Experimental Investigation of the Downstream Effects from High-Speed Fluid Structure Interactions and the Development of Supporting Diagnostics

A Dissertation Presented for the

Doctor of Philosophy

Degree

The University of Tennessee, Knoxville

James R. Chism

December 2023

DISTRIBUTION STATEMENT C. Distribution authorized to U.S. Government agencies and contractors. Other requests refer to AFRL/RQHA, 676 Second St, Arnold AFB, TN.

© by James R. Chism, 2023

All Rights Reserved.

This dissertation is dedicated to the countless, unnamed people who inspired me with a tireless work ethic, pushed me with an unwavering determination, and faced every day with an unshakable faith in themselves.

Acknowledgments

For a document of this size, the amount of time, effort, and sacrifice to achieve the work herein has been immense and was only possible due to the contributions of many individuals. I would first like to thank my advisor, Dr. Phil Kreth for the opportunity to be his graduate student and for the assistance along this journey. I would also like to extend my thanks to the other members of my doctoral committee: Dr. John Schmisseur, Dr. Trevor Moeller, and Dr. James Simonton. I do not take for granted the amount of time you have devoted to reading a document of this length and I appreciate the honest feedback and adherence to a high standard you placed upon the final stages of work towards my completion of this effort.

A special thanks goes to Dr. Mark Gragston for the guidance and opportunities he provided for me to work with many skilled researchers at various Air Force facilities. I would also like to thank those various researchers: Dr. Scott Peltier from AFRL at Arnold AFB and Dr. Zach Riley and Dr. Mike Spottswood from AFRL at Wright-Patterson AFB, for allowing me to work with them at their facilities and cultivate a unique graduate school experience. These experiences afforded me the opportunity to intern at Lockheed Martin with Anthony Brinkley, which has helped solidify the course I would like to take after graduation.

At UTSI, there are countless people to thank for the years of support along the way. The students of the HORIZON research group have been a bedrock of support throughout my time here, especially Dr. Lara Lash, Dr. Matthew Schwartz, Dr. Theron Price, and Lauren Lester. These former and current students started my path through graduate school and have been unwavering in their support even after moving on. The work of the support staff must also be recognized. Kirk Davenport, John Strike, and Larry Armstrong in their operation of the various facilities, Jack LeGeune and Gary Payne for their machining efforts

and willingness to push me to the front of the machining queue, and Kaycee Edwards for keeping the entire ship together and floating along the way.

On a personal level, there are too many people to name for the years of support, but one stands above the rest, my wife, Dr. Nancy Chism. Her patience and willingness to delay life without complaint made this entire process possible.

Abstract

This work investigates how surface deformations impact the downstream flow field and the development of diagnostic techniques to improve future experimental efforts. Three configurations using the UTSI Mach 2, Mach 4, and Mach 7 facilities are investigated with the primary diagnostics being schlieren, diagnostic paint, and focused laser differential interferometry (FLDI) along with other supporting diagnostics. The goals of these experiments were to identify the primary mechanism of these effects and to quantify the potential impact these effects would have on a canonical control surface. Experiments in the UTSI Mach 4 showed that unless separation occurred, the downstream turbulent boundary layer was unaffected by the presence of a surface deformation. Instead, weak shockwaves emanating from the deformation were identified as the most significant downstream effects. The designation of these shockwaves as weak came from the lack of changes in flow conditions after these waves, indicating that their impacts were localized to the waves themselves. These localized effects were highlighted in experiments conducted in the UTSI Mach 7 facility where the deformation shockwaves were impinged onto a downstream flare, resulting in increased surface heating at the impingement locations. Due to the complexity of the models and flow fields, large scale, a series of improvements to laser-based diagnostics have been made to increase the capabilities of future researchers in this area of study. These improvements center around the deployment of non-intrusive velocimetry to a test and evaluation (T&E) facility, and the improvement of FLDI by changing the lens configuration from spherical to cylindrical and quantifying the efficacy of using a high-speed camera as a detector. Using the UTSI Mach 2 and Mach 2.3 wind tunnels, the efficacy of using a high-speed camera as a detector was characterized, highlighting the trade-offs between lower sample rates and increased sensor size. When combined with cylindrical lenses, the high-speed camera added

a unique capability to the current state-of-the-art in FLDI measurements by achieving a highly resolved measurement over a thin-turbulent boundary layer.

Table of Contents

1 Introduction and Literature Review **1**

1.1 Fluid Structure Interactions 2

1.2 Shock-Shock Interactions 9

1.3 Improved Diagnostics 11

2 Experimental Capabilities **14**

2.1 Wind Tunnels 14

2.1.1 UTSI Mach 2.0 14

2.1.2 UTSI Mach 2.3 16

2.1.3 UTSI Mach 4.0 16

2.1.4 UTSI Mach 7.0 16

2.1.5 AFRL Mach 6.0 High Reynolds Number Facility 19

2.1.6 VKF Tunnel C 19

2.2 Diagnostics 22

2.2.1 Schlieren 22

2.2.2 Laser Induced Schliere Anemometry 23

2.2.3 Diagnostic Paint 24

2.2.4 Focused Laser Differential Interferometry 27

3 Fluid Structure Interaction Research **33**

3.1 Initial Experiments 33

3.2 Static Deformations on a Hollow Cylinder 39

3.2.1 Models 39

3.2.2 Results and Discussion . . . 42
3.2.3 Conclusions . . . 51
3.3 Downstream Impacts on a Control Surface . . . 54
3.3.1 Experiment Setup . . . 54
3.3.2 Results and Discussion . . . 60
3.3.3 Summary and Conclusions . . . 74

4 Diagnostic Development **81**
4.1 AFRL Mach 6 HRF LISA . . . 82
4.1.1 Experimental Setup . . . 82
4.1.2 Results and Discussion . . . 83
4.1.3 Velocity Measurements . . . 86
4.1.4 Uncertainty Methods . . . 88
4.1.5 Summary and Conclusions . . . 89
4.2 AFRL Mach 6 HRF Cylindrical Lens FLDI . . . 96
4.2.1 Experiment Setup . . . 96
4.2.2 Model . . . 96
4.2.3 Results and Discussion . . . 97
4.3 AFRL Camera FLDI . . . 105
4.3.1 Experimental Setup . . . 105
4.3.2 Results and Discussion . . . 108
4.4 Camera Based Cylindrical Lens FLDI . . . 119
4.4.1 Experiment Setup . . . 119
4.4.2 Results and Discussion . . . 132

5 Future Research **146**

Bibliography **147**

Vita **159**

List of Tables

2.1 The UTSI Mach 2.0 nominal operating conditions during measurements. . . 15
2.2 The UTSI Mach 2.3 nominal operating conditions during measurements. . . 17
2.3 The UTSI Mach 4 nominal operating conditions during measurements. . . . 18
2.4 The UTSI Mach 7 nominal operating conditions during measurements. . . . 20
2.5 The AFRL M6 HRF nominal operating conditions during measurements. . . 21
2.6 DLR temperature sensitive paint formulation used at UTSI 31

3.1 Zero crossing frequency of the shock foot calculated from the pressure time history of the shock foot transducer. Frequencies are in Hz, the upper threshold is $1.5\sigma + P_{mean}$, and the lower threshold is P_{mean} 36
3.2 Convective velocity measurements downstream of each deformation condition 49
3.3 A summary of the test conditions for these experiments. The list includes the deformation spacing from the flare-cylinder junction (D_{Sep}), measured second wave stagnation pressure (P_0) and stagnation temperature (T_0) along with the unit Reynolds number (Re_x) calculated from isentropic theory 57

4.1 A summary of test conditions in the Mach 6 High Reynolds Facility. The list includes the freestream Mach number (M_∞), the total pressure (p_0), the total temperature (T_0), the freestream static pressure (p), the freestream static temperature (T), the freestream velocity (U_∞), and the freestream per length Reynolds number (Re/x). 84
4.2 Velocities determined from linear fits of data in Fig. 4.7(a). 94
4.3 Velocities determined from linear fits of data in Fig. 4.7(b). 94

4.4 A summary of the tunnel operating conditions used in this work. 100
4.5 A summary of initial velocity calculation with the two LA-FLDI configurations. 104
4.6 Convective velocity comparison between the camera and diode. 109
4.7 A summary of the conditions used at during these tests. The list includes the measured stagnation pressure (P_0) and stagnation temperature (T_0) along with the isentropically calculated static pressure (P_∞), static density (ρ_∞), and unit Reynolds number (Re_x) 123
4.8 Measurements of the beam profiles for both configurations 128

List of Figures

1.1 Model and corresponding pressure coefficients for $M = 3, P_0 = 2000psf$. . . . 5
1.2 Six types of shockwave interference patterns 10

2.1 A CAD rendering of the UTSI Mach 2.0 15
2.2 A CAD rendering of the UTSI Mach 2.3 17
2.3 UTSI Mach 4 wind tunnel. 18
2.4 A CAD rendering of the UTSI Mach 7 wind tunnel 20
2.5 The Mach 6 High-Reynolds Facility at Wright-Patterson Air Force Base. . . 21
2.6 A general schematic of the Z-type schlieren setup commonly used for this research. 26
2.7 Schematic of a general LISA setup in a wind tunnel test section. 26
2.8 Diagram of PSP's operation 30
2.9 Sample calibration curve from the current research effort 30
2.10 Schematic of a traditional FLDI setup. 31
2.11 Spherical lens FLDI signal at the focal point. 31
2.12 Cylindrical lens FLDI signal at the focal point. 32

3.1 A schematic of the Mach 2 FSI experimental setup 35
3.2 UTSI Mach 2 pressure transducers. 35
3.3 Spectral content of the shock foot kulite for the various deformed configurations 36
3.4 Zero crossing frequency. 36
3.5 Shock tracking overlay on an instantaneous schlieren frame 38
3.6 Histogram of the mean shock foot location for each deformation case. 38

3.7 Images of the models used in this investigation 41
3.8 Schematic of the model shape with relevant dimensions labeled. 41
3.9 Mode 1+ deformation 44
3.10 Mode 1- deformation 44
3.11 Mode 2+ deformation 45
3.12 Mode 2- deformation 45
3.13 Spectra from the LA-FLDI system 47
3.14 Spectra from the LA-FLDI system 47
3.15 Downstream spectra for the various mode deformations compared to the baseline mode 0 undeformed model 48
3.16 Normalized convective velocity measurements compared to the theoretical velocity profiles for undisturbed and previously separated turbulent boundary layers 49
3.17 Coefficient of pressure for the Mode 2+ case. 52
3.18 Coefficient of pressure for the Mode 2- case. 53
3.19 Model used for the duration of the experimental campaign. Note: the deformation was moved between runs. 56
3.20 Schematic of the planned experiment. 57
3.21 Top view schematic of the schlieren system used. 58
3.22 Side view schematic of the TSP system used. 59
3.23 Time averaged schlieren image of the undeformed hollow cylinder flare. . . . 61
3.24 Surface map of the modified Stanton number 61
3.25 Cartesian to cylindrical coordinate transformation. 64
3.26 Linear C_h profiles along the baseline flare configuration 65
3.27 C_h profile along the centerline of the flare 66
3.28 Time averaged schlieren image of the 00 mm deformation. 68
3.29 Surface map of the modified Stanton number for the 00 mm case. 68
3.30 C_h profile along the centerline of the 00 mm deformation case 69
3.31 Time averaged schlieren image of the 30 mm deformation. 71
3.32 Surface map of the modified Stanton number for the 30 mm case. 71

3.33 C_h profile along the centerline of the 30 mm deformation case 72
3.34 Time averaged schlieren image of the 50 mm deformation. 76
3.35 Surface map of the modified Stanton number for the 50 mm case. 76
3.36 C_h profile along the centerline of the 50 mm deformation case 77
3.37 Time averaged schlieren image of the 80 mm deformation. 78
3.38 Surface map of the modified Stanton number for the 80 mm case. 78
3.39 C_h profile along the centerline of the 80 mm deformation case 79
3.40 Direct comparisons of the C_h profiles for each deformation case 80

4.1 A depiction of the experiment setup for LISA in the Mach 6 High Reynolds Facility at Wright-Patterson Air Force Base. The laser operating wavelength was 1064 nm and the schlieren LED source was nominally around 530 nm. A panel placed on the outside of the tunnel was used to terminate the 1064 nm beam after passing through the tunnel. 84
4.2 An illustration showing how plasma movement is masked in the path-integration of the schlieren. Sensitivity to the motion is lost in the schlieren path-integration for this setup with parallel schlieren light and laser optical axes upon entry into the tunnel. 85
4.3 (a) Gaussian beam calculation of the laser propagation through the $f = -100$ mm and $f = 150$ mm lenses system. The laser beam was focused to the nozzle centerline. (b) An intensity distribution along the beam path calculated from the Gaussian beam calculations. 85
4.4 A schlieren image showing the effect of multiple laser-induced plasma occurring around the focus. The effect is most noticeable as a series of concentric rings in the schliere. Flow is from left to right. 90
4.5 20 kHz schlieren image sequences showing the several schliere written by the 10 kHz burst laser convecting in the Mach 6 flow. The arrows indicate the movement of a schliere and are color-coded uniquely. 91
4.6 A graphical outline of the methodology used to track the schliere. 92

4.7 Displacement versus time data for (a) Condition 1 and (b) Condition 2. Five schliere were tracked for each and given the limited field-of-view and camera frame rate, only three frames each were appropriate for the analysis. 93
4.8 The standard deviation of the LISA high-speed schlieren images allow for measurement of the Mach number via the Mach cone effect. Measurements at (a) Condition 1 provide an angle of $9.9^\circ \pm 0.29^\circ$ and for (b) Condition 2 yield an angle of $10.0^\circ \pm 0.28^\circ$. These correspond to a Mach number of 5.82 ± 0.17 and 5.76 ± 0.16 respectively. 95
4.9 The flat plate model used in this work. 100
4.10 A calculated ray trace showing the LA-FLDI setup with six focused beam pairs. Note that the polarizers are not shown since they don't affect beam geometry. 101
4.11 Images of the LA-FLDI beams at the focus. 101
4.12 Spectra for the intermediate and highest Reynolds number conditions. 102
4.13 Comparison of freestream spectra between the spherical and cylindrical configurations for each Reynolds number. 103
4.14 Images of the LA-FLDI beams at the focus. 103
4.15 Initial analysis the correlation coefficients for determining the velocity from two channels of the LA-FLDI. 104
4.16 Schematic and setup of the FLDI system used in these experiments. The red text highlights the beam expansion optics only used in the cylindrical lens configuration. 107
4.17 Images of the LA-FLDI beam profiles at the focus. Only two are shown since the majority of measurements only utilize two points. 107
4.18 A comparison of signal size on the camera sensor and the effect of selecting only a region of interest versus the whole laser. 109
4.19 Comparison of power spectra from using the camera as the collection system to data collected with a photodetector. 109

4.20 Freestream and boundary layer power spectra for the photodetector and camera. (a) was measured at 15 mm or 1.36δ from the floor and (b) was measured at 5 mm or 0.45δ from the floor 114
4.21 Freestream and boundary layer power spectra for each signal on the camera. (a) was measured at 1 mm or 0.27δ from the floor and (b) was measured at 5 mm or 0.45δ from the floor 114
4.22 (a) Photodiode velocity profile normalized by the boundary layer thickness and freestream velocity. (b) Inner variable scale velocity profiles of photodiode measured velocities 115
4.23 Camera velocity profile normalized by the boundary layer thickness and freestream velocity. 115
4.24 Power spectra across the upper edge of the floor boundary layer. Each spectra represents a distinct point along the signal. 116
4.25 (a) Power spectra across the plate boundary layer. Each spectra represents a distinct point along the signal. (b) Power spectra across the upper half of the plate boundary layer signal 116
4.26 Correlation plot for convective velocity calculation. 117
4.27 Comparison of the minimum resolvable velocity changes for a given velocity between the photodiode and camera. Note the diode sampling rate is 5 MHz while the camera is 1.008 MHz. 118
4.28 Tube jet used for cylindrical lens FLDI characterization with the camera. . . 120
4.29 Average schlieren image of the flat plate model with FLDI measurement locations highlighted. 123
4.30 Schematic of the bench top schlieren setup used to image the tube jet. 124
4.31 Schematic of the modified Z-type schlieren setup used in the Mach 2 facility 124
4.32 Schematic of the cylindrical lens FLDI system used to measure the flat plate boundary layer. The green labels are for the elements present in both lens configurations for the camera, while the blue labels highlight optic(s) that are either unique to the cylindrical lens system used in these experiments and the red label highlights the optic(s) used only in the spherical lens configuration. 125

4.33 Beam profiles at the system focus for both lens configurations with relevant lengths labeled. 127
4.34 Beam profiles with accurate measurements using the $1/e^2$ beam diameter for Gaussian beams. 130
4.35 (a) cylindrical FLDI signal imaged by the camera. The $1/e^2$ extent of the beam was calculated in MATLAB and is highlighted in red. (b) mean intensity of the camera signal as the second Wollaston prism is translated across the beam path. 131
4.36 0.0 x/d 133
4.37 0.3 x/d 134
4.38 0.6 x/d 135
4.39 1.0 x/d 136
4.40 Average intensity of each row of pixels 140
4.41 Normalized FLDI signal at x = 60 mm. 141
4.42 Normalized FLDI signal at x = 90 mm. 142
4.43 Normalized fluctuation profiles at both x locations for Condition 1 143
4.44 Normalized fluctuation profiles at both x locations for Condition 2 144
4.45 Normalized fluctuation profiles at both x locations for Condition 3 145

Chapter 1

Introduction and Literature Review

Due to increased international competition and a renewed interest in space travel, hypersonic flight is now a paramount interest to the aerospace research community. Currently, hypersonic capabilities are limited to single use vehicles such as orbital rockets or missiles, but the interest is ultimately in multi-use, reusable vehicles, similar to that of the space shuttle orbiter. While the space shuttle was used in a repeatable manner, the cost of production and maintenance became prohibitively expensive. One of the major drivers of this maintenance expense was ensuring the outer thermal protection system was in working order. After every flight, a large team of engineers was required to inspect every tile on the orbiter for damage.

This surface damage was a result of the extreme thermal loads generated during hypersonic flight through the atmosphere. Thermocouple measurements taken during the orbiter flight show surface temperatures reaching 4000 K [1]. Even at half of that temperature, the loading on a vehicle can cause failure, especially when exposed across multiple flights. Additionally, companies and governments will require much shorter turn around times than those of the shuttle orbiter, increasing the likelihood of surface defects being missed. With modern high-speed vehicles, the use of new thermal protection materials and desire to create reusable systems increases the uncertainty in the surface conditions as material degradation from the extreme flight environment changes the surface topology. This uncertainty in surface conditions has prompted a resurgence in research on the interaction of the high-speed fluid and the vehicle structure. This resurgence is driven by off-design surface

features introducing changes to the downstream flow field that can increase heating or change aerodynamic forces on control surfaces that aren't designed for in the flight planning.

Compared to fundamental aerodynamic experiments, fluid structure interaction (FSI) research uses larger, more complex geometries, resulting in multi-component models at scales closer to flight vehicles. This increase in geometric scale requires the use of large-scale facilities that, in most cases, are utilized for test and evaluation (T&E) purposes. These facilities run at high Mach numbers with either low densities, high enthalpies, and/or short durations, limiting the number of available diagnostics. To alleviate this, universities have invested in creating facilities that bridge the scales between the traditional small scale academic wind tunnels and the production scale facilities found at places like Arnold AFB and Wright Patterson Air Force Base (AFB). These facilities have allowed not only for FSI research at the same scales as government and industrial efforts but have also opened the door for scaling of diagnostics from the academic sector to the larger facilities.

1.1 Fluid Structure Interactions

These first efforts in understanding fluid structure interactions (FSIs) were the result of small-perturbation theory, a subbranch of linear supersonic theory. For a full breakdown of small perturbation theory, the author encourages the reader to look at reference [2]. This article gives a detailed breakdown of linear theory as well as small perturbation theory. To highlight the relevant theory, chapter 8, section 5 from the book Elements of Gasdynamics [3] is described here starting with Eq. 1.1. This is the velocity potential equation for the small perturbation equation that is described at the beginning of chapter 8.

$$(1 - M_\infty^2)\frac{\partial \phi}{\partial x^2} + \frac{\partial \phi}{\partial y^2} = 0 \tag{1.1}$$

For flow past a wavy wall, the boundary conditions are described by Eq. 1.2, where a is the amplitude of the waves, and $l = 2\pi/\alpha$ is the wavelength. Since $M_\infty^2 - 1$ is greater than zero for supersonic flow, Eq. 1.1 becomes a hyperbolic equation in Eq. 1.3, where $\lambda^2 \equiv M_\infty^2 - 1$. The solution of this equation is discussed in reference [3] and is a straightforward solution, taking only half a page in the book.

$$y - a \sin \alpha x = 0 \tag{1.2}$$

$$\frac{\partial \phi}{\partial x^2} - \frac{1}{\lambda^2} \frac{\partial \phi}{\partial y^2} = 0 \tag{1.3}$$

The primary results of this solution are presented in Eqs. 1.4 through 1.6, where u is the streamwise velocity along the surface, v is the wall normal velocity along the surface, and C_p is the coefficient of pressure along the curved surface. Since the flow turns relative to a flat surface when moving along a curve, there is a vertical component that is typically not accounted for. Based on experimental observations from the author and past researchers, this vertical velocity component does not eject mass away from the boundary layer into the freestream and can be treated as a purely inviscid phenomenon. For C_p, this formulation shows that the pressure along the curve in supersonic flow is phase shifted along the curved surface when compared to the subsonic case. In the subsonic case, the maximum and minimum pressures occur at the peak and trough of the sinusoidal deformation respectively, but in the supersonic case, they both occur halfway along the curve, where the angle of deformation is greatest.

$$u = -\frac{U_\infty a \alpha}{\sqrt{M_\infty^2 - 1}} \cos \alpha [x - y\sqrt{M_\infty^2 - 1}] \tag{1.4}$$

$$v = 2a\alpha \cos \alpha [x - y\sqrt{M_\infty^2 - 1}] \tag{1.5}$$

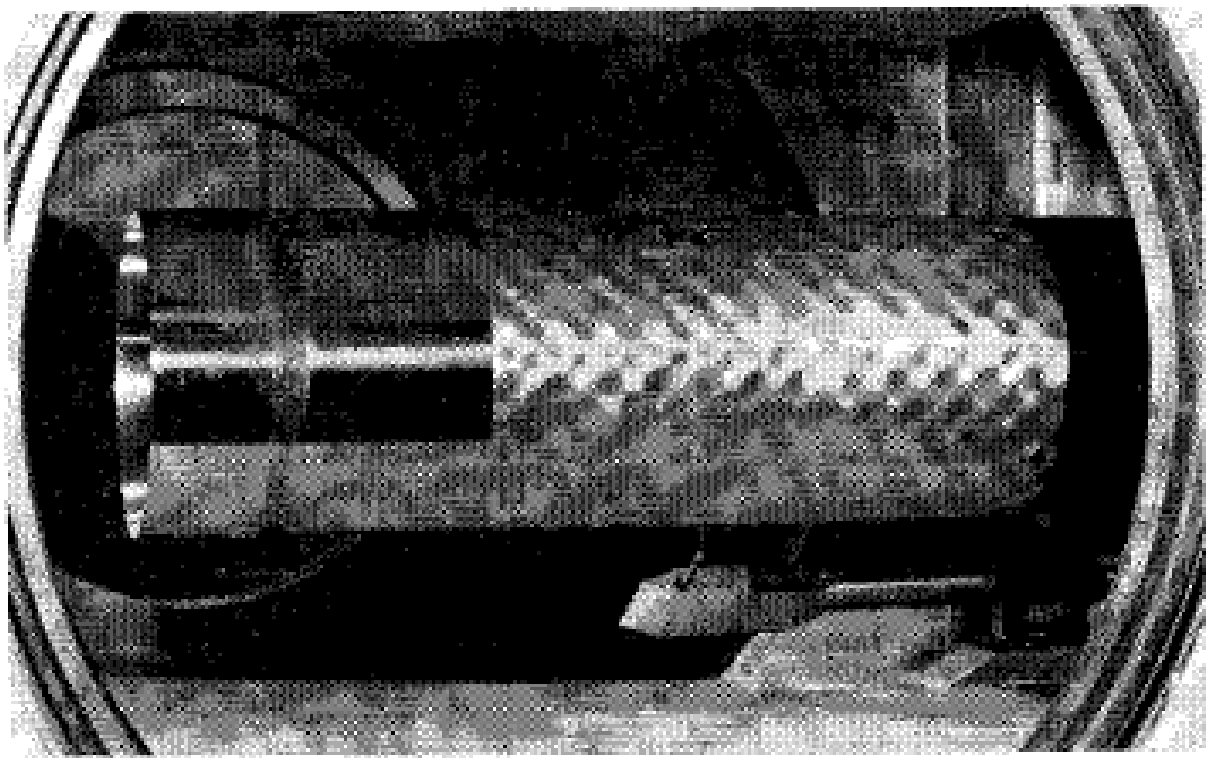
$$C_p = \frac{2a\alpha}{\sqrt{M_\infty^2 - 1}} \cos \alpha [x - y\sqrt{M_\infty^2 - 1}] \tag{1.6}$$

Early research into the effects of fluid structure interactions focused on the local changes to flow characteristics and surface forces, particularly at low Mach numbers [4]. Rogers [5] developed a boundary layer theory to predict the pressure and drag due to transverse waves generated by deformed surfaces. His method relied on a proper understanding of boundary layer shape factor and thickness and his results were more accurate than the existing inviscid theories at the time. Compared to experiments in the National Aeronautics

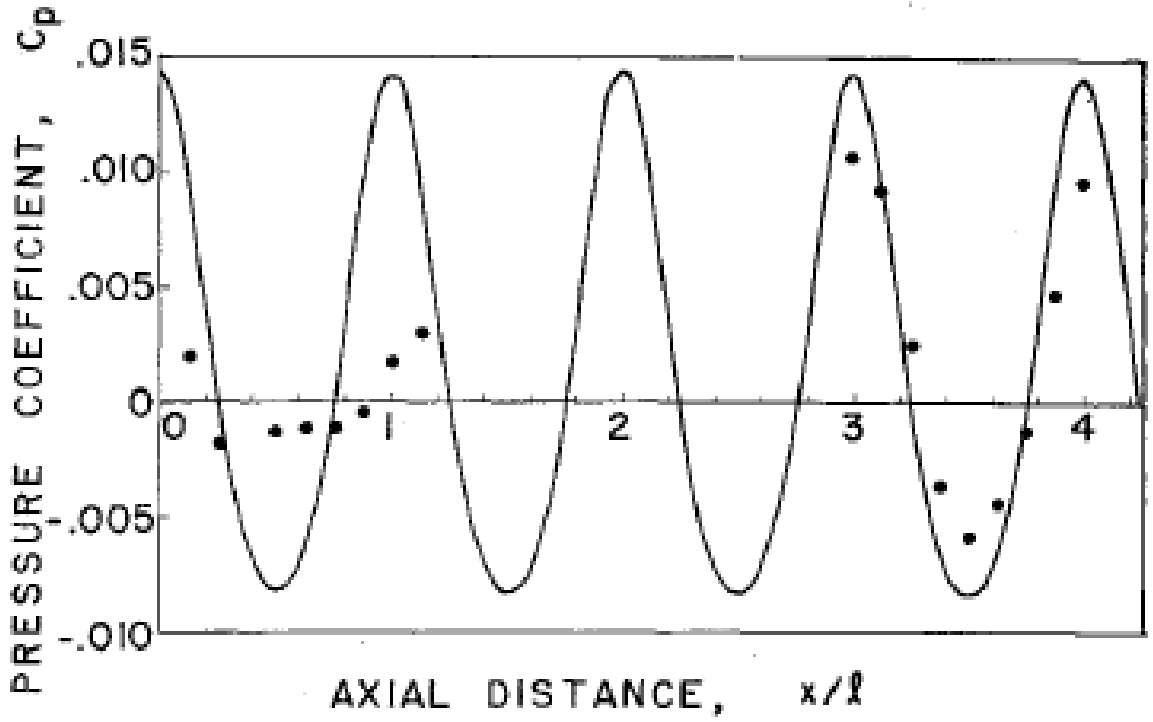
and Space Administration (NASA) Langley Mach 2 wind tunnel, his theory had excellent agreement with pressure and drag measurements. He noted that the strong deviation from inviscid methods came from the formation of Görtler vortices formed in the subsonic region of the boundary layer [5]. Anderson [6] used pressure transducers, oil flow surface visualization, and schlieren imaging to investigate the wavy surface of a hollow cylinder at Mach 3.0 and 4.62. The waves on the cylindrical body varied in both the streamwise and radial directions of the cylinder, with wave amplitudes on the order of the boundary layer thickness seen in schlieren. Pressure measurements indicate a strong correlation with linear supersonic theory, with no discernible effect from the number of preceding waves. Oil flow visualization showed the presence of separation regions between the peaks of successive waves.

Shore and Dixon looked at turbulent pressure and heat transfer coefficients. Using a variety of instrumented, buckled aluminum panels in the NASA Langley Mach 3 tunnel, the researchers compared Stanton numbers across the various deformations. They concluded that Stanton number was related to changes in slope; however, the changes were not linearly proportional. They note that the smallest deformation investigated increased the Stanton number by 150 percent of the flat plate boundary layer thickness [7]. Later, higher Mach number cases were studied such as those by Bertram, looking at the impact protruding waves have on the heat transfer on a cone at Mach numbers of 6, 8, and 20 for both laminar and turbulent boundary layers. The deformations augmented the heat transfer locally, with lower values in the troughs and peak values near the peak of each wave. They concluded that the deformations generated strong local heating effects and increased downstream heating relative to the unperturbed cases. These downstream effects however were still consistent with theory, only showing changes as step increases due to the increased upstream temperature. For all cases, the heat transfer effects can be treated as a sum of singular waves in the streamwise direction. This result highlighted that there appeared to be no coupling in the effects generated by successive waves, that each could be taken as an independent effect. In the case of drag/pressure, repeated transverse waves generated Görtler vortices that significantly modified the drag profile. This was evident in the boundary layer velocity profiles which showed significant waviness.

DISTRIBUTION STATEMENT C. Distribution authorized to U.S. Government agencies and contractors. Other requests refer to AFRL/RQHA, 676 Second St, Arnold AFB, TN.



(a) Wavy Cylinder Model



(b) Static pressures on the wavy cylinder

Figure 1.1: Model and corresponding pressure coefficients for $M = 3, P_0 = 2000psf$. This was taken from [6]

To build on these early studies, many current research efforts are interested in the response of compliant surfaces to aerodynamic loading with the of understand the effect that surface compliance would have on the forces driving the generated deformations. Lynch *et al.* [8] used a combination of pressure sensitive paint (PSP) and digital image correlation (DIC) to characterize a flexible beam in a shock tube. Their results show a weak correlation between the natural frequency of the beam and the vortex shedding frequency from the tip of the beam [8, 9]. This result indicates the feedback nature of these types of interactions; however, the short test duration points to the tunnel startup as the driving mechanism rather than the steady state forces. Casper [10] looked at the response of compliant panel underneath a laminar boundary layer with a forced input in the Purdue Mach 6 quiet tunnel. The forcing input was a laser spark generated in the upstream boundary layer convecting over the compliant panel. These laser sparks generated a panel response in all three directions. When these turbulent packets were generated at the natural frequency of the panel, the panel deformation amplitude reached up to two hundred times the amplitude of the isolated sparks. Additionally, the panel responded at 10 to 20 times the amplitude when excited over a band of frequencies that included the panel's natural frequency [10]. Tan and Gramola [11] studied a deformed surface as a method for shock control. Using the Imerpial College Mach 2 wind tunnel, a shock was generated to impinge onto a flexible surface, whose shape was controlled by a pressurized cavity below the panel. As the shock was traversed over the curvature, the separation region varied based on its location along the surface [12]. This phenomenon was explored further, with the results showing that impingement on a positive slope yielded a reduction in wave drag while the negative slope impingement resulted in increased wave drag. This was caused by flow re-acceleration, generating a stronger rear shock. The authors also noted that the flexible panel served to diminish the unsteadiness in the shock, acting as a damper to the oscillating system [11].

In an effort to mimic more flight-like conditions, current research efforts have looked into methods for oscillating the thin panels and due to the limited forces generated in wind tunnels, impinging shocks have been the primary method of panel loading. Neet *et al.* [13]. used a shock generator above a compliant flat plate to assess the response due to shock excitation. Without an input frequency, the shock impingement generated

a stable deformation that showed a decrease in shock unsteadiness while augmenting the separation region [13]. This decrease in unsteadiness is most likely due to the trapping of the shock foot in the recessed portion of the deformed surface. The CalTech team notes the drawback of panel response time in impulse facilities, where the time between tunnel startup and the end of steady state leaves little to no time for the structure to damp out the startup loads. To account for this, Spottswood [14] and Beberniss [15] used a similar shock generator on the floor of the RC-19 facility in Wright-Patterson, Ohio. Initial experiments saw coupling between structural dynamics and shock motion. Using two impingement locations, the dynamics of the panel were studied using PSP and DIC. The authors noted that changes in the impingement location excited different, non-harmonic frequencies [16]. Using a combination of PSP and DIC, they show a low frequency excitation of the panel that matched the expected natural frequency of the panel [14, 15]. An important note in their results is the presence of a broadband, low frequency response in the pressure measurements when no panel is present. This low frequency signal encapsulates the natural frequency of the panel used. This result is congruent with the work of Casper [10] whose broadband excitation generated a response of the compliant panel at its natural frequency. This loading was sufficient to drive the panel to failure after 30 minutes of test time through crack propagation from the trailing edge [17]. Peltier *et al* [18]. attempted to recreate this experiment in the VKF Tunnel D. Using the same diagnostic configuration, they were unable to identify any frequency content as a result of panel deformation, suggesting that the driving mechanism was due to acoustic noise in the RC-19 facility [18].

These prior experiments have been expanded upon with computational studies as well, focusing on the prediction of structural changes to given aerodynamic input. Visbal [19] simulated a compliant panel under a laminar boundary layer and under laminar shock boundary layer interaction. For the undisturbed laminar boundary layer, high frequency panel oscillations began with their frequency corresponding to boundary layer instabilities. The shock interaction resulted in a reduction of unsteadiness similar to that of Gramola [11]. This stabilizing of the shock suggests a possible use as a passive flow control method for shock trains in compressor inlets as noted by the author [19]. Boyer [20] compared the effect of an inviscid free shock impingement to a viscous laminar shock impingement. These

simulations showed a significant difference in pressure values over the deformation, based on the configuration used. For the viscous case in particular, the oscillation amplitudes were increased compared to the inviscid case. The viscous impingement also introduced non-harmonic oscillations likely due to boundary layer instabilities amplifying the force generated by the impinging shock [20]. Brouwer [21] compared the effects of static and dynamic deformations in a two-dimensional deformation case. The results showed that shock induced separation size was highly dependent on surface deformation size and that the initial separation size was a major determiner in the amplitude of deformation. The varying separation size also changed the steady aerodynamic forces, not only with reductions in velocity but with a phase shift along the deformed surface. Additionally, increases in frequency corresponded to lower deformation amplitudes regardless of shock strength, indicating a dominance of the panel in the resultant effects [21]. Expanding away from laminar boundary layers, Shinde [22] studied the effect of a transitional shock boundary layer interaction over a compliant panel. Introduction of the panel yielded significant modification of the principal Reynolds stresses along with an introduction of Görtler instabilities [22].

To begin understanding the impacts of external fluid structure interactions, research efforts have started to look at surface deformations analogous to ones found along a vehicle's surface. Peltier [18] investigated various three-dimensional curvatures on the floor of von-Karman Gasdynamics Facility (VKF) Tunnel D. Using particle image velocimetry (PIV) and PSP, the researchers compared the effect of curvature as well as dimensionality. Each of the deformations had an amplitude greater than the thickness of the turbulent boundary layer they were subjected to. Their pressure results are similar to those of Anderson [23], following linear theory along the length of the curvature. The velocities from PIV show expected changes across the face of the deformation, with a separation bubble at the beginning of the most extreme curvature. The changes in both pressure and velocity appear to scale as a function of curvature, with no notable dependence on amplitude in accordance with linear theory [18]. Computationally, Shinde *et al.* [24] explored a wavy panel deformed in a turbulent boundary layer. Their work notes that higher deformation modes generate a greater effect on the low frequency pressure fluctuations due to an increase in separation. This separation generates low frequency unsteadiness associated with shock boundary layer

interactions and could produce a coupling effect downstream [24]. To expand on previous studies, this dissertation work looks at static deformations without the influence of impinging shocks. Unlike the majority of referenced studies, the research presented here will focus on the downstream effects generated by static FSI and how they will impact control surfaces, in line with prior work from Anderson [6] and Peltier [18].

1.2 Shock-Shock Interactions

From prior FSI research, a defining feature of surface deformation is the propagation of shock waves. Schlieren images from both Anderson [6] and Boyer [20] show shock waves emanating downstream from their deformations. At sufficiently high Mach numbers these shockwaves pose a risk to downstream control surfaces, generating a shock-shock interaction at the face of the control surface. The seminal work on shock-shock interactions comes from Edney [25, 26]. In this report, Edney defines six classifications of shock-shock interactions based on the angle of intersection, though no numerical angles are reported. Types I-IV are characteristic of leading-edge shocks encountering vehicle attachments such as the boosters on the space shuttle or the pylon of the X-15. Types V and VI are of greater interest to this study as they are more characteristic of interactions seen on control surfaces. From Edney's report, type V and VI interactions are a result of two shocks running in the same direction with type V having a more oblique angle between the two interacting shocks than that of a type VI. Type V interactions generate an increase in pressure and heat transfer downstream of the interaction due to a jet being produced at the point of shock intersection. Type VI interactions produce lower pressure and heat transfer as this interaction produces a shear layer instead of a jet [25, 26]. To illustrate each type of Edney interaction, Fig. 1.2 [27] shows a diagram of the different interactions as they relate to a leading edge bow shock.

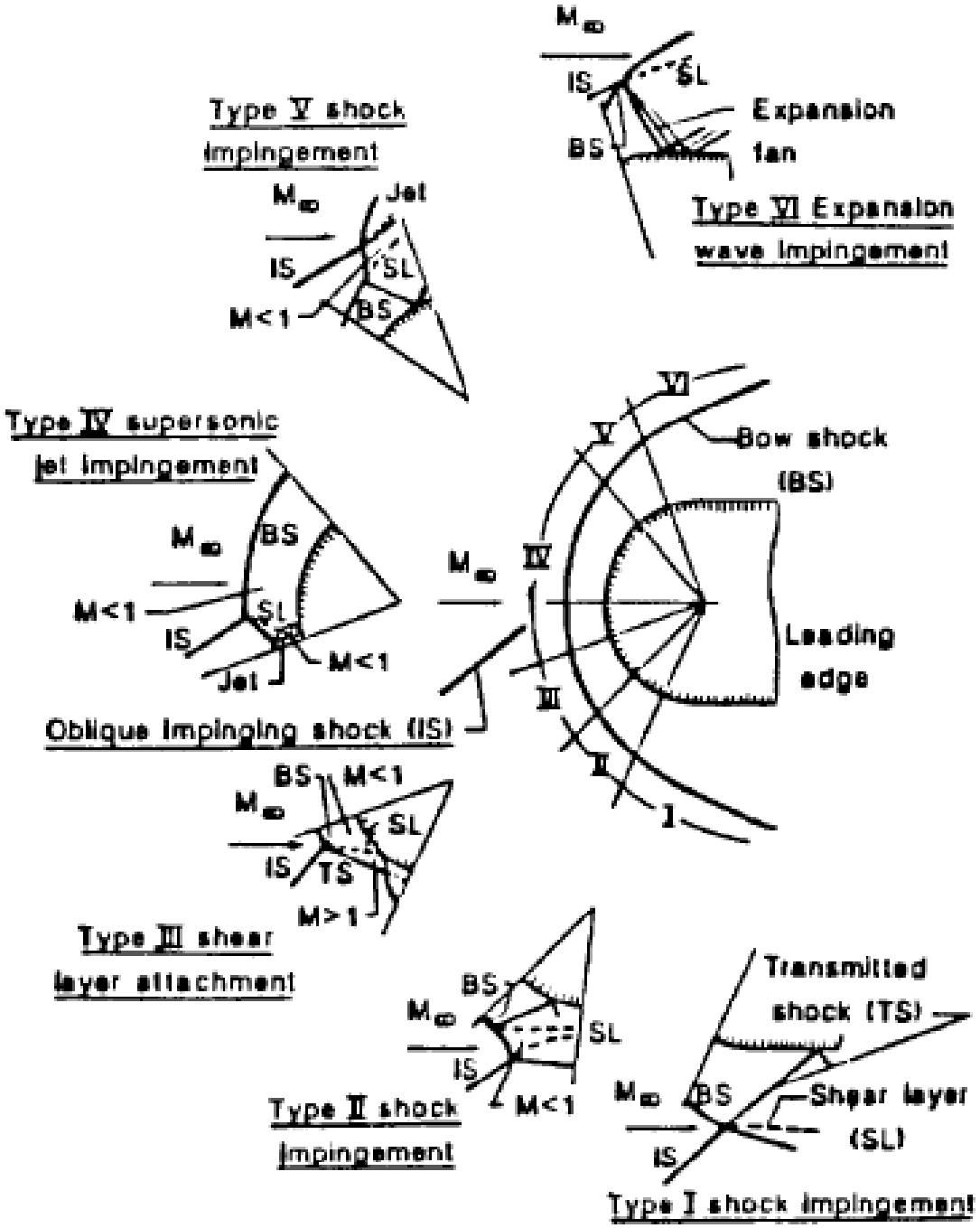


Figure 1.2: Six types of shockwave interference patterns [27].

Since Edney's report, many researchers have explored the impacts of various shock-shock interactions. The fundamentals of these concepts are reviewed in Bertin's Hypersonic Aerothermodynamics, Ch. 9 [1]. This chapter outlines the effects of various shock-shock interactions, and in particular the type V interaction on the wing of the space shuttle orbiter. The experiments showed an increase in pressure generated by the impinging shock and a significant increase in the heating rate [1, 28, 29]. Further work on this configuration varied both Mach number and Reynolds number. Keyes *et al.* [30] ran an extensive experimental study across Mach numbers ranging from 1.5 to 6, comparing the effects from type I to type IV interactions. They note that there is a temperature increase of 7.5 to 17 times the stagnation value across these interactions, indicating the extreme loading generated [30]. Berry [31] looked at the effect that fin sweep angle had on the strength of the interactions. He noted that there were two maximum heat transfer cases, one resulting in a type IV interaction with a sweep angle of 15° and the other a type III interaction with a sweep angle of 25° [31]. These results were reinforced by computations from Klopfer [32] and Comeaux [33] who were able to develop numerical techniques to match the trends shown in experiments [32, 33]. Hackett continued similar work, in a Mach 7 high enthalpy facility to assess the impact of gas chemistry in a type IV interaction. He noted that the increased heating was less impacted by chemistry than the inviscid interaction between the shocks [34].

A common feature of the shock-shock interaction research presented is the lack of boundary layer separation in the control shock. Eliminating this feature allows researchers to focus on the inviscid portion of the interaction [28]. It also comes from the assumption that the propagating shock is generated at the front of a vehicle and any interaction from it will be away from the separation region of the control surface. To expand on this, this dissertation seeks to investigate the impacts of a shock-shock interaction when related to the reattachment of a separated region on the interaction surface.

1.3 Improved Diagnostics

Due to the high operational cost, impulse facilities like those used in this research effort are the standard for high Mach number flows in academic research environments. While

these facilities allow for increased Mach numbers in the test section, run times are severely diminished. This limits the diagnostics available to interrogate these flow fields. Velocimetry techniques, such as particle image velocimetry (PIV), are impractical in such facilities. This presents a problem for researchers interested in off-body measurements. To make up for this, many laser based techniques have been developed [35, 36, 37]. Two techniques in particular show immense potential in increasing the current diagnostic potential in the UTSI impulse facilities: Laser Induced Schliere Anemometry (LISA) and Focused Laser Differential Interferometry (FLDI).

LISA is a new technique developed in the HORIZON research group. The majority of work has been done by Lester and Gragston [36], with the author supplementing their efforts. A more detailed breakdown of this technique will be explored later, but as noted by Lester [36], LISA is primarily used for freestream velocity measurements, with additional calculations of Mach number and static temperature. This technique was successfully deployed in the UTSI Mach 2 and Mach 4 wind tunnels, with uncertainties reported less than 3 percent of the theoretical values [36]. Even with the successful demonstration in these facilities, the diagnostic still requires deployment in outside facilities to prove its maturity. Along with this, Mach 4 and Mach 2 are below the desired hypersonic regime. Successful deployment outside of UTSI allows for both goals to be accomplished while simultaneously increasing the capability of government facilities.

Unlike LISA, FLDI is a mature diagnostic originally discussed by Smeets [35] and Smeets and George [38], and is utilized by many academic research groups. Its popularity has increased recently due to the increased interest in high-speed flows. The primary use for FLDI is studying high-speed turbulent and transitional boundary layers. Its simplified setup allows for acquisition rates up to and beyond the GHz range, making this technique ideal for impulse facilities. FLDI measures density fluctuations and, combined with its high acquisition rate, allows for excellent frequency resolution. Historical boundary layer studies show a characteristic frequency distribution for turbulent boundary layers, with a notable $-5/3$ roll off in the high frequency range that correlates to the decay of the turbulent energy cascade [39]. This technique has been utilized in a number of high speed flow studies to investigate transitional and turbulent flows [40, 41, 42]. Fulghum [43] characterized the

freestream disturbances at AEDC Tunnel 9 using FLDI while Ceruzzi *et al.* [42] have also used FLDI for disturbance measurements at Mach 18 conditions in the same facility. Ceruzzi *et al.* [44] also used FLDI to study a turbulent floor boundary layer at Mach 3. Along with this, FLDI is able to resolve the second mode instability in hypersonic transition [45]. Parziale *et al.* [46] applied FLDI in the CalTech T5 shock tunnel to measure the second-mode instability in on a cone and along with characterizing the freestream flow conditions of the tunnel [46]. Gragston *et al.* [41] used linear array FLDI (LA-FLDI) to detect second mode transition on a flared cone in the University of Texas A&M's Mach 6 quiet tunnel across multiple Reynolds numbers, showing the results matched the expectations from linear stability theory.

Researchers have extended the utility of FLDI by introducing several configurations and extensions. For example, LA-FLDI has been developed to measure flow disturbance velocities by correlating the signals of two beam pairs. The correlation yields the temporal delay and when combined with the known separation distance of the beam pairs, it provides a mean disturbance velocity estimate. This technique has been employed in several prior experiments [47, 48]. Gragston, Siddiqui, and Schmisseur [41] and Gragston *et al.* [49] has utilized this technique multiple times to measure convective velocities in both turbulent and transitional boundary layers. Ceruzzi and Cadou [44] utilized this technique to show that the measured convective velocities measured scale the same as the gas flow velocities in the turbulent boundary layer. Another variation of FLDI developed by Houpt *et al.* [50] utilizes cylindrical lenses to keep the beams constant in wall normal height while still allowing for the focusing aspect that is key to limiting optical path integration effects. This cylindrical lens setup is particularly well-suited for measurements on flat plate geometries since it removes the potential beam clipping associated with using a spherical lens, which does not keep the beam at a constant wall normal height.

Chapter 2

Experimental Capabilities

This section outlines the facilities and diagnostics used in these research efforts. Each section will give a brief overview of the facilities and diagnostics used throughout the various experiments in this dissertation.

2.1 Wind Tunnels

Throughout the course of research, a large number of wind tunnel facilities have been utilized either for the study of FSI or for diagnostic development. This has allowed for a variety of Mach numbers, Reynolds numbers, and experimental scales. This section gives an overview of each facility used in the subsequent experiments.

2.1.1 UTSI Mach 2.0

The Mach 2.0 tunnel at UTSI was used extensively in this research effort. The facility operating conditions are shown in Table 2.1. The Mach 2 tunnel has a 20.32 cm by 20.32 cm test-section and per length Reynolds number range of 30-69 million per meter. This facility was used for the initial FSI experiments along with diagnostic development. This tunnel was used primarily for its small scale and ease of use. Given its blowdown capabilities and easy model adjustments, many runs could be performed daily with minute changes to the setup. Figure 2.1 shows a CAD drawing of the facility.

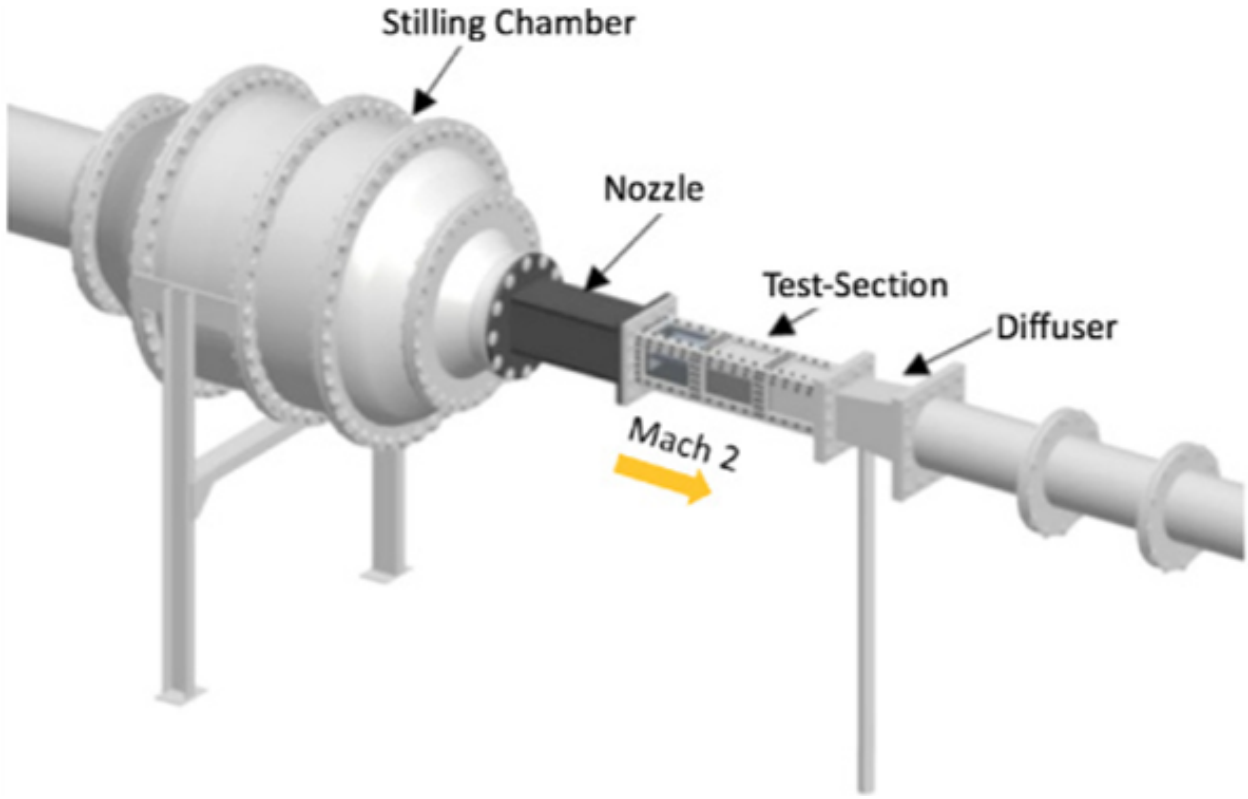


Figure 2.1: A CAD rendering of the UTSI Mach 2.0

Table 2.1: The UTSI Mach 2.0 nominal operating conditions during measurements.

Tunnel Conditions	**UTSI Mach 2.0 Tunnel**
P_0 [kPa]	241
T_0 [K]	285
U [m/s]	500
Re/x [$\times 10^6$ m^{-1}]	30.2

2.1.2 UTSI Mach 2.3

The Mach 2.3 tunnel at UTSI was utilized as a preliminary facility for some of the diagnostic development work. It has a 15.24 cm by 15.24 cm test-section with a facility per length Reynolds number range of 26-60 million per meter. A full list of the facility's nominal run conditions is given in Table 2.2 The Mach 2.3 facility was used as for the initial exploration of the camera as a detector due to the convenient setup available at the time and the experiments were moved to the Mach 2 for a more detailed investigation into the topic.

2.1.3 UTSI Mach 4.0

The UTSI Mach 4 wind tunnel is a Ludwieg tube with a 60.9 cm $\times$ 60.9 cm (24 in $\times$ 24 in) test section and an approximate steady state run time of 120 ms. The Reynolds number is variable, with the ability to go down to $3.48 \times 10^6 m^{-1}$ and up to $5.28 \times 10^6 m^{-1}$; however, for this effort the Reynolds number was held at its highest value. The primary use for this facility was in the study of downstream FSI effects but prior research efforts have used this facility for diagnostic development. A major advantage of using this facility is its large scale. Figure 2.3 and Table 2.3 show a schematic of the facility along with the run conditions used for these experiments. A detailed description and characterization is provided by Kreth *et al.* [51].

2.1.4 UTSI Mach 7.0

The UTSI Mach 7 wind tunnel is a Ludwieg tube with a 45.7 cm $\times$ 45.7 cm (18 in $\times$ 18 in) free jet test section and an approximate steady state run time of 100 ms. With the current facility infrastructure, the unit Reynolds number is set to $5.21 \times 10^6 m^{-1}$ for the nominally reported values. Characterization work is still ongoing with this facility. The free jet test section is temporary pending the fabrication of a permanent standard test section. Table 2.4 shows the nominal run conditions used, with a detailed description and characterization is provided by Gragston *et al.* [52].

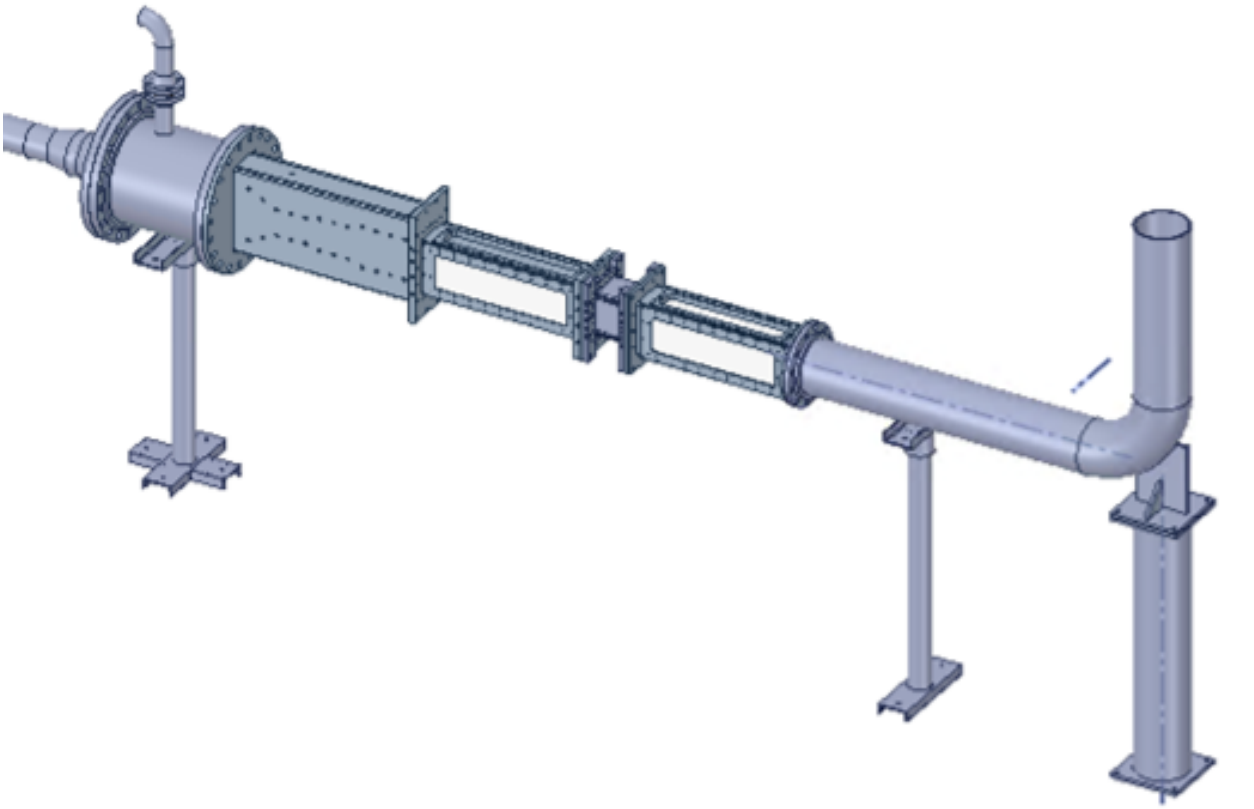


Figure 2.2: A CAD rendering of the UTSI Mach 2.3

Table 2.2: The UTSI Mach 2.3 nominal operating conditions during measurements.

Tunnel Conditions	**UTSI Mach 2.3 Tunnel**
P_0 [kPa]	241
T_0 [K]	285
U [m/s]	542
Re/x [$\times 10^6$ m^{-1}]	27.6

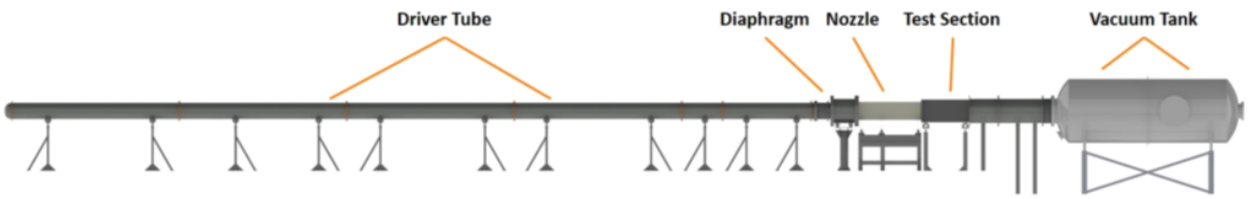


Figure 2.3: UTSI Mach 4 wind tunnel.

Table 2.3: The UTSI Mach 4 nominal operating conditions during measurements.

Tunnel Conditions	**Values**
P_0 [kPa]	448
T_0 [K]	293
P_∞ [kPa]	3.0
T_∞ [K]	69.8
U [m/s]	670
Re/x [$\times 10^6$ m^{-1}]	23.2

2.1.5 AFRL Mach 6.0 High Reynolds Number Facility

The Mach 6 High-Reynolds Facility at Wright-Patterson Air Force Base was utilized in this research effort for diagnostic development. Both LISA and Cylindrical Lens FLDI were utilized in this facility. This tunnel was chosen as for its hypersonic environment and the lack of diagnostic capabilities available to the facility operators. Of major concern to AFRL, was the limited optical access for advanced laser techniques. The goal was to introduce FLDI and LISA to this facility and show their effectiveness even with limited access under these conditions. The facility has a Mach 5.9 freestream with per length Reynolds numbers ranging from $32.8 \times 10^6\ m^{-1}$ to $98.4 \times 10^6\ m^{-1}$ with stagnation temperatures ranging from 500 K to 611 K. The core flow in the free-jet test section is 25.4 cm in diameter and 71 cm long. Run times range from 2 to 4 minutes. The facility is shown in Fig. 2.5.

2.1.6 VKF Tunnel C

To bring FLDI to a new large-scale facility, the author assisted AFRL in their fluid structure interaction experiments at VKF Tunnel C. Due to the limited release of information from this facility, only a table of run conditions used for these specific tests will be provided. The two-fold goal was to successfully deploy FLDI in a large scale VKF facility to understand the constraints of the system due to the facility and demonstrate to AEDC the viability of such a diagnostic for future consideration. For AFRL, this diagnostic gave them an off-body measurement to supplement their suite of infrared imaging, digital image correlation, and surface sensors on a flat and deformed panel. The experiments were run at Mach 4 with varied run time, from 10 seconds to 600 seconds, stagnation pressures from 55 psia to 100 psia, and stagnation temperatures from 500 °F to 1100 °F. For clarity, these conditions will be tabulated with the results in Ch. 4 as there are a significant number of run conditions.

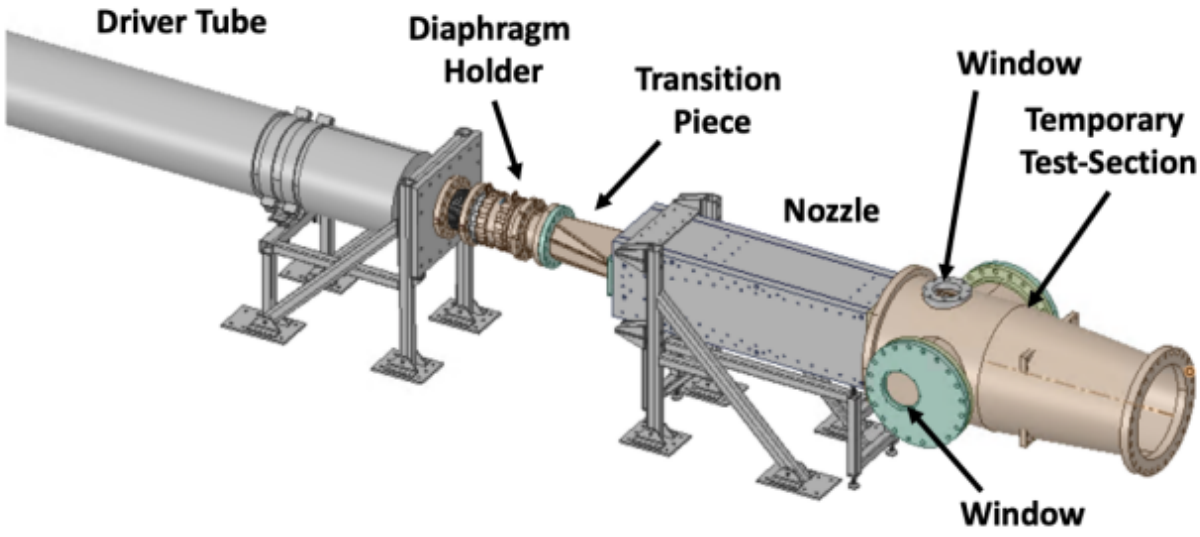


Figure 2.4: A CAD rendering of the UTSI Mach 7 wind tunnel [52]

Table 2.4: The UTSI Mach 7 nominal operating conditions during measurements.

Tunnel Conditions	Values
P_0 [kPa]	1,034
T_0 [K]	550
P_∞ [kPa]	0.25
T_∞ [K]	51
U [m/s]	1,000
Re/x [$\times 10^6$ m^{-1}]	23.2



Figure 2.5: The Mach 6 High-Reynolds Facility at Wright-Patterson Air Force Base.

Table 2.5: The AFRL M6 HRF nominal operating conditions during measurements.

Tunnel Conditions	**Condition 1**	**Condition 2**
M_∞	5.85	5.85
p_0 [MPa]	8.27	12.41
T_0 [K]	565	566
p [kPa]	6.12	9.18
T [K]	71	71
U_∞	996	996
Re/x [$\times 10^6$ m^{-1}]	60.1	90.2

2.2 Diagnostics

A number of diagnostic techniques were used throughout this work, with several overlapping across projects. This section gives a general description of each technique and the algorithms used to analyze the data acquired, leaving the experiment specific changes for the section where it was implemented.

2.2.1 Schlieren

One of the most common diagnostic techniques available, schlieren is a traditionally qualitative technique that using high-speed cameras can extract quantitative information about dominant flow features such as shocks and boundary layers. While there are many variations, the basic setup of a schlieren system commonly used in this research is the z-type setup shown in Fig. 2.6. This setup is commonly used in the UTSI wind tunnels to save space as compared to a lens-based system along with the availability of large parabolic mirrors to increase field of view. An in-house LED provides illumination capable of 100kHz operation that is collected by 200 mm focusing lens. This light is focused through an iris to simulate a point light source and is then sent to a parabolic mirror that takes the expanding light rays and collimates them. This collimated light is then sent through the test section to the other parabolic mirror of matching focal length, which focuses the light into the camera. At the light's focal point, a knife edge is placed to cut off half of the incoming light. This knife edge cutoff is the premise of schlieren and is what creates the high sensitivity of the technique. The knife edge utilizes the Gladstone-Dale relation, given in 2.1, where n is the index of refraction, k is the Gladstone-Dale coefficient, and ρ is the fluid density.

$$n - 1 = k\rho \tag{2.1}$$

This relation states that a change in density will result in a change of refractive index, n. Since n is the relation between the speed of light in the fluid with respect to the speed of light in a vacuum, changes in density will result in a slight change in the speed of light in the system. Due to the collimated light, this change in speed is seen as deflections of the once parallel light beams. As the light is focused onto the knife edge, the light rays that deflect

towards the knife edge are cut off, resulting in a darkening of the image in that location while light rays that deflect away appear as bright spots in the image. For a more in depth and comprehensive explanation of schlieren theory, the author recommends the book written by Gary Settles [53]. In this research effort, schlieren is utilized in tracking, identifying shocks, and estimating boundary layer thickness downstream of deformations. Shock tracking with schlieren has been used extensively in the HORIZON research group to extract spatial and spectral data from these interactions [54, 55, 56]. Building upon these earlier techniques, this research uses high-speed schlieren to track shockwaves from both deformed surfaces and simulated control surfaces and the boundary layer growth behind a deformation, details of which will be presented in the relevant chapters.

2.2.2 Laser Induced Schliere Anemometry

Taking advantage of schlieren's ability to view density gradients, LISA allows for even more quantitative information to be extracted from schlieren. This new diagnostic technique was introduced to high-speed wind tunnels by Lester and Gragston [36] and has been built upon in this research effort [57]. LISA uses a focused, pulsed laser beam to generate a packet of hot gas, known as a schliere, that convects with the flow and is imaged using schlieren. Since the schliere is made of hot gas, it has the same velocity as the surrounding fluid, allowing for accurate velocity measurements. A schematic of how LISA works used is shown in Fig. 2.7. It starts with a high powered, pulsed laser being focused on the plane of interest which generates a spark in the flow. This spark creates a hot pocket of gas that translates with the flow along with a blast wave that propagates from the sparked gas. These schliere are imaged with a high-speed schlieren system as previously described at a desired frame rate, giving a temporal spacing between frames of Δt. Based on a scale image taken for the given schlieren system, the distance a single schliere has moved in pixels is converted to a physical scale and used to calculate velocity. Current uses of this technique have been limited to steady, unidirectional wind tunnel facilities; however, these schliere can easily be tracked to provide flow angularity measurements as well as unsteady velocity.

Along with velocity, Mach number can be calculated using the blast wave emanating from the hot gas. In the far field, the blast wave expansion has weakened to a Mach wave,

meaning that its expansion is the speed of sound. Taking the angle made by fitting a line across the top of successive blast waves yields the Mach angle, μ and through isentropic theory, Mach angle is a direct measure of the Mach number as shown in 2.2.

$$sin(\mu) = 1/M \tag{2.2}$$

With velocity and Mach number measured, the static temperature of the flow can be directly calculated as well, using equation 2.3. The advantage of these calculation methods is that no assumption of stagnation conditions is needed, making this technique a good choice in testing the efficacy of a facility and its monitoring systems.

$$T = \frac{U^2}{\gamma R M^2} \tag{2.3}$$

A major benefit of LISA is the simple setup for the laser-induced schliere and the use of schlieren for imaging. Many high-speed wind tunnels already have schlieren imaging capabilities, which makes the technique readily accessible. Unlike molecular tagging techniques such as PLEET, an intensified camera is not needed, which reduces cost. Furthermore, laser-induced plasmas have even been used as perturbation sources in high-speed quiet tunnels [37], which means LISA can be used as method for characterizing the flow conditions in such delicate facilities.

2.2.3 Diagnostic Paint

Some of the fundamental values measured in wind tunnel facilities are pressure and temperature, which are traditionally measured using single point transducers. While highly accurate and well characterized, the major drawback is the lack of spatial resolution given by single point sensors. To characterize spatial changes in these values across a model requires a suite of sensors, incurring significant cost. Additionally, the suite of sensors still has a limited spatial resolution given the gaps between the transducers. To fill in these gaps and provide a continuous spatial measurement, diagnostic paints were developed to measure both pressure and temperature [58, 59]. These paints work by correlating changes in signal intensity to

given pressures or temperatures in a manner similar to the correlation of voltages to these values in traditional transducers.

For this research effort, the pressure sensitive paint (PSP) mixture used is the unsteady PSP developed by Innovative Scientific Solutions Inc. (ISSI) [60]. PSP operates on the principle of oxygen quenching, whereby the paint's illumination intensity changes based on the amount of oxygen present, represented by eq. 2.4 [61]. I_{ref} and P_{ref} are the intensity and pressure at the reference (wind-off) condition, I and P are the intensity and pressure at the measurement (wind-on) conditions, and A and B are calibration constants.

$$\frac{I_{ref}}{I} = A + B\frac{P}{P_{ref}} \tag{2.4}$$

Assuming the test gas is air, the fraction of oxygen present is a constant in proportion to the other elements present, so a change in pressure will yield a proportional change in the paint intensity. A schematic of how PSP works is shown in Fig. 2.8 from Gregory et al., showing the 400 nm LED illuminating the paint, which, through oxygen quenching, light between 600 and 720 nm. This is the same operation presented in later chapters, with specific setup details contained in those chapters.

A major source of error in PSP is the temperature dependence of the paint's response [62, 63]. To account for this, calibration curves were made for each set of runs. To do this, a series of images were taken at specific pressures as the wind tunnels were drawn down to vacuum. Figure 2.9 is an example of the curves made for this research effort. To ensure a relevant measurement range for the calibration curves, the measured intensities (I) for the calibration curves were taken over a range that encompassed the expected highest and lowest pressures predicted on the geometry. For each curve made, a minimum of five points were used to generate the curve. The curves themselves were made by fitting a fifth order polynomial using the native fit function in MATLAB. For expediency in processing, an average curve from all pixels was used for an entire model, but future efforts may look at generating curves for specific regions or individual pixels.

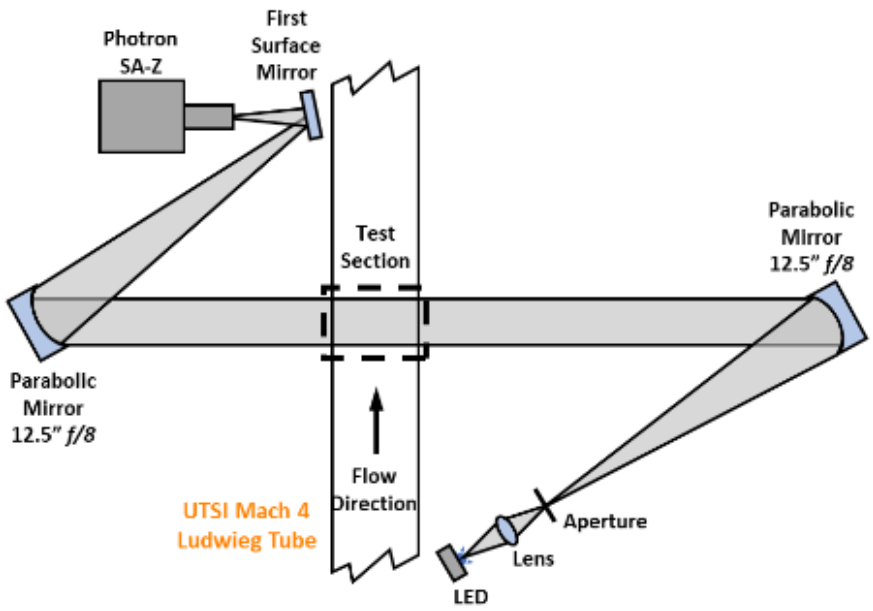


Figure 2.6: A general schematic of the Z-type schlieren setup commonly used for this research.

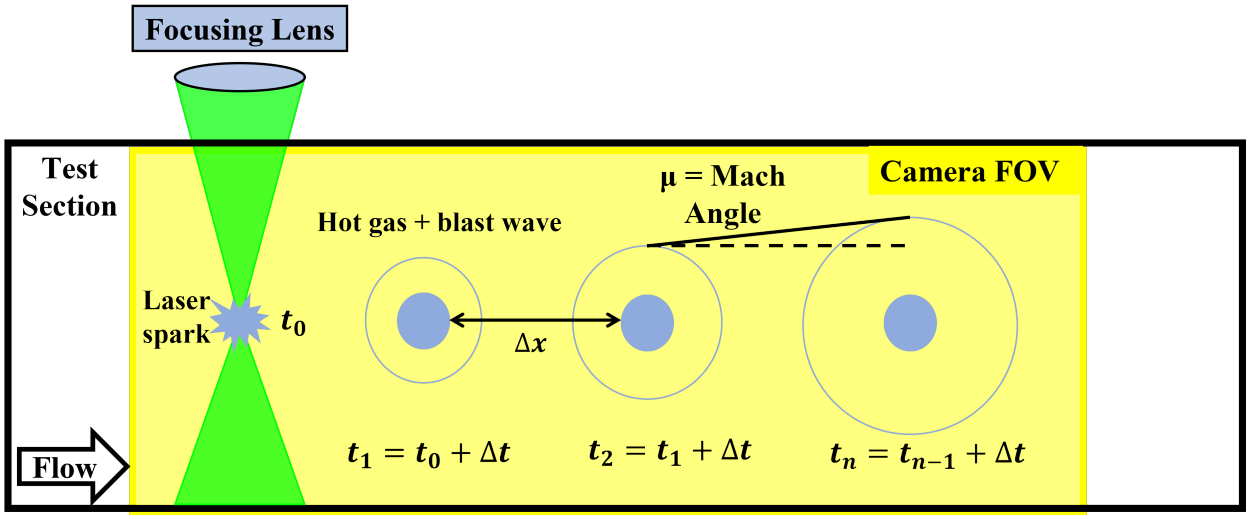


Figure 2.7: Schematic of a general LISA setup in a wind tunnel test section.

Temperature sensitive paint (TSP) operates on a similar concept but does not rely on oxygen to react, instead changing intensity based on the temperature change of the paint itself. This diagnostic has been studied for a substantial amount of time in hypersonic facilities [64]. Recently the UTSI team has introduced its use in our own facilities with promising results [65]. The formulation used at UTSI, including this research, is shown in Table 2.6. It originated from DLR [66, 67] and has been utilized in other facilities in the US [68]. Unlike PSP, TSP cannot be easily calibrated in-situ, requiring a pre-made calibraiton curve. For this work, the curve generated by Smith is used [65] since the paint used was made to the same specifications and overseen by Dr. Smith and follows Eq. 2.5.

$$\frac{I_{ref}}{I} = A + B\frac{T}{T_{ref}} \tag{2.5}$$

This curve was generated in a bench-top experiment where a model was coated in TSP and heat from a heat gun was applied. As the model heated and cooled, images were collected at various points and compared with a thermocouple that was triggered at the same time. Due to the shorter acquisition rate of the thermocouple the two diagnostics were not run simultaneously. Instead for each thermocouple measurement, an average of one hundred images was taken for the TSP. Fortunately, TSP is not pressure dependent, allowing for the calibrations to be used between multiple runs.

2.2.4 Focused Laser Differential Interferometry

Focused laser differential interferometry (FLDI) has seen a resurgence in the high-speed testing community in recent years. The technique was originally discussed by George and Smeets [35, 38] and has recently become a valuable tool in studying supersonic boundary layers. To understand how FLDI works. Figure 2.10 shows a traditional FLDI setup. This setup begins with a laser beam, which has 45° polarization, being split using a Wollaston prism, creating two beams with orthogonal polarizations and equal intensity that diverge at a small angle. Next, the beams are focused using a lens, which yields two small points with a beam separation distance Δx. This split is best visualized in Fig. 4.17, where Δx is the beam spacing. To expand the capabilities of traditional FLDI, a diffractive optical

element (DOE) can be dropped into the system, creating an array of measurement pairs with a specific spacing between the measurement pairs. After the focus, the beams are collected by a lens, made co-linear using another Wollaston prism, and finally through a polarizer, causing the beams to interfere. As disturbances propagate through the beam path, small changes index of refraction occur, resulting in fluctuations of the fringe pattern, which is captured by a photodetector. However, a key aspect of FLDI is that only disturbances near the focus contribute significantly to the signal. This effect is brought about by the fact that two beams in the system share mostly share a common optical path except near the focus, which means the highest change in phase will occur is a disturbance propagates near the focal region.

The multiple measurement pairs in Fig. 2.11 highlight one of the advances made to the traditional FLDI system. Multiple researchers have explored increasing the number of beam pairs. This is usually done by adding an additional Wollaston prism into the setup [44]; however, a DOE allows for an arbitrary number of FLDI beam pairs. This technique is Linear Array-FLDI and has been used extensively by the HORIZON research group including this author [41, 69, 70, 71]. However, increasing the number of points limits the ability to detect each of the signals. Current configurations rely on the use of multiple photodetectors, increasing the complexity of system alignment along with the cost of the overall system [71].

To alleviate this, further investigation has been done into the use of cylindrical lenses in an FLDI setup [50, 72]. This configuration avoids clipping of the signal as the measurement moves closer to a model surface and avoids the gap between the discreet points generated by spherical lens FLDI, giving a continuous signal across a line. Figure 2.12 shows what a cylindrical lens FLDI signal looks like at the focal point. This configuration shows a substantial beam height relative to the beam width.

A drawback to this setup is the increased signal size at the focal point. Current photodetectors are only able to collect and average the entire signal, effectively rendering the beam measurement as an average signal over its entire height. The current research effort explores using a camera to image the entire signal and extract quantitative data across each portion of the signal. If successful, it would allow for thin boundary layer measurements using

the change in spectral content across the signal, bypassing the lack of traditional boundary layer measurement techniques available in many large scale and impulse facilities.

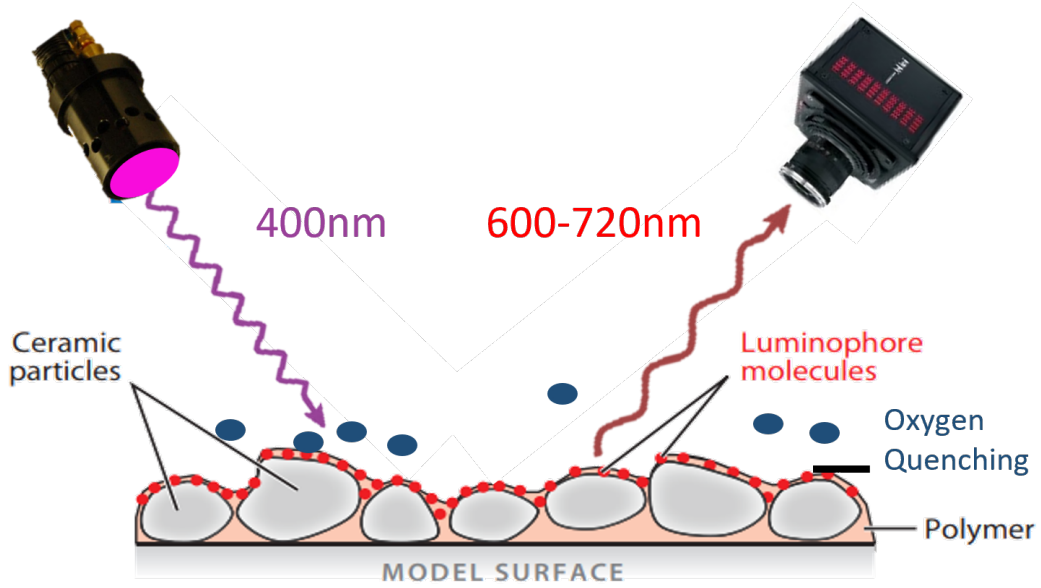


Figure 2.8: Diagram of PSP's operation [61]

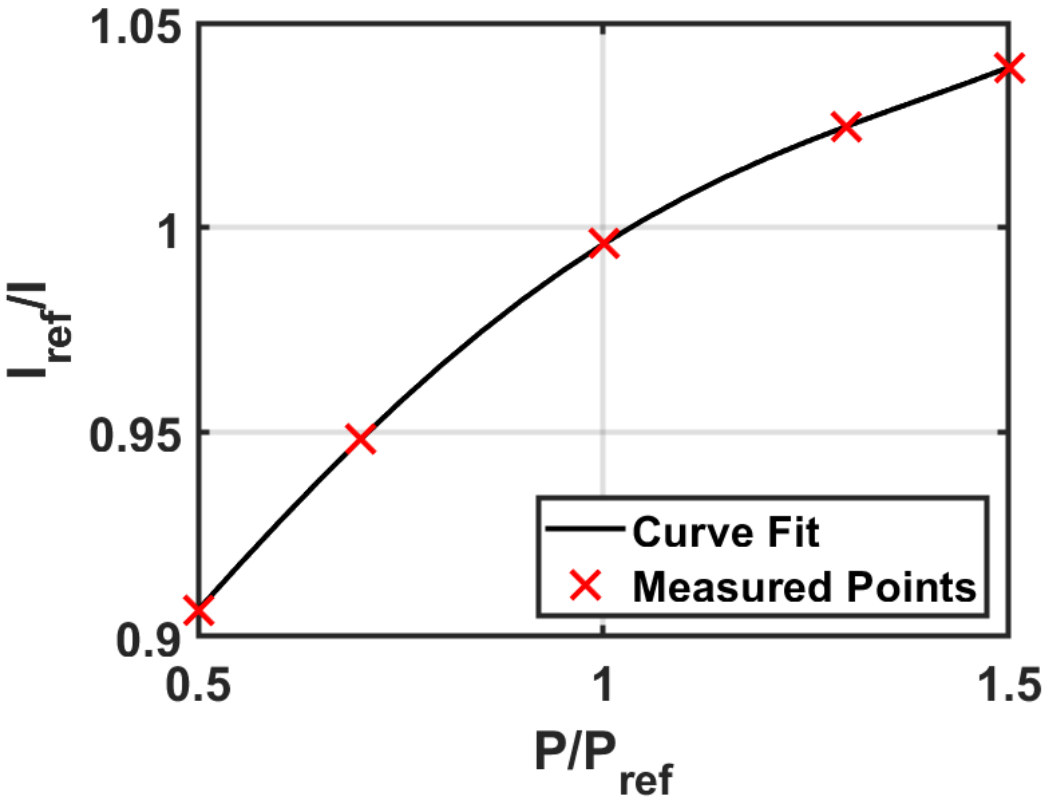


Figure 2.9: Sample calibration curve from the current research effort

Table 2.6: DLR temperature sensitive paint formulation used at UTSI [65]

Component	Amount	Amount x 50	Amount x 3.5
Ru(phen)	71.2[mg]	3,560 [mg]	249.2 [mg]
Polyacrylic Acid	10 [mL]	500[mL]	35 [mL]
Ethanol	20 [mL]	1,000 [mL]	70 [mL]
Polyurathane White	Coat Model	Coat Model	Coat Model

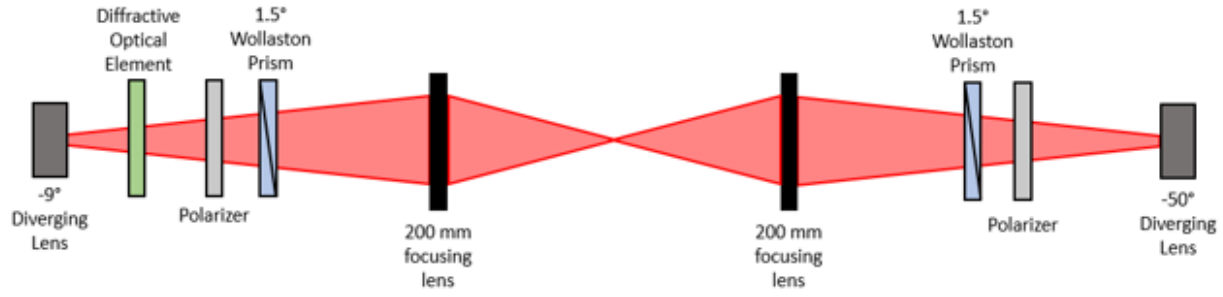


Figure 2.10: Schematic of a traditional FLDI setup.

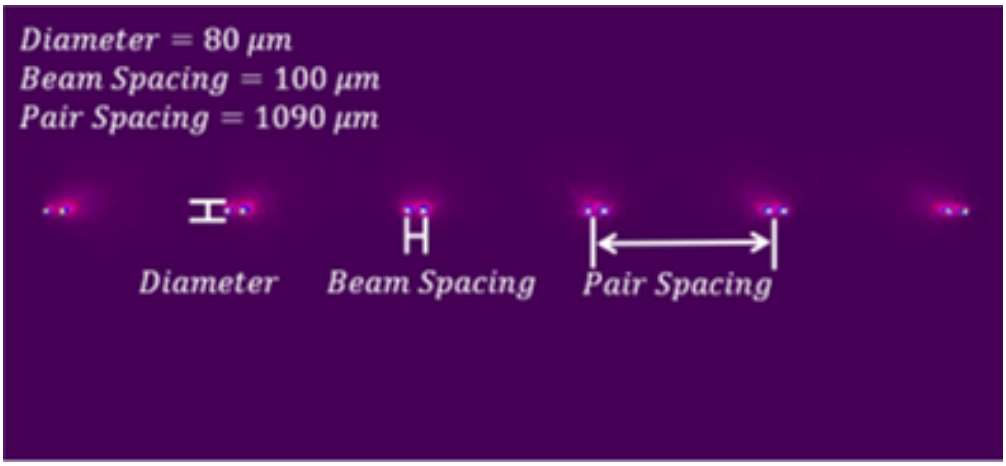


Figure 2.11: Spherical lens FLDI signal at the focal point.

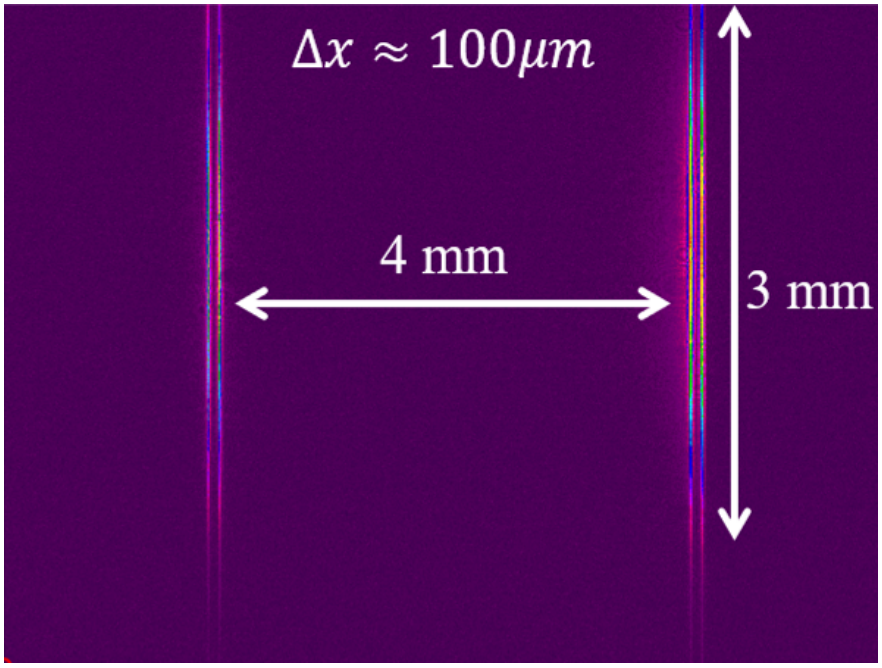


Figure 2.12: Cylindrical lens FLDI signal at the focal point.

Chapter 3

Fluid Structure Interaction Research

For all the deformation setups studied here, there were three primary assumptions applied. The first was that each deformation would be static instead of dynamic. This assumption is from the difference in timescales between structural vibration that is on the order of 1 kHz at its maximum and the standard fluid scales being an order of magnitude higher on the low end. While not explicitly stated, multiple prior researchers utilized this assumption during their work [73, 6, 74, 4]. The second assumption utilized was that each deformation would take the shape of a first mode panel deformation. Though panels deform at multiple modes, the first mode is the primary deformation shape that is seen. The addition of multiple first mode deformations is to account for large panels that have multiple deformed regions when buckled. Although these appear to be second mode deformations, in this research, they are treated as a combination of first mode deformations. The final overarching assumption is that deformation amplitudes must be smaller than that of the boundary layer thickness. This assumption separates structural deformation from control surfaces and geometric additions such as hemispheres. For the work presented here, the largest deformation reaches around half of the present boundary layer thickness.

3.1 Initial Experiments

The first experimental efforts in understanding the downstream effects generated by a deformed panel in the floor of the UTSI Mach 2 wind tunnel upstream of a cylinder shock

generator, illustrated in Fig. 3.1 below. The leading assumption was that the cylinder generated SBLI would function as an amplifier for the deformation generated effects, and subsequently shed light on what impacts these effects would have on a control surface. Due to facility constraints, the panel was limited in its dimensions, being only 2 inches wide by 3 inches long. It would be deformed by a rod placed below the tunnel pushing and pulling on the underside of the panel. This would yield a deformation identical to a first mode panel deformation while also keeping the amplitudes in a reasonable range. Initial deformation testing of the panel showed a maximum elastic deformation of 1.5 mm. With an 11 mm boundary layer on the floor of the Mach 2 tunnel, the amplitude of deformation was significantly smaller, keeping within the amplitude constraints. The first round of experiments utilized high speed schlieren along with pressure transducers to study the cylinder SBLI behavior when the upstream panel was deformed. Both diagnostics were sampled at 100 kHz to allow for sufficient spectral resolution. Figure 3.2 shows the locations and pressure time histories of the different pressure transducers.

For each configuration, the pressure magnitude did not change for each position. This is expected as the deformation is too small to generate a substantial shock capable of increasing the downstream pressure. To identify possible changes, the spectral content between deformation types was compared. Even with the most extreme deformations, the pressure transducer underneath the shock foot showed no discernible change in the dynamics of the interaction downstream of the panel as shown in Fig. 3.3.

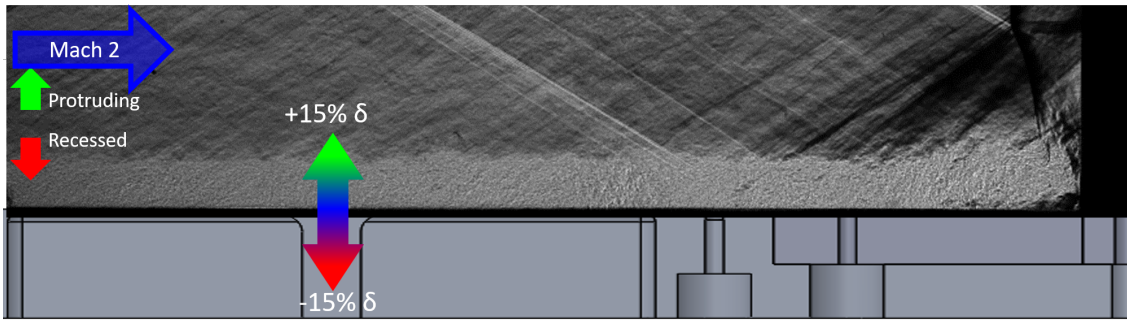
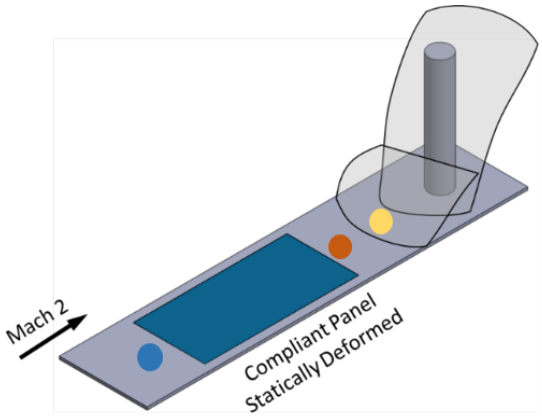
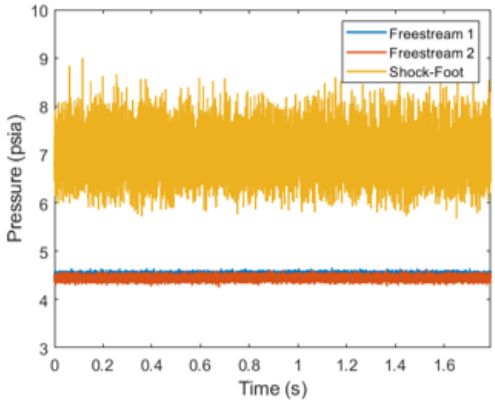


Figure 3.1: A schematic of the Mach 2 FSI experimental setup



(a) Location of each transducer relative to the panel and cylinder SBLI



(b) Pressure time history for each transducer.

Figure 3.2: UTSI Mach 2 pressure transducers.

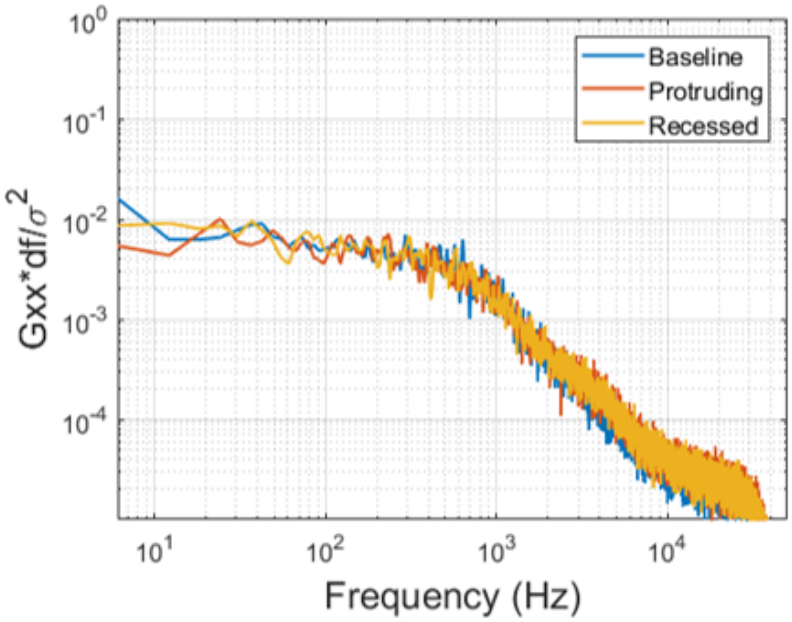
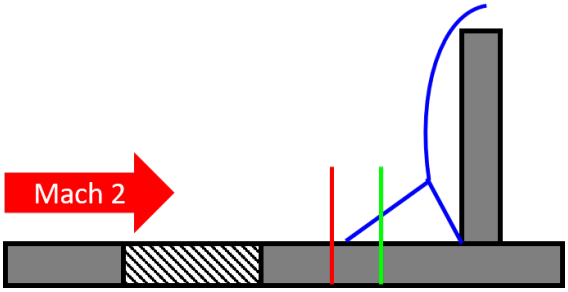
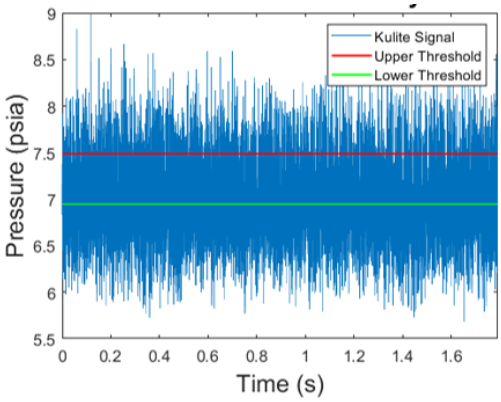


Figure 3.3: Spectral content of the shock foot kulite for the various deformed configurations



(a) Schematic showing the spatial thresholds for the zero crossing calculations



(b) Pressure time history with the zero crossing thresholds highlighted.

Figure 3.4: Zero crossing frequency.

Table 3.1: Zero crossing frequency of the shock foot calculated from the pressure time history of the shock foot transducer. Frequencies are in Hz, the upper threshold is $1.5\sigma + P_{mean}$, and the lower threshold is P_{mean}

RunNumber	**Baseline**	**Protruding**	**Recessed**
1	3778	4834	4506
2	3954	4739	4504

To get a more complete understanding of the shock foot dynamics from the pressure transducers, the zero-crossing frequency of the shock foot was calculated. The zero-crossing frequency, f_z, is calculated by counting the number of times the shock foot crosses over the transducer in a given time period. For a pressure transducer, a cross is defined by a pressure increase above a certain upper threshold value, indicating the shock is over the transducer and by the pressure decreasing below another, lower threshold value, indicating the shock is downstream of the transducer. This concept is indicated in Fig. 3.4 both spatially in Fig. 3.4a and temporally in Fig. 3.4b. The results of this calculations are tabulated in Table 3.1, with each deformation case showing an increase in shock foot unsteadiness. While not conclusive, this result points to an impact from an upstream deformation.

To corroborate the possible findings in the pressure data, shock tracking was used in the schlieren videos. For brevity in this report, the shock tracking algorithm used relies on bianarizing each schlieren frame to isolate the shock foot, then fitting a line to the front of the shock, and finally reporting the lowest point of that line for each frame. Figure 3.5 illustrates this, with the fitted line overlaid on a schlieren frame. From the saved shock foot locations, spectra and mean positions can be calculated. The spectral content from the shock tracking mirrored that of the pressure transducers, corroborating the earlier findings.

The mean shock foot location for each deformation condition is plotted in Fig. 3.6. The results show a potential relationship between the presence of a deformation and a corresponding change in shock foot location. The recessed case shows an extension of the shock foot while the protruding case shows the shock foot receding closer to the cylinder. These results are not conclusive as the change in measurement location is around three pixels, too close to the resolution bounds to be considered definitive. Given that pressure transducers are single point measurements, time of the shock over the transducer does not yield any information useful to corroborating these findings. Based on the inconclusive nature of the data gathered during this experimental effort, the research efforts were focused more on identifying the downstream effects from a deformation first, before quantifying their impact on a control surface. This shift in focus led to a redesign of the full effort which will be discussed in the subsequent sections.

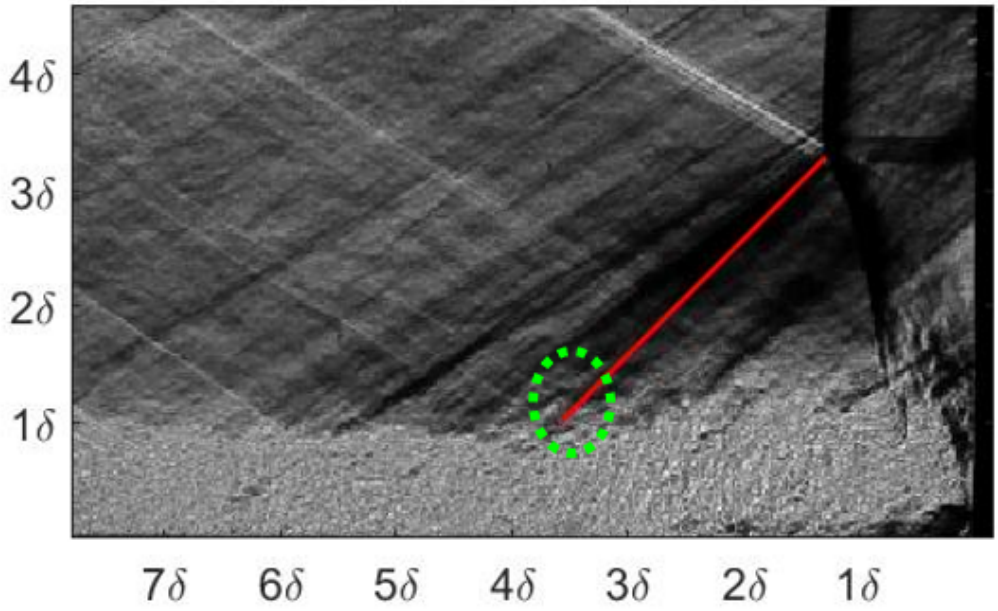


Figure 3.5: Shock tracking overlay on an instantaneous schlieren frame

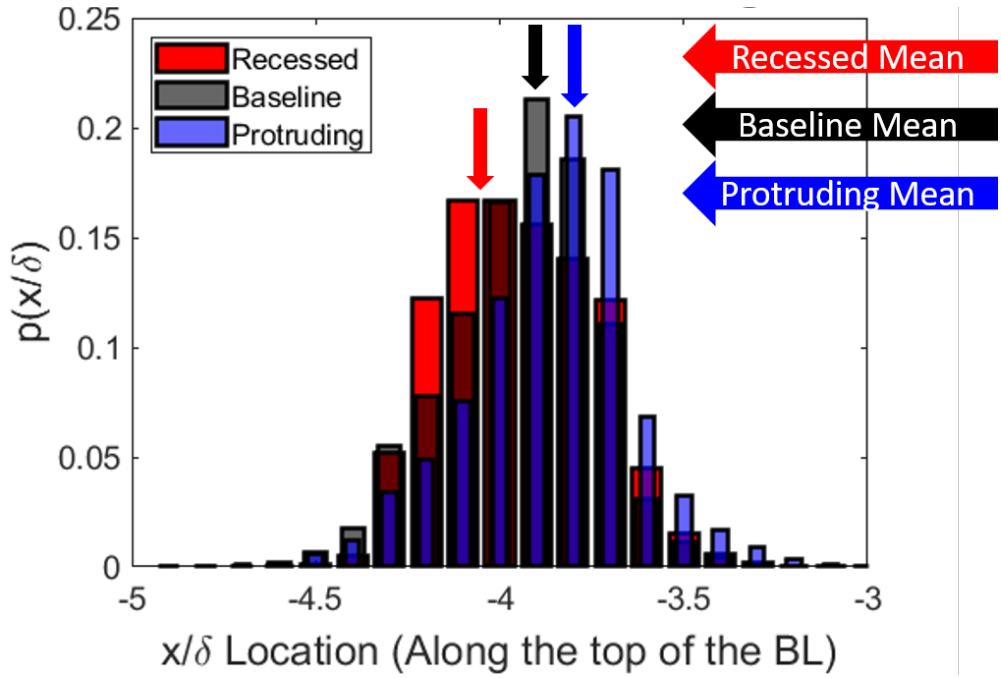


Figure 3.6: Histogram of the mean shock foot location for each deformation case.

3.2 Static Deformations on a Hollow Cylinder

Due to the difficulty of measurement across three dimensional models, the decision was made to study the problem in a two-dimensional manner. This led to the experiments shifting from the floor of the UTSI Mach 2 to a hollow cylinder in the UTSI Mach 4 Ludwieg tube. This section will discuss the experiments used to characterize the chosen models and draws heavily on the AIAA Scitech paper written by the author on these efforts.

3.2.1 Models

To evaluate the downstream effects of surface deformations, models of varying deformation complexity were produced. The models were sinusoidal deformations with constant height and curvature, with each model varying in shape and complexity relative to the others. Figure 3.7 shows a picture of each model along with the naming convention used for the shape. The change in color between the mode 1 and mode 2 models is a result of the mode 2 models being 3-D printed instead of machined. Each model was designed to fit a hollow cylinder to isolate the 2-dimensional, streamwise effects for later comparison with 3-D models with the same scaling.

To get a better understanding of the model scaling. Figure 3.8 shows a schematic of the sinusoid used to design the models. A major consideration in sizing the models was to make the leading inclination steep enough to induce a response but not so much that it breaks structural limits. Based on prior work [24, 6, 23], the deformation shape could be described by Eq 3.1.

$$\frac{2a}{\lambda} = 0.053 \tag{3.1}$$

Each of these prior works used a sinusoidal assumption for their deformations so their length to amplitude ratio still holds. This equation is consistent for both mode 1 and mode 2 sine waves, hence why it was used. To keep the deformation scaled appropriately, I imposed a condition that the deformation amplitude could not exceed the boundary layer thickness. For this work, the amplitude of the deformation was 1.8 mm, yielding a half wavelength of 34

mm. Compared to the model boundary layer thickness of 4 mm, this gave me a comfortable amplitude to boundary layer thickness ratio of 0.45, well within our desired parameter.

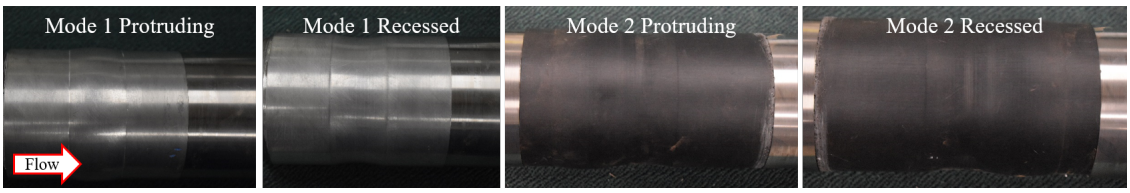


Figure 3.7: Images of the models used in this investigation

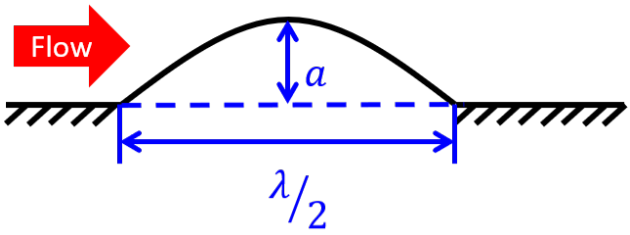


Figure 3.8: Schematic of the model shape with relevant dimensions labeled.

3.2.2 Results and Discussion

To understand the flow field around these deformed surfaces, high-speed schlieren was used to identify the major structures of the flow field, particularly the boundary layer edge and the emanating shocks. These features were identified using the contrast provided by schlieren and compared with the theoretical baselines. Figure 3.9 shows an average schlieren image of the Mode 1+ deformation with the key features highlighted. As will be the case with subsequent schlieren images, the emanating shocks are highlighted by the yellow and green dashed lines while the boundary layer edge is highlighted by the red and blue lines. The blue dashed line is the theoretical turbulent boundary thickness from White's Viscous Flow book. The red line is the boundary layer thickness estimated from schlieren. For the Mode 1+ deformation, there are two shocks that form, a strong leading-edge shock, highlighted n yellow, and a weaker trailing edge shock, highlighted in green. There is also an expansion at the apex of the deformation that is not highlighted. These shocks suggest pressure changes across the deformation and potentially downstream. The boundary layer measurement shows no deviation from the theoretical expectation. The lack of change in growth rate is not unexpected as the incoming boundary layer is turbulent, but the recovery one panel length downstream of the deformation back to the thickness that would occur with no deformation highlights the resiliency of the boundary layer to this disturbance. Figure 3.10 shows the same type of schlieren image for the Mode 1- deformation.

For this recessed deformation, the front of the model starts with an expansion as the deformation begins. Towards the end of the model, a substantial shock is formed. The foot of this shock protrudes towards the center of the deformation, indicating a separation in the trough. Figures 3.11 and 3.12 show the schlieren images for the mode 2 deformations. In Fig. 3.11, the positive deformation generates a shock on the leading edge and on the back end coming out of the recessed portion. Compared to the mode 1 cases, the leading shock is similar to the Mode 1+ deformation as is the trailing shock to the Mode 1-. This indicates a possible cumulative effect from the combined deformations. Figure 3.12 shows the Mode 2- configuration, dominated by one shock emanating from the recessed portion. Due to the protruding deformation being directly connected to the recessed portion; the

shock is stronger than those in other cases. Again, the boundary layer estimations for both cases show a complete recovery within a panel length downstream of the deformations. Due to the complexity of the flow field near the end of the deformations, the boundary layer estimations could not be confidently made within a panel length of the deformed section.

To determine the extent of downstream impact in the boundary layer, LA-FLDI was run one panel length downstream of each deformation. The choice of one panel length was driven by the idea that if there was no discernible difference that far downstream, then the impact to downstream vehicle structures would be also be indiscernible. Figure 3.13 shows how the FLDI measurements were oriented relative to the deformation. The beam pairs were placed as close to the surface as could be confidently measure, which was around 2 mm. Based on the FLDI setup, the measurement points had 1 mm between them, giving a total measurement range of 5 mm between the furthest points.

To ensure the FLDI measurements were in the boundary layer, baseline runs were taken comparing the freestream and model spectra, shown in Fig. 3.14. The black line is the freestream signal while the red line is the model. Both measurements were taken at the same point in the tunnel, with the model being taken out for the freestream run. The model signal shows a clear change in the higher frequency, indicating that the signal was immersed in the turbulent boundary layer. This is further corroborated by the peak in the turbulent spectra occurring near the anticipated characteristic frequency of the boundary layer at that point. The characteristic frequency was calculated using the calculated freestream velocity from isentropic theory divided by the measured boundary layer thickness from schlieren. Since there was no measured pressure increase downstream of the deformations from PSP, the local Mach number and velocity were assumed to be the same as those upstream of the deformation.

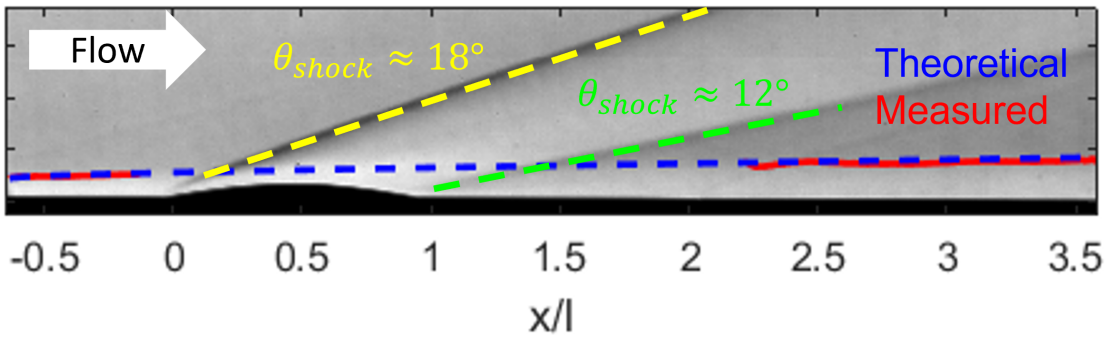


Figure 3.9: Mode 1+ deformation

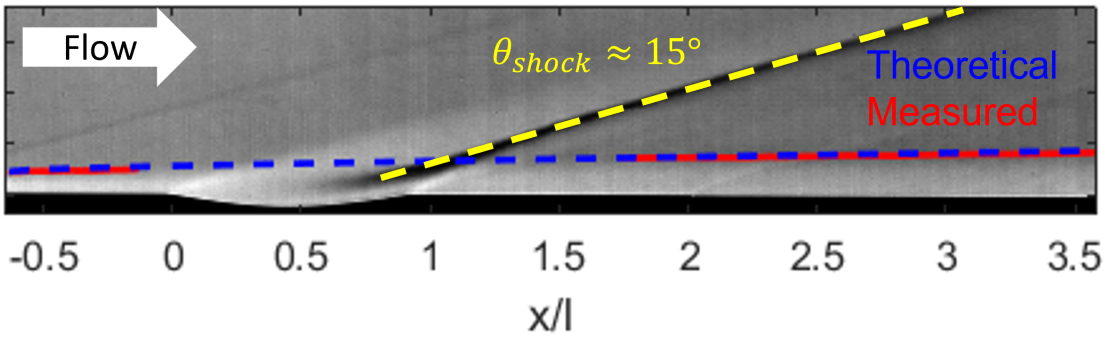


Figure 3.10: Mode 1- deformation

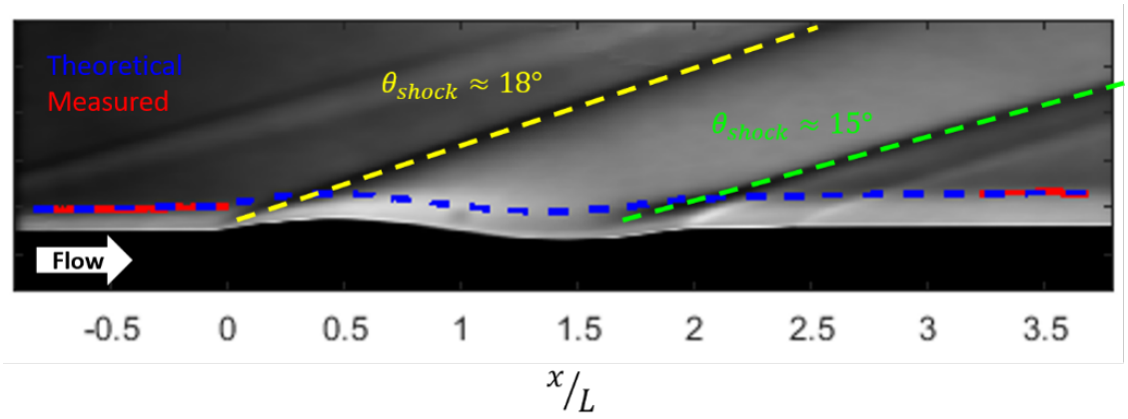


Figure 3.11: Mode 2+ deformation

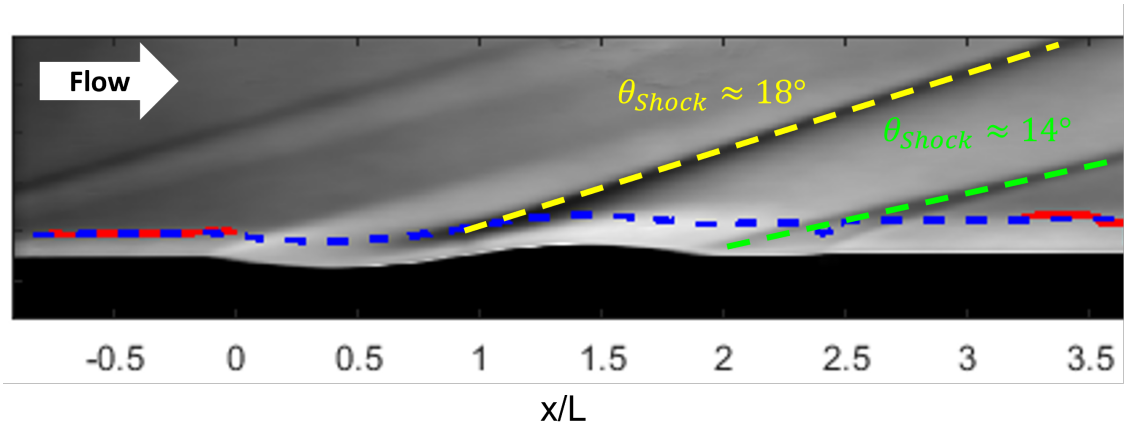


Figure 3.12: Mode 2- deformation

Fig. 3.15 compares the spectra downstream of the mode 1 deformations to the baseline mode 0 condition. In each case, there is no discernible difference between the downstream spectra. While there was no expectation that the spectrum's shape would change, the consistency of the turbulent energy distribution was somewhat unexpected. A noted drawback in these measurements is the 2 MHz sampling rate not resolving the higher frequencies.

While the addition of measurement points detracted from the overall sample rate, it did allow for the measurement of convective velocities within the turbulent boundary layer. These values are compiled in Table 3.2. To illustrate that these are not the actual fluid velocities, the theoretical freestream velocity has been included as a comparison, showing the lag in convective velocities. For the flat model, the mode 1 deformations, and the Mode 2+ deformation, the convective velocities are the same. Each shows a deficit from the measured freestream value, further confirming the measurement's immersion in the boundary layer. The Mode 2- case, however, shows a further deficit in its convective velocity, indicating a lasting effect in the downstream boundary layer. To identify the cause of this lag, the normalized convective velocities were plotted against the turbulent boundary layer velocity profiles generated by Sun and Childs' extension of the original Spalding velocity profile [75]. In Fig. 3.16, the solid black line shows a traditional velocity profile for an undisturbed turbulent boundary layer. The red x is the normalized convective velocity profile for most deformed cases. These points are in good agreement with the profile for the measured 0.5δ beam height. The dashed line shows the velocity profile of a turbulent boundary layer downstream of a separation. The overlapping blue x is the normalized convective velocity for the Mode 2- leading case, indicating that the boundary layer undergoes a significant separation in the trough of the deformed section. Even though the shape is the exact mirror of the Mode 2+, the orientation of the deformation relative to the flow plays the critical factor.

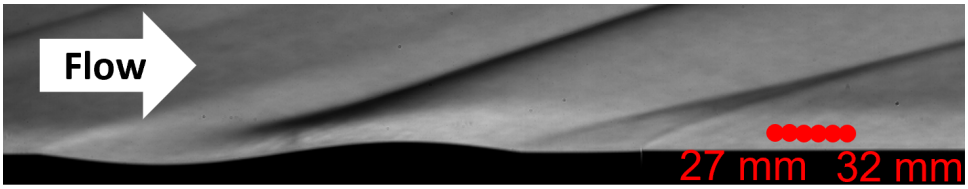


Figure 3.13: Spectra from the LA-FLDI system

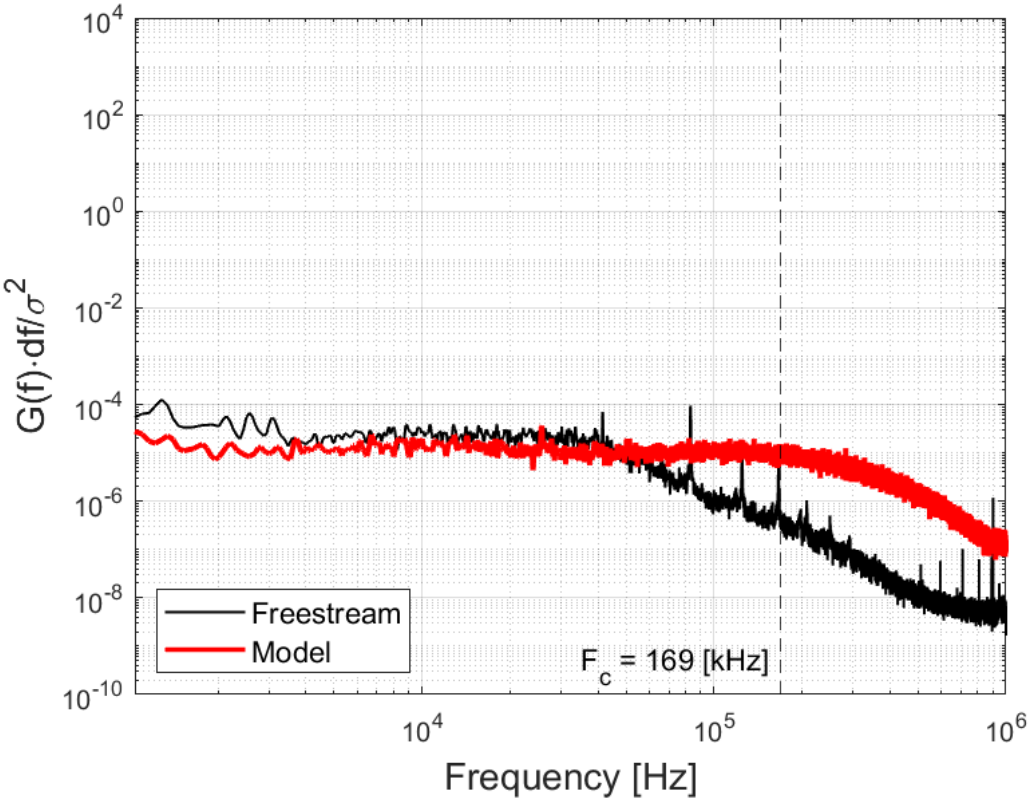
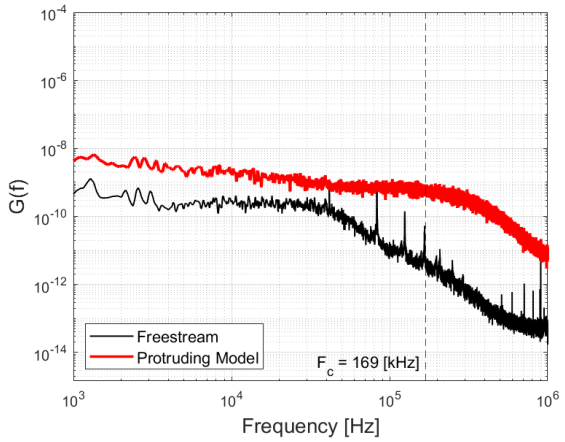
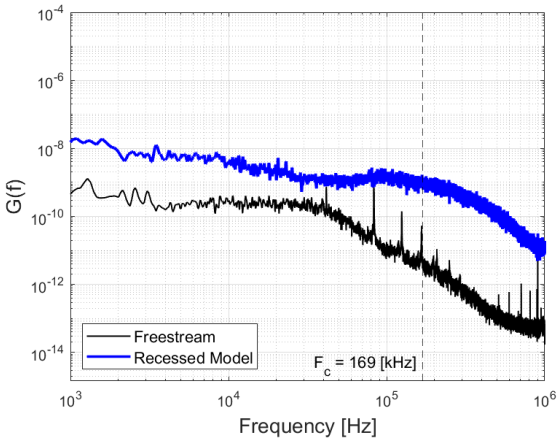


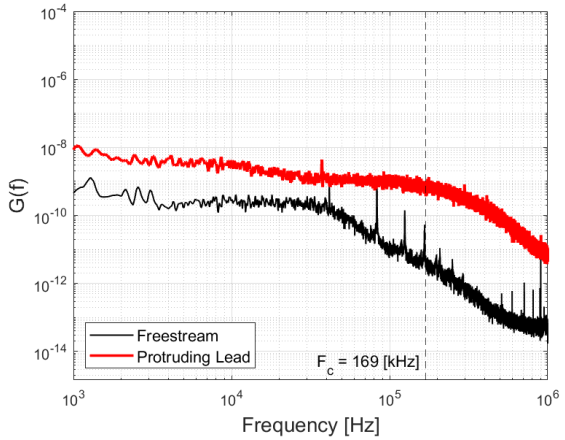
Figure 3.14: Spectra from the LA-FLDI system



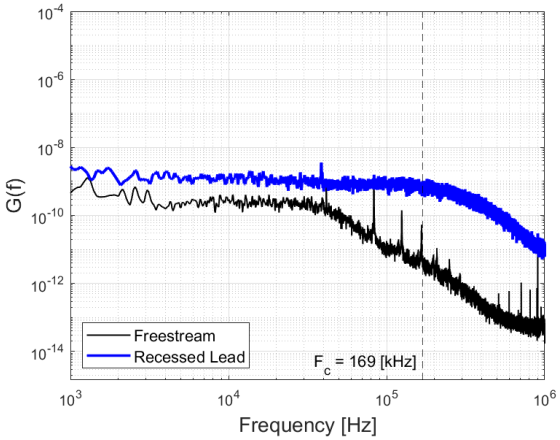
(a) Mode 1+ deformation



(b) Mode 1- deformation



(c) Mode 2+ deformation



(d) Mode 2- deformation

Figure 3.15: Downstream spectra for the various mode deformations compared to the baseline mode 0 undeformed model

Table 3.2: Convective velocity measurements downstream of each deformation condition

Model Case	**Velocity [m/s]**	U/U_{fs}	**Uncertainty [m/s]**
Isentropic Freestream	677	0.956	43.2
Measured Freestream	641	0.900	38.9
Mode 0	605	0.944	34.7
Mode 1+	605	0.944	34.7
Mode 1-	605	0.944	34.7
Mode 2+	605	0.944	34.7
Mode 2-	573	0.894	31.3

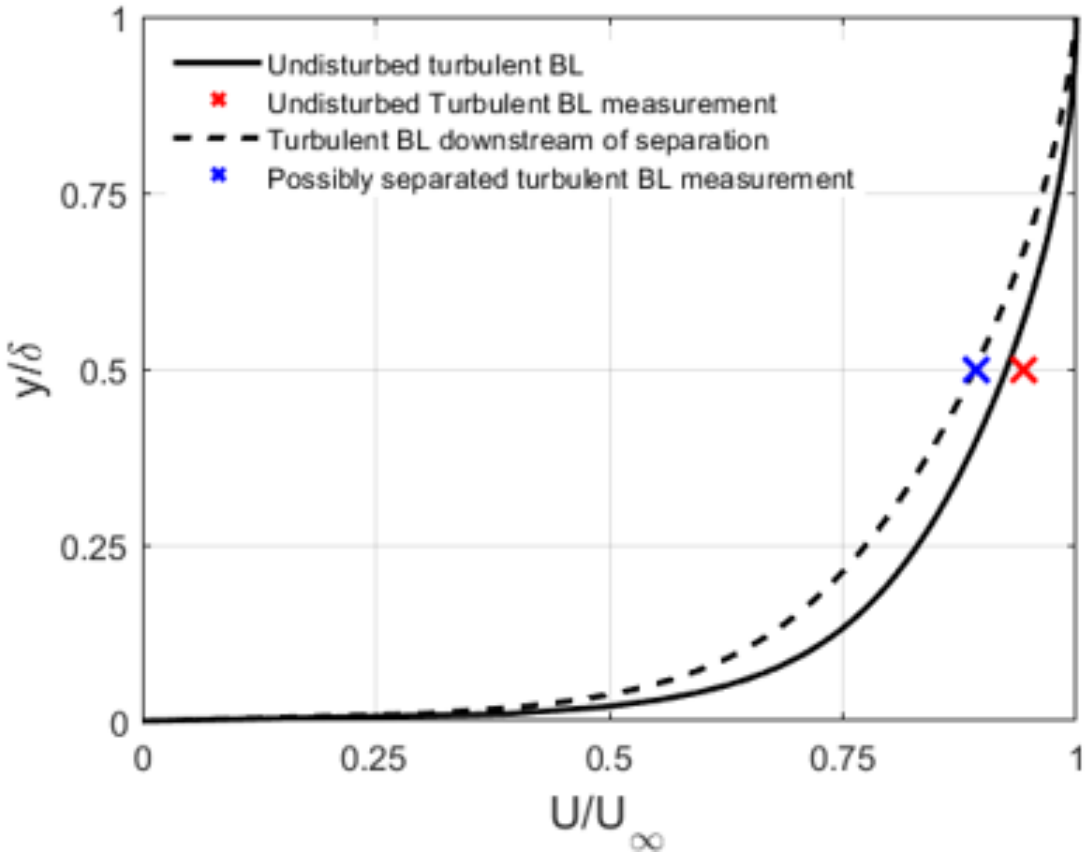


Figure 3.16: Normalized convective velocity measurements compared to the theoretical velocity profiles for undisturbed and previously separated turbulent boundary layers

To further characterize the sinusoidal deformations, pressure measurements were made using fast response PSP across the deformed surfaces. This allowed for a full field pressure map with no measurement gaps across each deformation. Figure 3.17a shows the full field coefficient of pressure, C_p mapping for the Mode 2+ configuration. The extreme C_p values at the edge of the cylinder are not flow features but are instead distortions caused by the motion of the model during the run and the extreme curvature away from the sensor at the edges of the model. Figure 3.17b shows a centerline profile of the C_p values with corresponding theoretical and computational C_p results for the same configuration and conditions. The theoretical results come from small perturbation theory outlined in Chapter 8 of "Elements of Gasdynamics" [3], where Eq. 1.6 from earlier is simplified to Eq. 3.2.

$$C_p = \frac{2a\alpha}{\sqrt{M_\infty^2 - 1}} \cos \alpha x \tag{3.2}$$

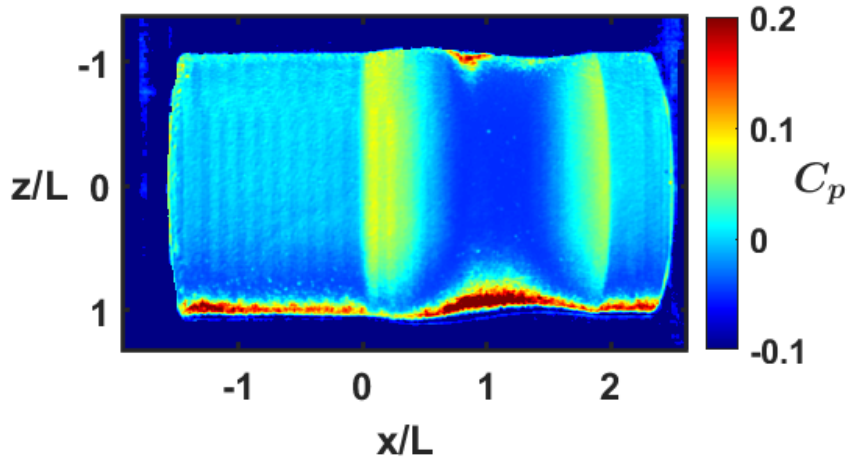
This equation is represented by the black line labeled as Linear Theory in Fig. 3.17b, and compares well with the experimental and computational results, highlighting that at Mach 4, linear theory still holds and the deformation does not yield and appreciable impact to the flowfield. The computational results are courtesy of Aaron Becks from the Ohio State University, who utilized an in-house Reynolds Averaged Navier-Stokes (RANS) code to simulate these experimental conditions. His CFD results match the experiments, with the first pressure rise being slightly over predicted and the latter under predicted, but still maintaining the correct distribution, particularly the narrow pressure rise at the trailing edge of the deformation.

For the Mode 2- case, the C_p distribution and profile are shown in Fig. 3.18, where the mapping. Figure 3.18a, shows a significant spike in pressure approximately $0.9x/L$ along the deformation. This is highlighted in Fig. 3.18b, where the experimental data shows a strong peak at that location. Linear theory markedly under predicts the peak C_p values along with over predicting the magnitude of pressure loss in the regions at the edges of the deformation. The computational results fare better, particularly in the regions of low pressure; however, these results still under predict the peak pressure load. This divergence from theory and computations with the substantially increased pressure indicates that the Mode 2- case

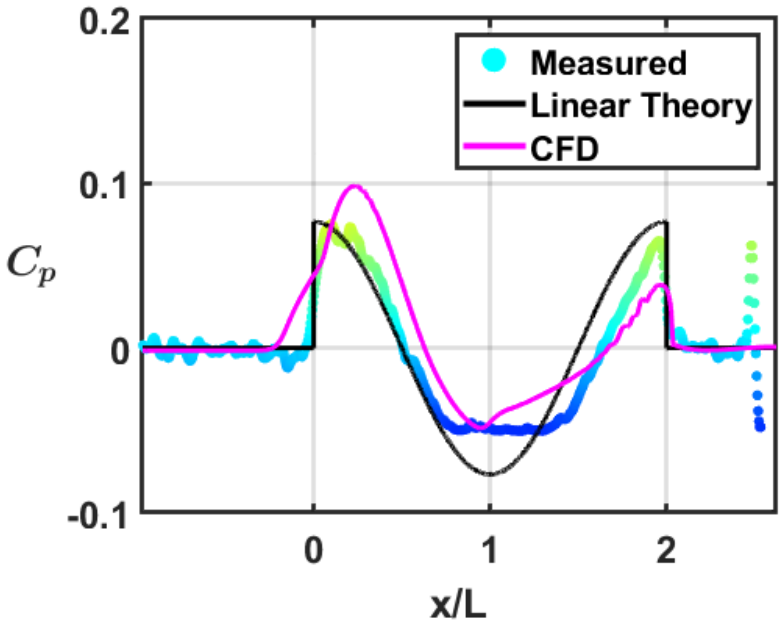
has separated in the trough, unlike the Mode 2+ case, even though the flow angles are the same between the two configurations. This indicates that there is a height condition required to induce boundary layer separation along with the known angle dependency. For the protruding case, the maximum height Δy travel for the boundary layer is $0.5\delta_{99}$ while the maximum Δy travel in the recessed case is $0.9\delta_{99}$. While the $\Delta y = 0.9\delta_{99}$ height is tempting to consider as a condition for separation, more study must go into this phenomenon as there is a dependency with incident angle that must be taken into account.

3.2.3 Conclusions

Sub-boundary layer thickness panel deformations were characterized, and their downstream effects were measured using schlieren, PSP, and LA-FLDI. Schlieren images show that the downstream boundary layer recovers within one panel length of the deformation, though the change before that is uncertain from this measurement. These images also show that even though these deformations are sub-boundary layer thickness, they still produce significant shocks. The pressure data shows that these shocks do not produce a lasting pressure increase downstream of the deformations, containing their immediate effect to the local region. However, their prominence in schlieren indicates that these are not insignificant waves and have the potential to impact downstream control surfaces. PSP across each deformation is bolstered by matching the theoretical expectation from linear theory and CFD for the Mode 2+ case. In the Mode 2- case, the pressure data diverges from theory and computations, indicating a separation in the trough of the deformation. Given that both deformations had the same sinusoidal shape, the separation was caused by the difference in wall normal travel for the boundary layer from the trough of the deformation to the peak on the downstream side. The spectral measurements from LA-FLDI likewise showed no significant changes downstream of any deformations. The convective velocities: however, showed a change downstream of the Mode 2- that is consistent with the change expected downstream of a separated region, adding a second measurement showing a change downstream of the Mode 2-case.

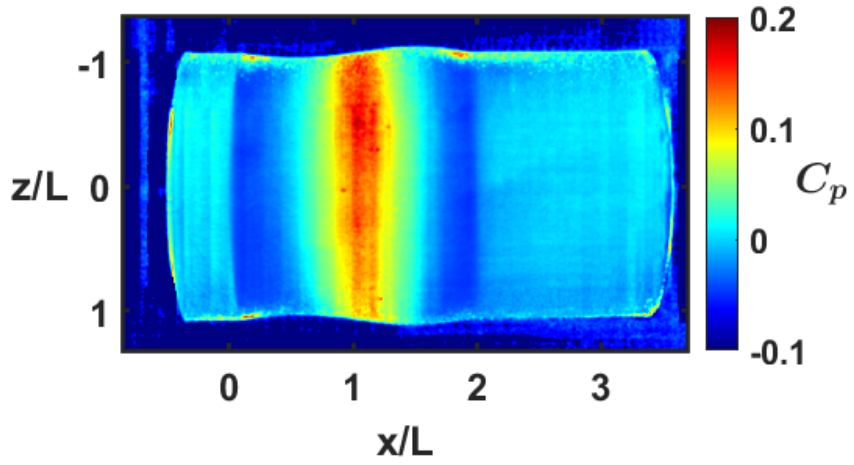


(a) C_p map

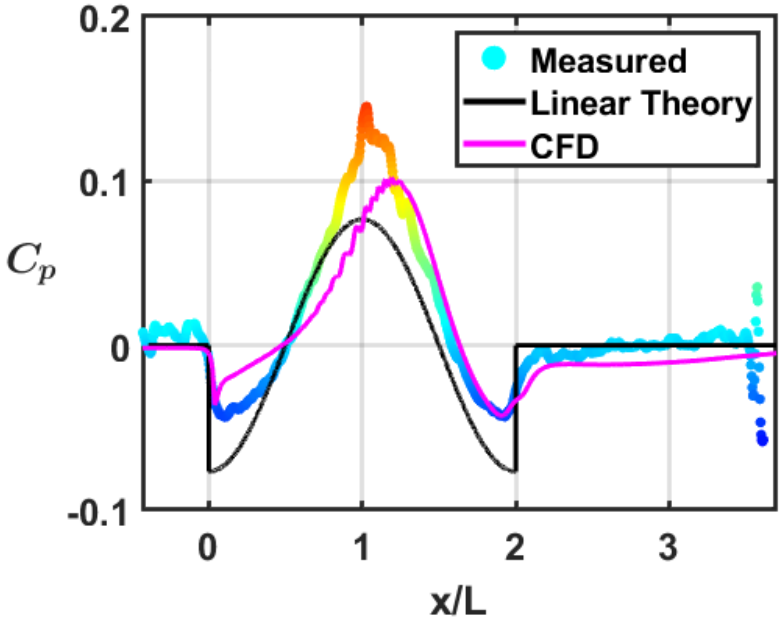


(b) Centerline C_p

Figure 3.17: Coefficient of pressure for the Mode 2+ case.



(a) C_p map



(b) Centerline C_p

Figure 3.18: Coefficient of pressure for the Mode 2- case.

3.3 Downstream Impacts on a Control Surface

To build on the measured effects from a static deformation, the next set of experiments focused on characterizing the impact of the propagating shocks on a flare downstream of a deformation. To achieve a more favorable shock angle from the deformation shock, the UTSI Mach 7 wind tunnel was utilized in these experiments. This section is pulled directly from the author's pending journal paper.

3.3.1 Experiment Setup

Model Configuration

Fig. 3.19 shows the model used, which consisted of a hollow cylinder with a tripped leading edge, attached to a flare at the end. Due to the low Reynolds number in the facility, the boundary layer does not naturally transition along the length of the model, so trips were employed at the leading edge to induce turbulent flow. These trips follow the design recommendations of Semper and Bowersox [76] for trip sizing in Eq. 3.3, yielding a trip height of 3 mm.

$$h_{trips} = 1.33 \cdot \delta_{99} \tag{3.3}$$

The leading-edge boundary layer thickness was measured using schlieren taken during the initial characterization of the hollow cylinder in this facility, which yielded a boundary layer thickness of $\sim 2.5mm$. To ensure the trips had a minimal effect on the desired interactions, the trips were placed 355 mm (14 in) from the flare juncture. The minimum distance from the trips to the deformation was 285 mm (11 in), keeping the desired interaction far away from the trips to allow the post-trip, turbulent boundary layer to recover. The flare had an angle of 30°, with a length of 110 mm (4.33 in), and a radius of 63.5 mm (2.5 in), producing a separation shock with an angle of 35°. The deformation was sized and scaled using the same procedure as the previous work this effort extends [77]. For these experiments, the deformation was a Mode 1+, whose height and length are defined by Eq. 3.4, where a is the deformation amplitude and λ is the wavelength. Based on schlieren estimates of the

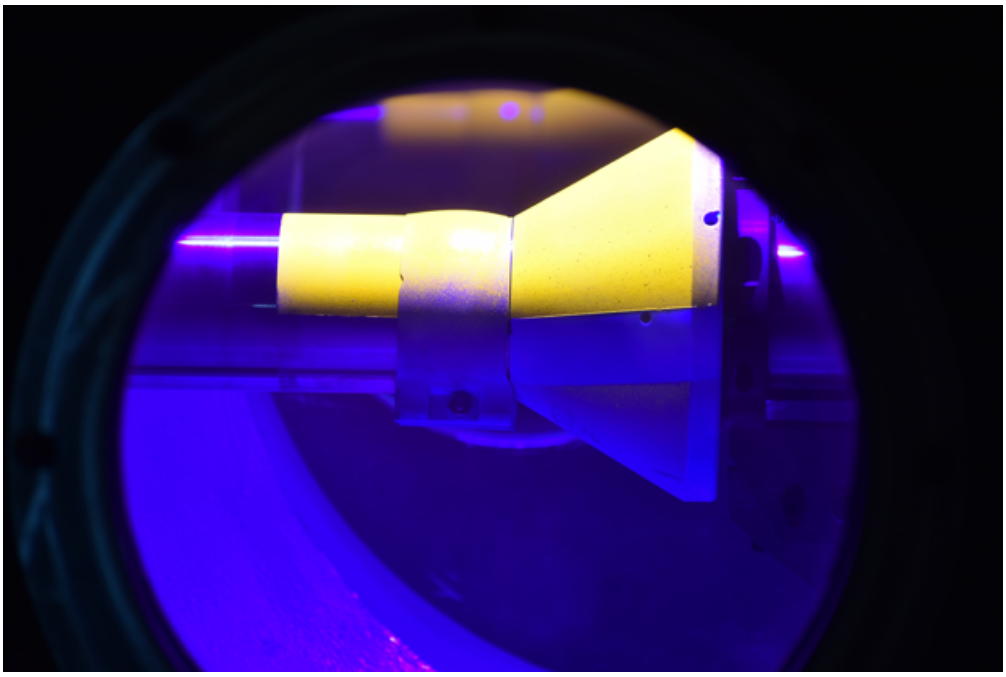
incoming turbulent boundary layer thickness, the amplitude of the deformation was 3 mm (0.118 in), yielding a wavelength of 116 mm (4.56 in).

$$\frac{2a}{\lambda} = 0.053 \tag{3.4}$$

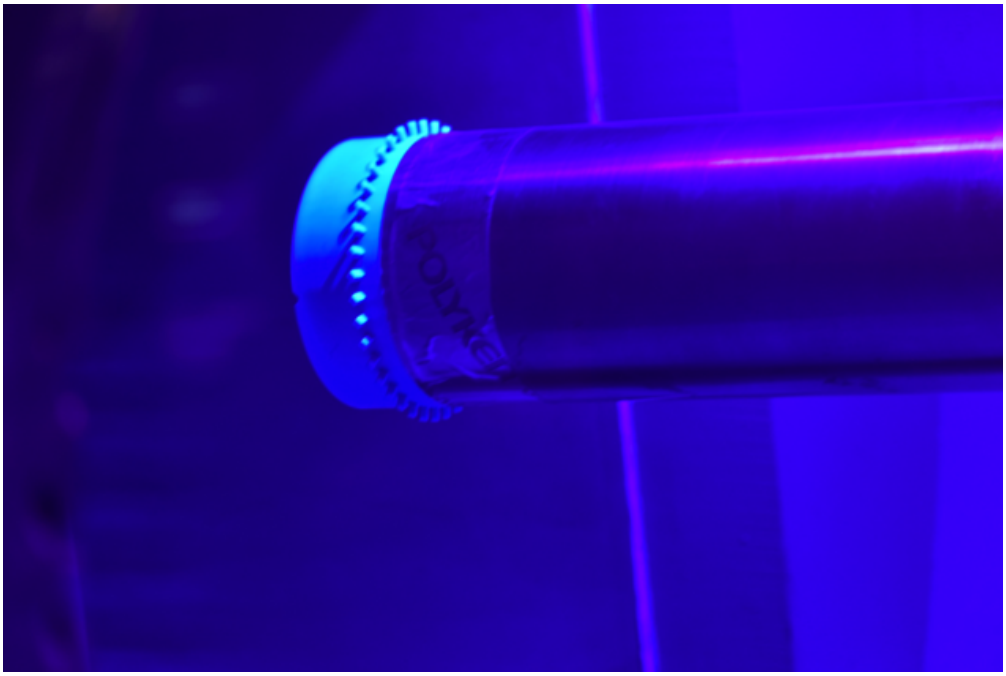
To adjust the position of the shock-shock interaction, the deformation was a 3-D printed sleeve that could be moved along the cylinder to locations that impinged shocks at predicted locations. To predict shock impingement locations, the shock angles from the prior Mach 4 effort were used to find an effective turning angle of the deformation and using that effective turning angle, combined with Mach 7, gave a predicted wave angle using the conical shock relations.

Diagnostic Techniques

The diagnostics used in these experiments were high speed schlieren and temperature sensitive paint (TSP) that were acquired simultaneously at 20 kHz. Figure 3.21 shows a top down schematic of the schlieren setup, with the system imaging through the side of the test section, allowing for TSP imaging from the top, taking advantage of the axisymmetric nature of the model. The schlieren system used a Photron SA-Z with a 70-200 mm zoom lens and a 5 μs shutter. The system was evaluated using a 532 nm long pass filter to block the UV light from the TSP LED's; however, this was removed as the LED signal was not detected in the camera image and the filter reduced the intensity of the schlieren signal. The TSP setup used two continuous, water-cooled LED's from Innovative Scientific Solutions (ISSI) that emit 400 nm UV light, a Photron AX-200 with a 50 mm camera lens, with a 535 nm long pass filter attached. The diagnostic paint used was an in-house blend created by Dr. Cary Smith for use in the UTSI facilities [78, 79] and is based on the DLR formula developed by Martinez *et al.* [80].



(a) Hollow cylinder flare with the deformation attached and diagnostic paint applied.



(b) Tripped leading edge of the hollow cylinder.

Figure 3.19: Model used for the duration of the experimental campaign. Note: the deformation was moved between runs.

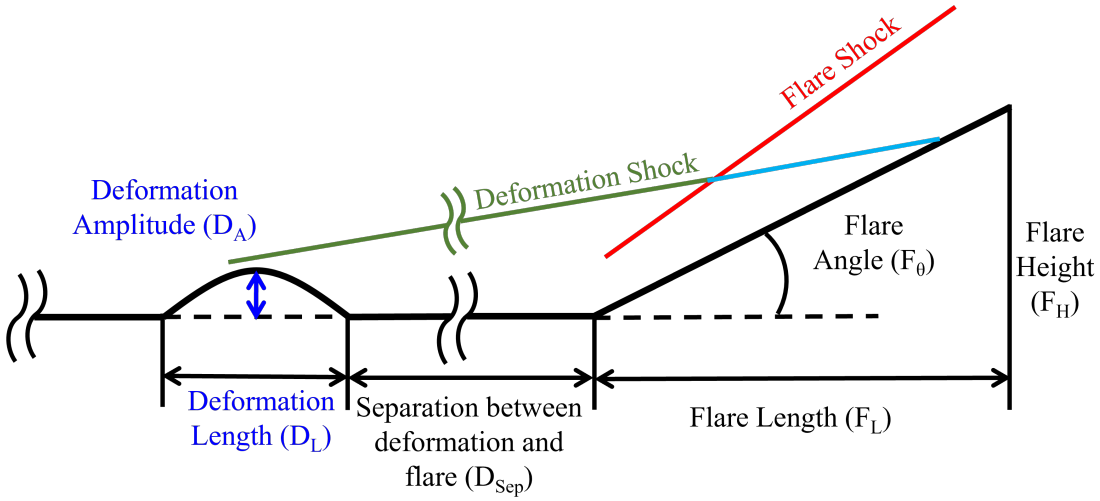


Figure 3.20: Schematic of the planned experiment.

Table 3.3: A summary of the test conditions for these experiments. The list includes the deformation spacing from the flare-cylinder junction (D_{Sep}), measured second wave stagnation pressure (P_0) and stagnation temperature (T_0) along with the unit Reynolds number (Re_x) calculated from isentropic theory

Case #	Baseline	Case 1	Case 2	Case 3	Case 4
D_{Sep} [mm]	N/A	0	30	50	70
P_0 [kPa]	992	958	999	986	1007
T_0 [K]	550	550	550	550	550
Re/x [$\times 10^6$ m^{-1}]	5.00	4.83	5.04	4.97	5.07

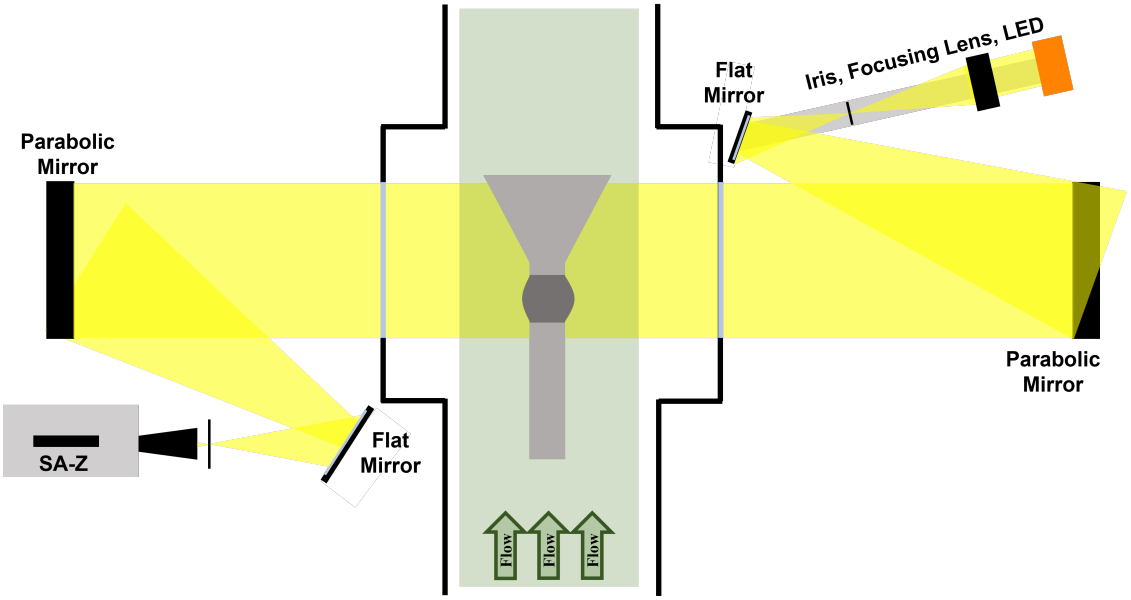


Figure 3.21: Top view schematic of the schlieren system used.

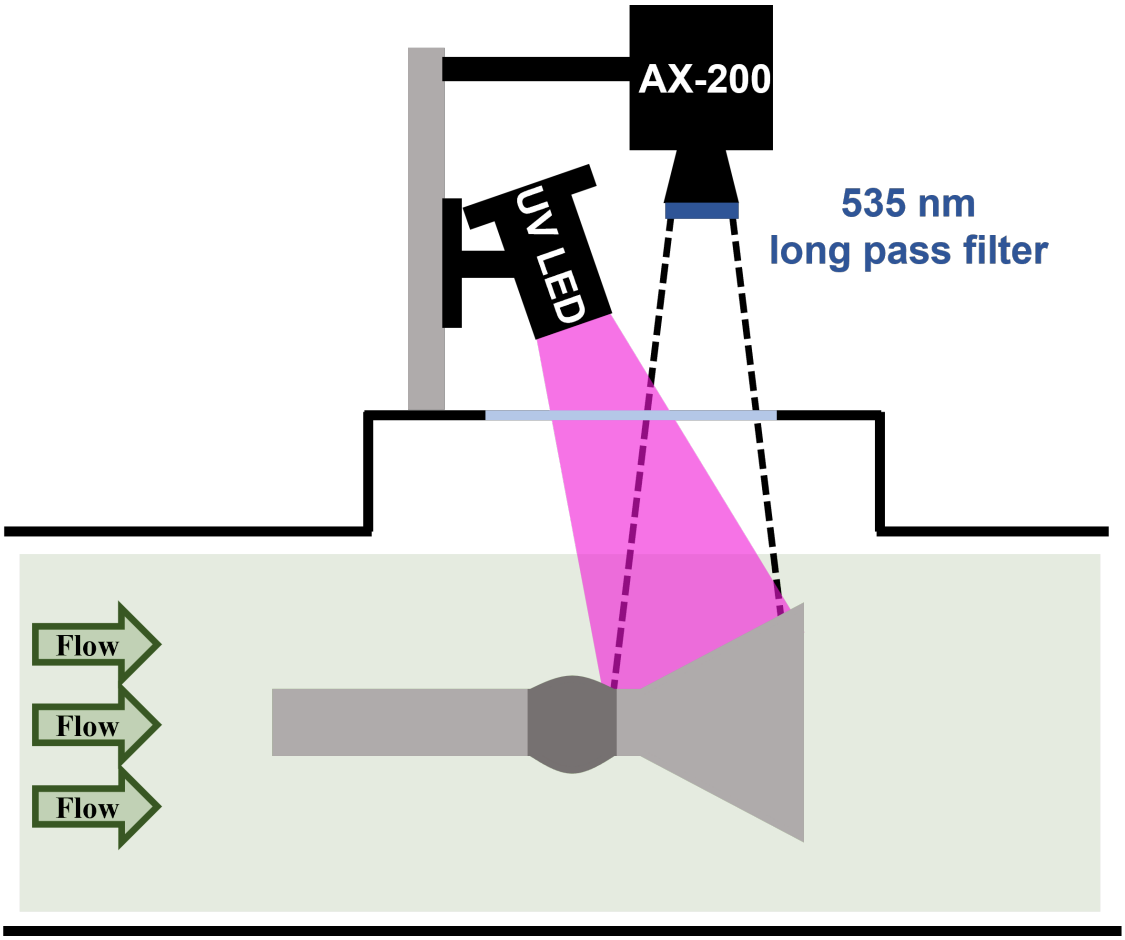


Figure 3.22: Side view schematic of the TSP system used.

3.3.2 Results and Discussion

Baseline

An undeformed case was first run to characterize the base flow field for this model. Figure 3.23 shows a time averaged schlieren image of the flare generated shock boundary layer interaction (SBLI) with the flare shockwave highlighted in red. While not shown in this image, the markers for the deformation shock and its projected impingement on the flare are also defined in the image. Due to the low-density environment of the facility, the schlieren images were background subtracted using schlieren images taken at vacuum just prior to the run and to keep a consistent colormap between deformation cases, every average schlieren image was normalized by the maximum intensity found in the interaction.

The coordinate system used places the origin of the model at the flare-cylinder junction and is consistent throughout all measurements and figures. Above the Origin point, the flare shock is nearly parallel with the cylinder indicating a separation region at the juncture of the flare, while the shock deflects away from the model between 20 and 40 mm in the streamwise direction. At this inflection point, the shock compresses close to the flare, indicating boundary layer reattachment. This is further supported by the modified Stanton number surface mapping in Fig. 3.24. Between the aforementioned streamwise locations there is a spike in heating that corresponds to the boundary layer reattaching.

The modified Stanton number calculations followed the procedure outlined by Liu *et al.* [81] and Nakakita *et al.* [82] where the heat transfer was first calculated using Eq. 3.5, where t_m is the total time for the calculation, t_i and t_{i-1} are the times at two consecutive frames, and T_i and T_{i-1} are the temperatures at those corresponding frames.

$$q(t) = 2\sqrt{\frac{\rho c k}{\pi}} \sum_{i=1}^{m} \frac{T_i - T_{i-1}}{(t_m - t_i)^{1/2} + (t_m - t_{i-1})^{1/2}} \tag{3.5}$$

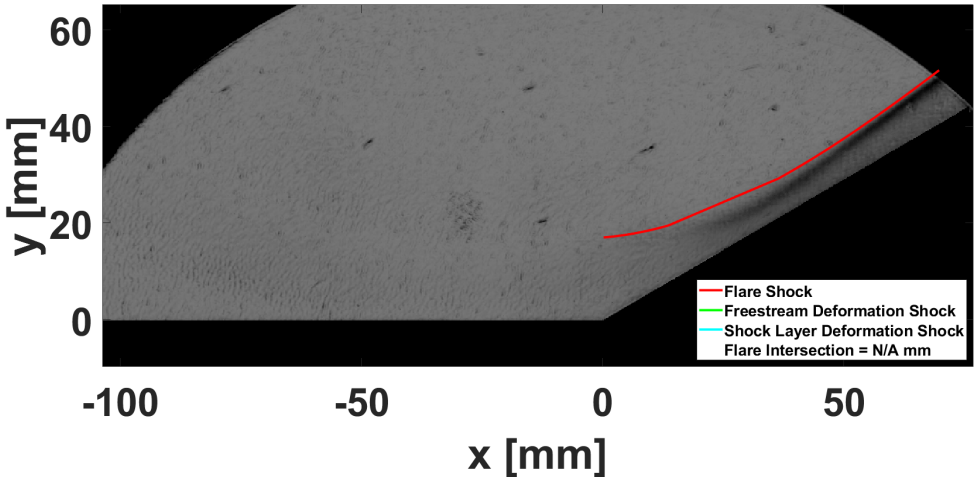


Figure 3.23: Time averaged schlieren image of the undeformed hollow cylinder flare.

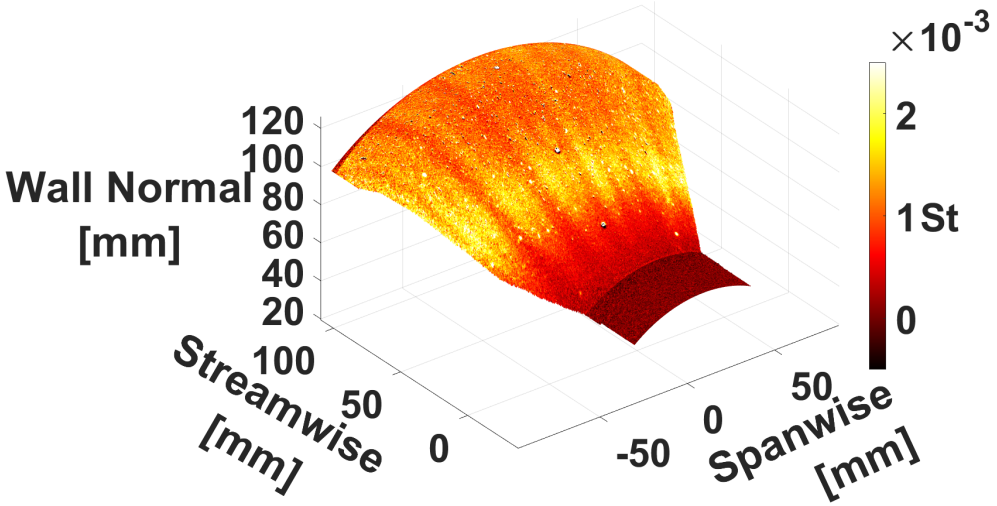


Figure 3.24: Surface map of the modified Stanton number

To simplify the calculations, two frames were used to make the calculations. The first frame, T_{i-1}, was a time average of twenty-one frames at the beginning of the second wave passage, and the second frame was the same length time average at the end of the second wave passage. The average time for the first frame, t_{i-1}, calculated using the average frame number divided by the camera sampling frequency. Since the camera was triggered along with the tunnel pressure data, the temporal location within the wave passage was verified. The is a material constant prior to the summation in Eq. 3.5 was calculated for this TSP formulation and application by Smith [78] from benchtop characterization as 688 $J/(m^2 \cdot K \cdot s^{1/2})$.

Using the heat transfer from Eq. 3.5, the modified Stanton number was calculated using Eq. 3.6. The values for c_p, ρ_e, u_e, and T_0 were taken from the isentropic relations for the Mach 7 Ludwieg tube and Taylor Maccoll solution for a 28° cone as the flare while T_w and $q(t)$ were measured by the TSP. This modified Stanton number varies from the traditional Stanton number by using the stagnation temperature instead of the adiabatic wall temperature as the stagnation temperature is easier to measure than the accurate calculation of the adiabatic wall temperature.

$$St = \frac{q(t)}{c_p \rho_e u_e (T_0 - T_w)} \tag{3.6}$$

Fig. 3.24 also highlights the reattachment vortices that vary spanwise across the flare as hot and cool streaks. These vortices are a known feature in interactions like these and have been seen in the UTSI Mach 4 on the same model with a naturally developing turbulent boundary layer [83]. This, along with the spacing between streaks not matching in distance or spatial frequency with the trips indicates that the vortices are a feature of the flare interaction and not remnants of the leading-edge trips.

To better visualize the streamwise heating variations along the flare, slices were taken along lines of constant radial angles, ϕ and lines of constant streamwise positions, x. To do this the image must be transformed from Cartesian coordinates to cylindrical coordinates through the use of a transformation matrix. A 2-D example of how this process works is highlighted in Fig. 3.25, where the top image is the Cartesian Stanton number mapping, the central image a representative transformation matrix, and the lower image the cylindrical

coordinate output, where ϕ is the flare angle from centerline parallel to the streamwise direction. Once there was little in the way of heat transfer along the cylinder portion of the model, only the flare was mapped to cylindrical coordinates.

With the data transformed, linear profiles were taken at multiple locations in both streamwise and angular positions. Figure 3.26 shows St profiles along lines of constant streamwise positions. Figure 3.26a, and lines of constant radial angle. Figure 3.26b. Both figures indicated increased heating along the edge of the flare; however, these increases were artificial and were caused by the curvature of the flare. The ratiometric nature of TSP processing can account for most model curvature; however, the lowered signal intensity due to heating and the oblique angle between the camera and edges of the flare threw off the values near the edges. To compensate for this signal noise, the analysis for the deformed cases was concentrated along the centerline of the model. In Fig. 3.26a, the vortical streaks are clearly defined as peaks and troughs moving along the ϕ direction while the various points in the streamwise direction show increased heating at the reattachment and a decrease afterwards. This is more clearly seen in the continuous streamwise profiles Fig. 3.26b. In both cases, the profiles were made fitting a smoothing spline to the data in MATLAB's native fit function. This helped to eliminate outliers visible as speckles in Fig. 3.24 and Fig. 3.25 and make the graphs more legible with clean curves as opposed to data points.

To provide a clearer representation of the heating profile along the flare. Figure 3.27 is the centerline streamwise St profile from Fig. 3.26b, where $\phi = 0$. The low St value corresponds the heating within the separation bubble at the base of the flare and the peak heating at 40 mm is the boundary layer reattachment on the flare. The region between 20 and 40 mm shows a rapid rise in heating that corresponds to the compression of the flare shock towards the surface seen in Fig. 3.23. The small spike in heating at 105 mm is an artificial increase as that point is where the flare flattens out. This point on the flare is identifiable in Fig. 3.19a.

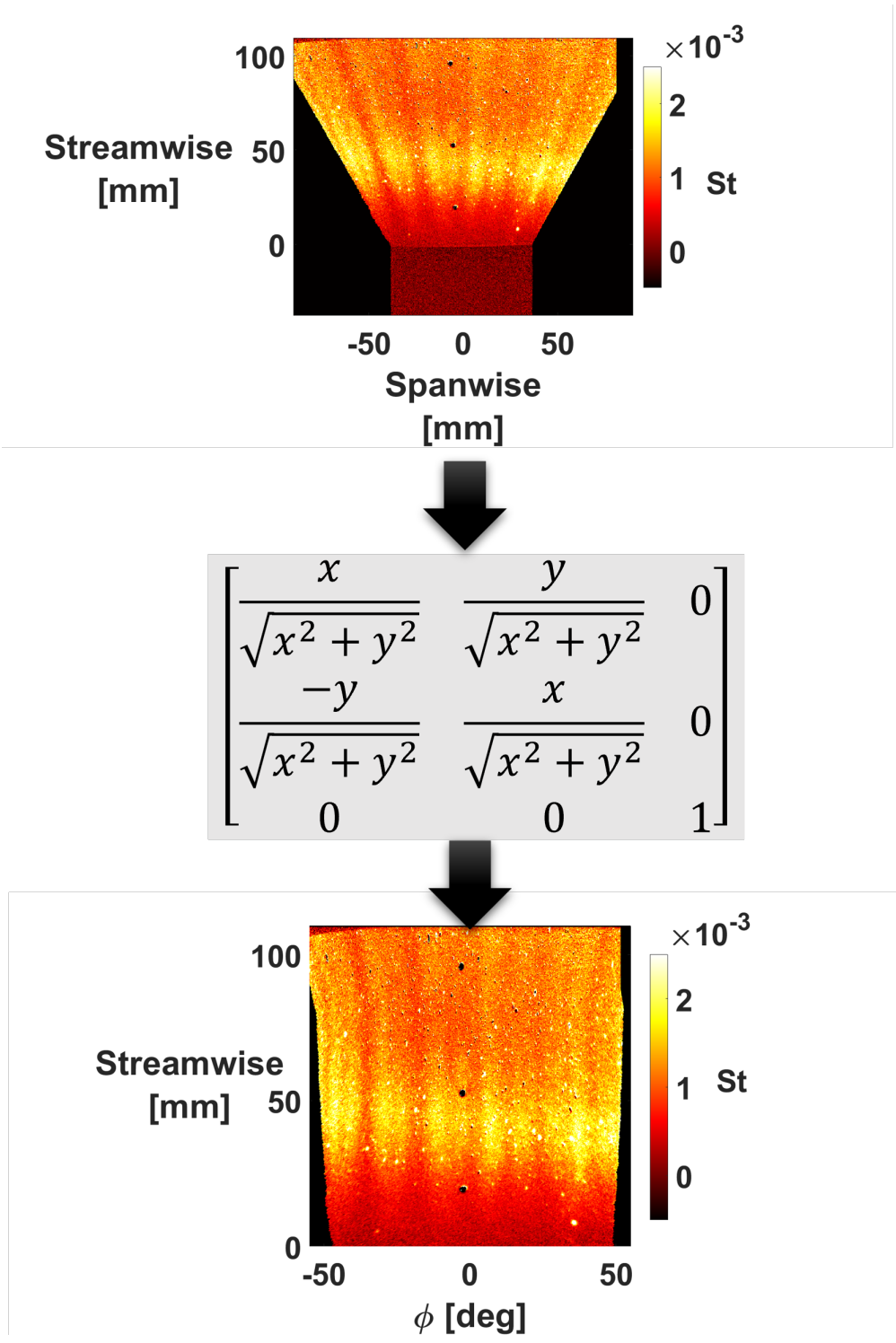
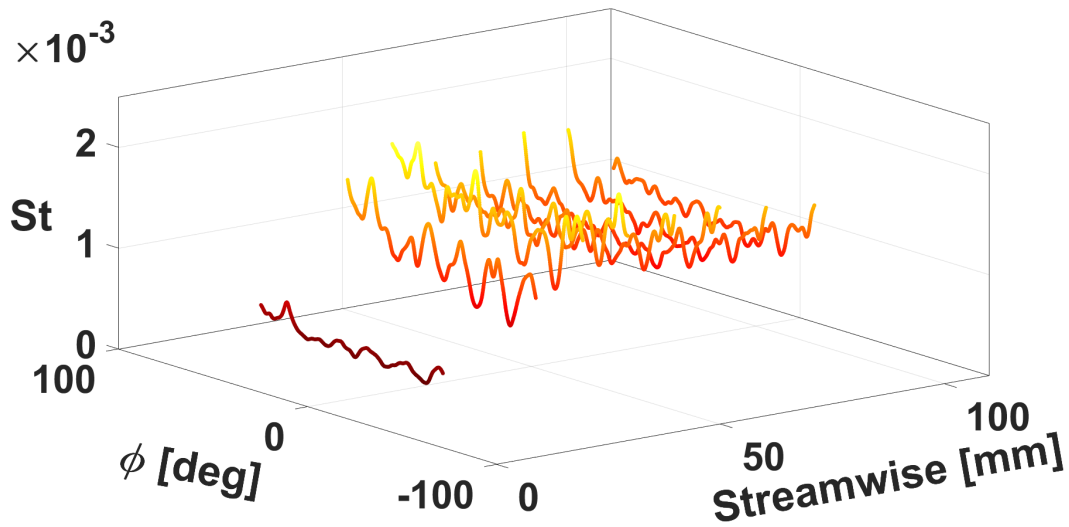
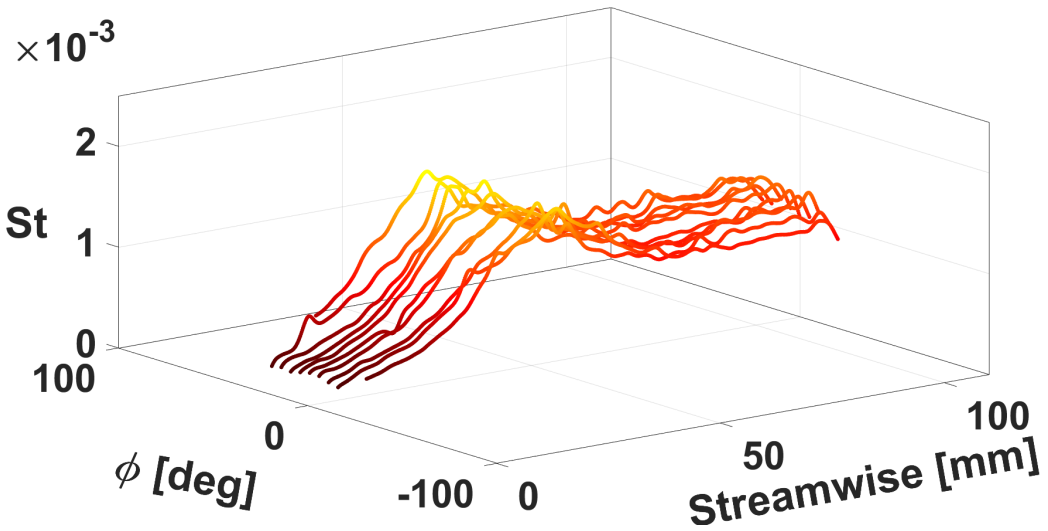


Figure 3.25: Cartesian to cylindrical coordinate transformation.



(a) Lines of constant x



(b) Lines of constant ϕ

Figure 3.26: Linear C_h profiles along the baseline flare configuration

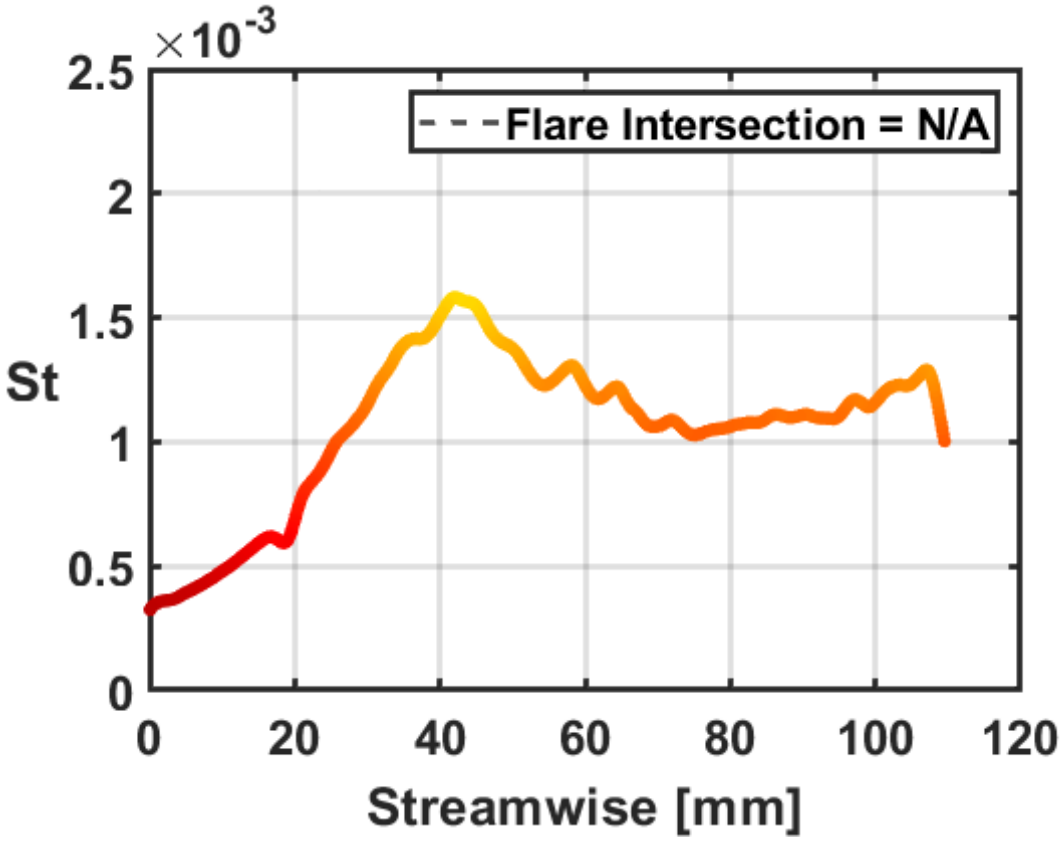


Figure 3.27: C_h profile along the centerline of the flare

Case 1 & 2

The first case was placed the deformation at the base of the flare with no flat cylinder between them. Figure 3.28 shows the average schlieren image from this configuration, with the deformation shock highlighted in green and the predicted deformation shock in the shock layer highlighted in blue. The predicted shock was calculated by accounting for the change in conical wave angle after the flare shock due to the reduction in Mach number. The freestream deformation shock was 11° at Mach 7.2. With a flare shock angle of 34°, the post shock Mach number was roughly 3, creating a new deformation wave angle of 21°. This blue line accounts for the change instead of assuming that the shock will continue along its freestream path.

Fig. 3.28 shows the deformation shock intersecting the flare shock over the separation region, making the prediction of the new shock angle difficult as the new angle would take the deformation shock back into the freestream before meeting the post reattachment flare shock. Accounting for these changes; however, was deemed unimportant as Fig. 3.29 shows the heating along the flare, with an overall lower St for this case but no substantial differences in the heating profile along the length of the flare.

A better visualization of the streamwise heating profile is given in Fig. 3.30, showing the overall heating is similar in magnitude for this case compared to the baseline case. The reattachment point appears to have shifted downstream slightly, as the peak heating occurs around 45 mm instead of 40 mm like the baseline case. In the separation region, there was an increased heating rate at around 10 mm in the streamwise direction. This suggests that, for this case, the impact of the deformation at the junction does not occur at the predicted flare intersection point, but instead at the point where the shock first intersects the separated region in Fig. 3.28.

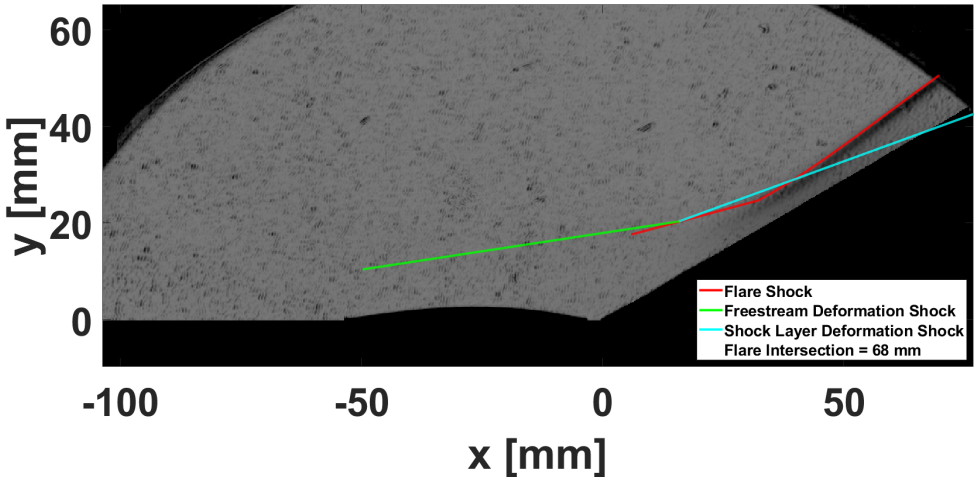


Figure 3.28: Time averaged schlieren image of the 00 mm deformation.

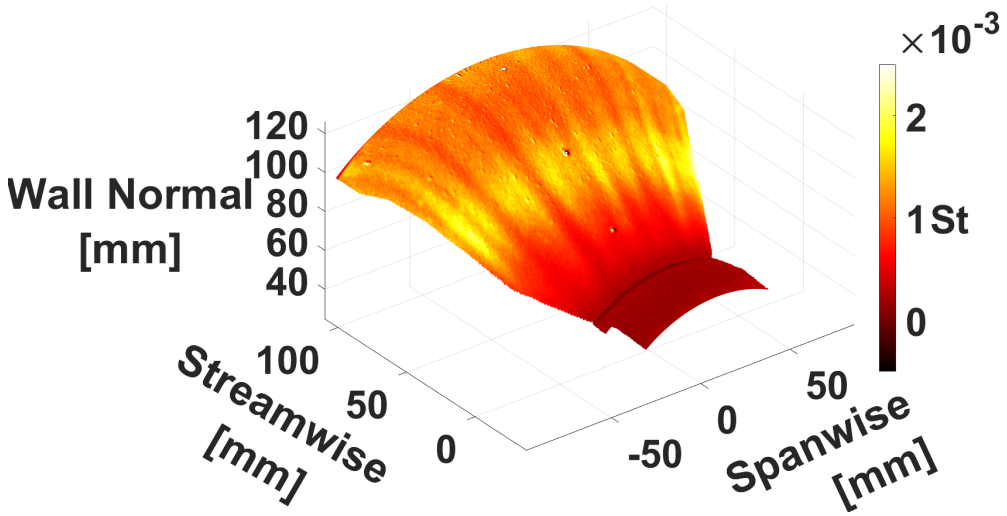


Figure 3.29: Surface map of the modified Stanton number for the 00 mm case.

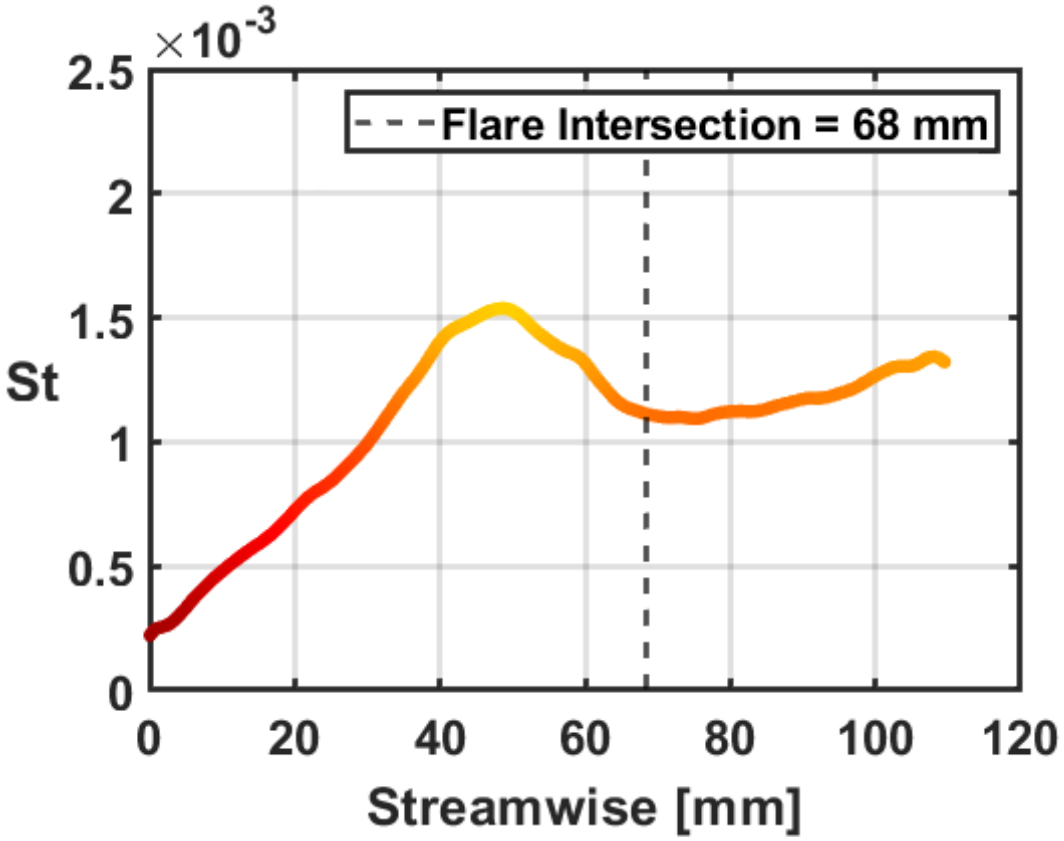


Figure 3.30: C_h profile along the centerline of the 00 mm deformation case

Case 2 placed the deformed panel 30 mm from the base of the flare, shown in Fig. 3.31. Here, the deformation leading edge is out of the SLBI separation region, and the trailing edge forms the outermost boundary. The freestream deformation shock meets the flare shock at 49 mm in the streamwise direction from the flare junction. The projected shock path within the shock layer predicts the deformation shock will impinge on the flare at 79 mm. The flare shock itself does not compress onto the flare to the degree it did in the prior two cases, with the shock appearing straight further upstream along the flare.

The full St map in Fig. 3.32 shows increased heating further along the flare, with the heating remaining high all the way to the flare lip. The impinging shock shows a spreading of heat transfer away from the singular reattachment location over a larger area of the flare. Additionally, the reattachment line has shifted downstream along the flare relative to Case 1 and the baseline, indicating a change in the reattachment point.

The streamwise profile bore this out in Fig. 3.33 as the peak heating appeared lower than the baseline case while the heating downstream of the 40 mm reattachment point was increased in relation to that peak value. Figure 3.33 shows a clear shift in the reattachment point for this deformation case, as the peak heating now appears closer to 50 mm. After this point, the heat transfer remains high, not showing a significant drop off until the predicted flare intersection of 79 mm. With the shock-shock interaction occurring over the reattachment point, the effects form it have an out-sized impact on the heating along the flare as it effectively increases the range reattachment heating.

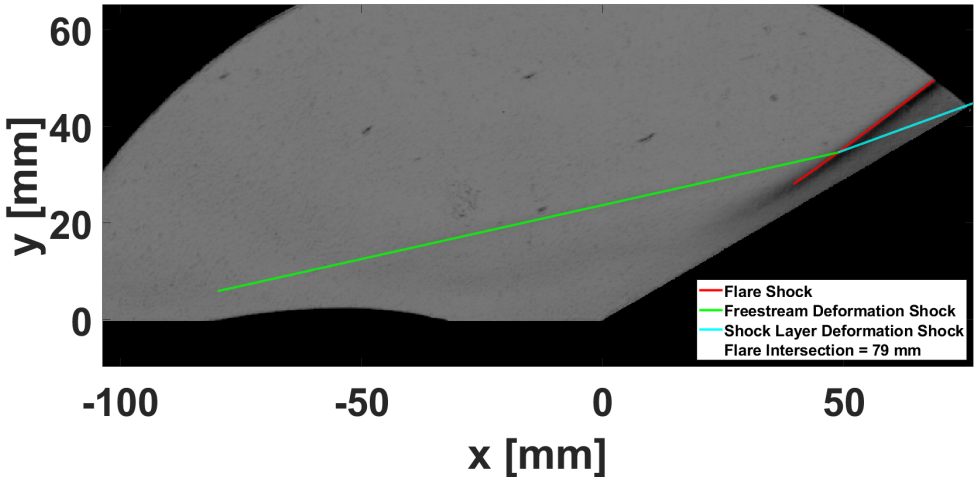


Figure 3.31: Time averaged schlieren image of the 30 mm deformation.

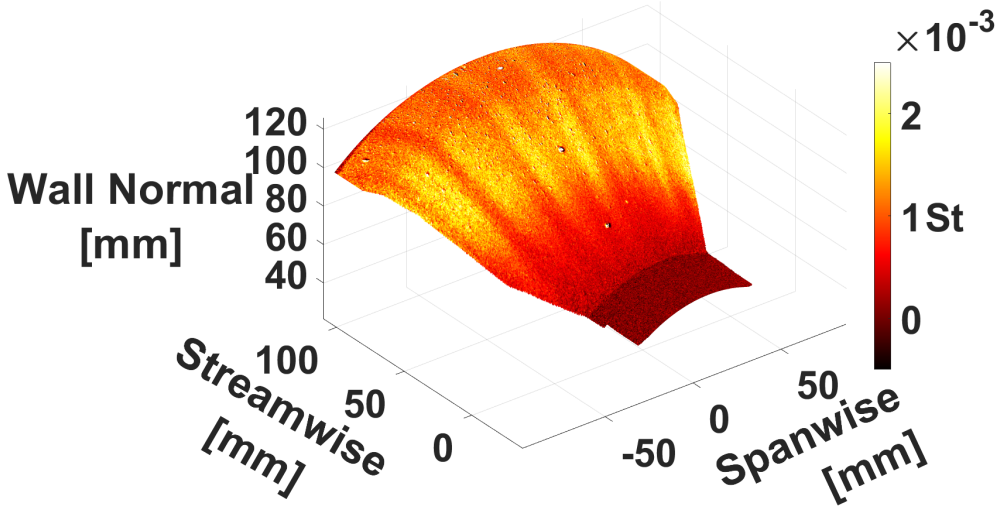


Figure 3.32: Surface map of the modified Stanton number for the 30 mm case.

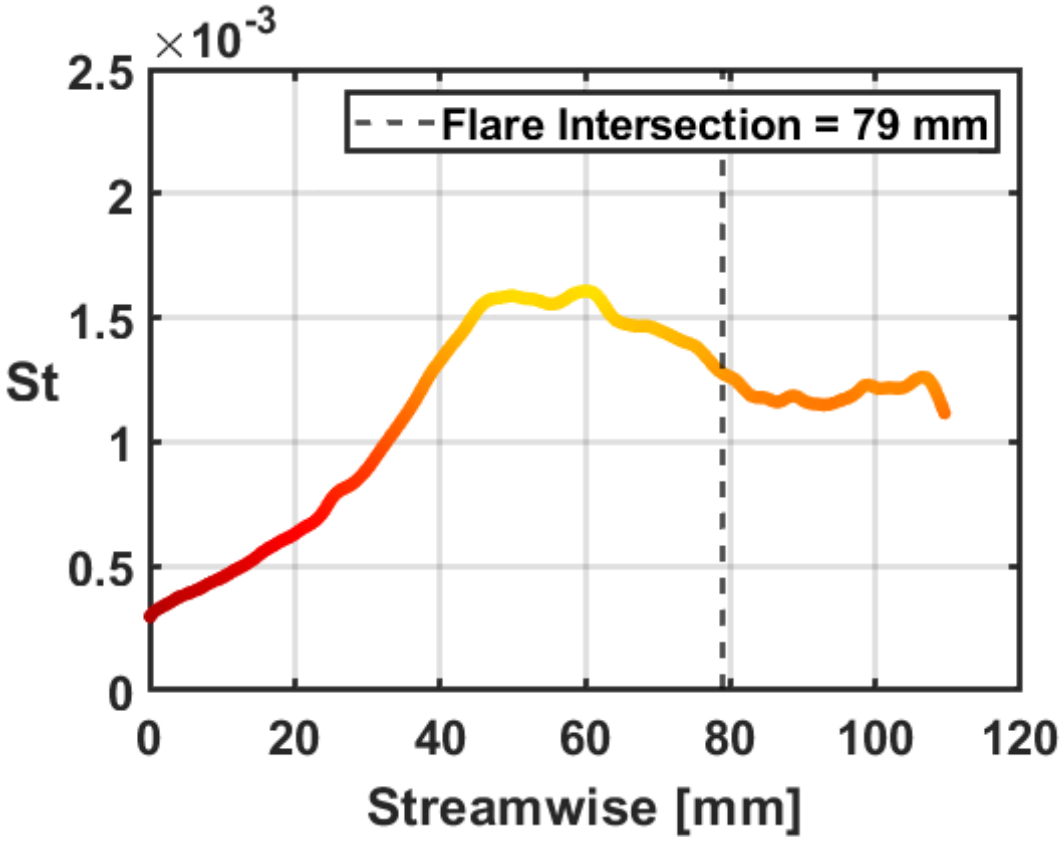


Figure 3.33: C_h profile along the centerline of the 30 mm deformation case

Case 3 & 4

Case 3 placed the deformation trailing edge 50 mm away from the base of the flare, illustrated in Fig. 3.34. Here the shock-shock interaction occurs downstream of the baseline reattachment point at 52 mm downstream, with a predicted flare intersection at 88 mm. This image shows the flare shock compressing closer to the baseline reattachment point more so than the previous case but not the extent of the baseline case.

The *St* map in Fig. 3.35 highlights an increased spread of heat transfer downstream of the reattachment point along with a downstream shift in the reattachment point. The heating, however, did not appear to extend as far in this case as in the prior. Figure 3.36 showed the peak heating shifted downstream, around the same point as the 30 mm case, with the peak being slightly broader and less defined. The heating did not fully relax to the baseline profile but also did not show a broad increase as in Case 2. Instead, the heating slightly relaxed before increasing again to a secondary point at the location of the predicted flare impingement. At the flare intersection point, this distinct heating increase was visible, indicating that the shock layer corrections for the deformation shock were correct. The discrete nature of this heating increase compared to case 2 is most likely a result of the shock impingement not directly interacting with the reattachment point.

Case 4 looked at the deformation 77 mm away from the flare junction. The nominal distance was 80 mm; however the change was made to 77 mm as it was the furthest the deformation could be from the flare while still impinging the shock onto the flare. Figure 3.37 highlights this as the flare impingement was predicted at 105 mm in the streamwise direction meaning the shock impingement would occur at the lip of the flare. The shock-shock interaction occurred at 60 mm from the junction, keeping its effects clear of the reattachment point. The flare shock in Fig. 3.37 showed a more distinct curvature of the flare shock foot and a stronger compression of the shock towards the flare surface prior to the baseline reattachment point.

This relaxation closer to the baseline case was evident in Fig. 3.38, where the reattachment point did not shift as far downstream as the previous two cases. The heating downstream of the reattachment point appeared to relax slightly before increasing steadily

towards the end of the flare, similar to the previous case. These points are clarified in Fig. 3.39, where the peak heating occurs at 45 mm and relaxes until around 80 mm similar to the baseline case. The heating increased steadily from there until the end of the flare. Unfortunately, the localized anomaly in the TSP measurements at the flare lip was not known prior to or during the experiments so it was not accounted for. Even with the localized anomaly, the flare heating increased steadily towards the predicted impingement point at that anomaly, with a broader signature than Case 3.

Comparison of the Results

To make a more concrete comparison between the various deformation cases, the centerline St profiles are plotted against each other in Fig. 3.40. This plot shows the baseline case in black, with its reattachment point at 40 mm in the streamwise direction. Cases 1 and 4 case both showed the slightly shifted peak heating while cases 2 and 3 showed the most extreme peak heating shifts. After the reattachment points, Case 1 mirrored the baseline as its heating relaxed to nearly match the baseline heating. Cases 2-4 all showed elevated heating after their reattachment points, with Case 2 clearly having the most broadband spread in terms of post reattachment point heating, with the St values not relaxing to the baseline values until after 80 mm in the streamwise direction, over 40 mm from the peak heating location. Case 3 case showed a slight relaxation in heating after the reattachment; however, the values were still elevated before they began to increase to the shock impingement. Case 4 showed a similar trend to Case 3, with a longer increase distance between the St trough and the predicted shock impingement.

3.3.3 Summary and Conclusions

Thermal effects from deformation generated shock-shock interactions over a flare at Mach 7 were investigated with the use of simultaneous high-speed TSP and schlieren. The baseline case showed good sensitivity of the TSP to the model configuration, with all the expected flow structures appearing and a lack of leading-edge trip effects persisting in the boundary layer. The conversion of temperature values from the TSP to heat transfer and modified

Stanton number, St, was successful as the reported St values were on the expected order of magnitude. The addition of deformations augmented the heating along the flare surface, with case 2 showing the most change, as its shock-shock interaction was directly over the baseline reattachment point, resulting in a significant spread of the peak heating downstream. Cases 3 and 4 also showed increased heating after their respective reattachment points, with both secondary heating peaks occurring at predicted shock impingement locations that considered the change in conditions in the shock layer. Each deformation case also showed a downstream shift in the reattachment point, with cases 1 and 4 showing a 5 mm shift downstream and cases 2 and 3 showing a shift of 10 mm in the streamwise direction. These promising results will motivate the exploration of more deformation locations along with an increased diagnostic scope to better understand these interactions and the risks they pose to hypersonic flight vehicles.

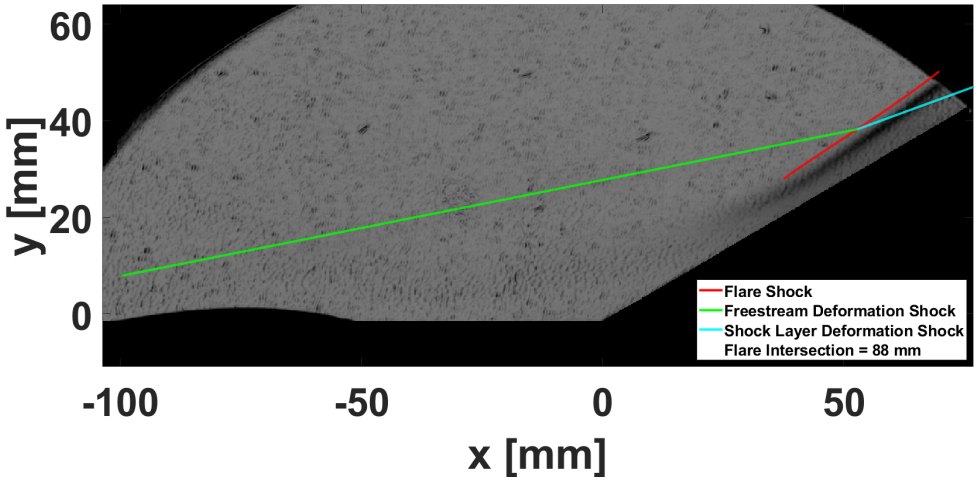


Figure 3.34: Time averaged schlieren image of the 50 mm deformation.

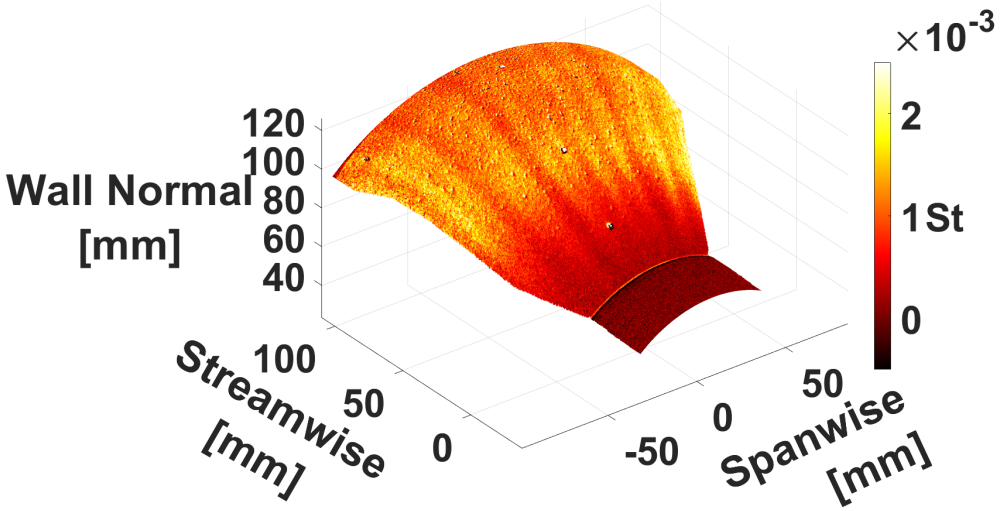


Figure 3.35: Surface map of the modified Stanton number for the 50 mm case.

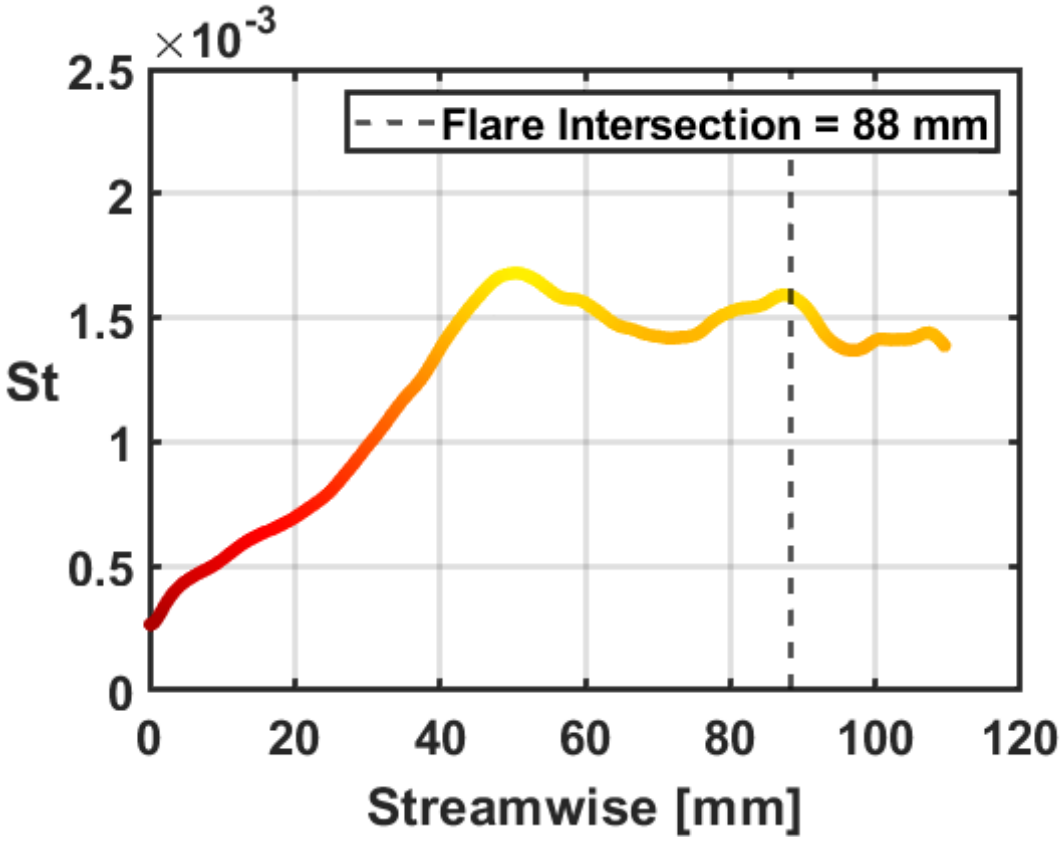


Figure 3.36: C_h profile along the centerline of the 50 mm deformation case

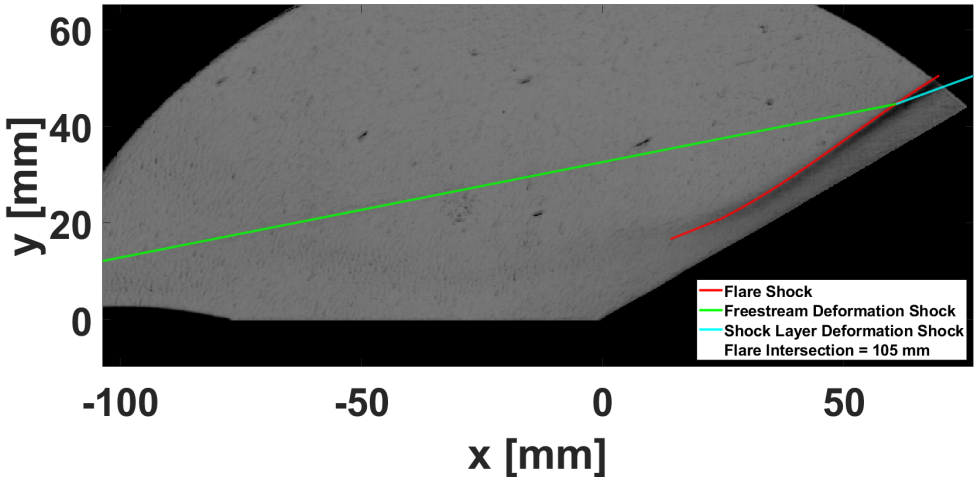


Figure 3.37: Time averaged schlieren image of the 80 mm deformation.

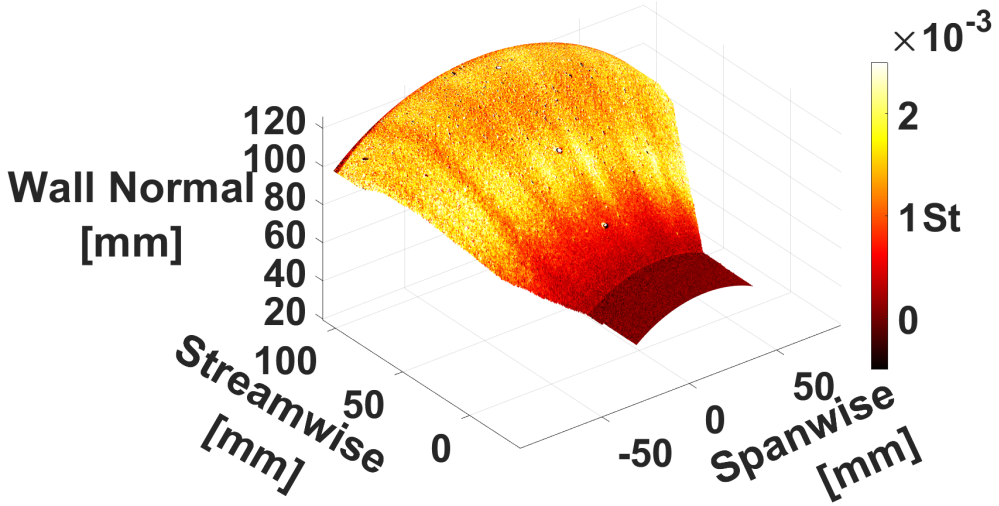


Figure 3.38: Surface map of the modified Stanton number for the 80 mm case.

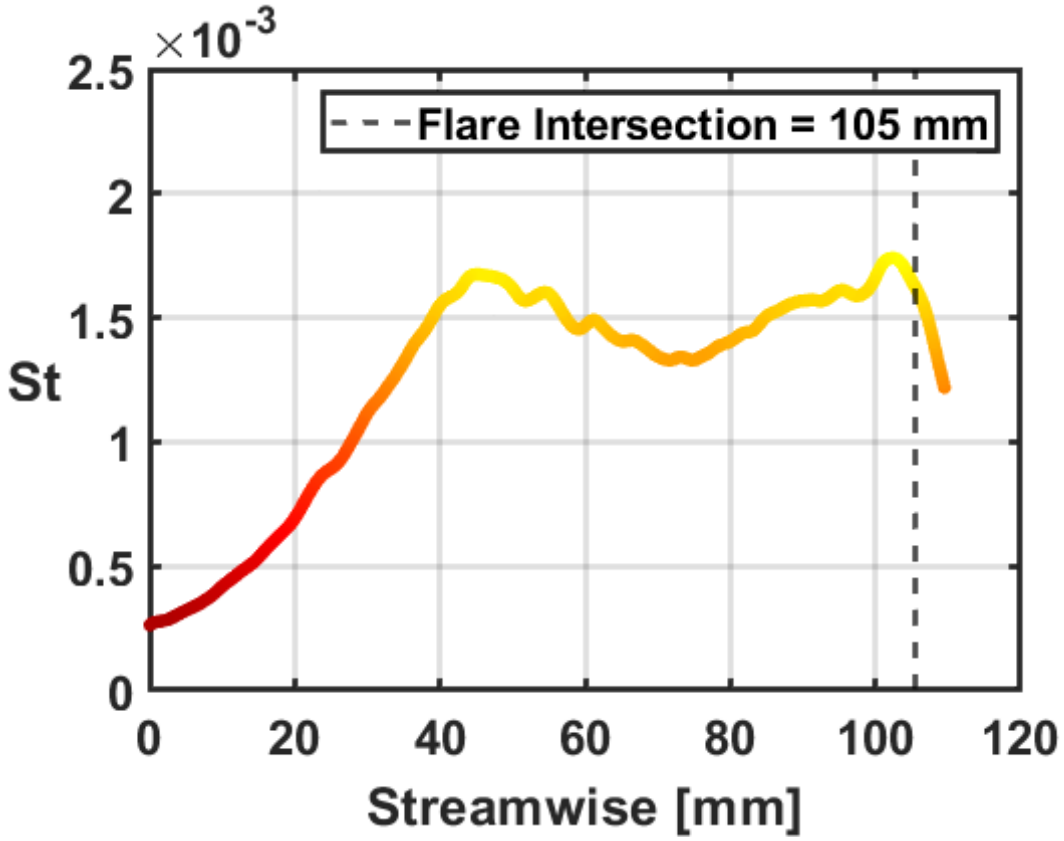


Figure 3.39: C_h profile along the centerline of the 80 mm deformation case

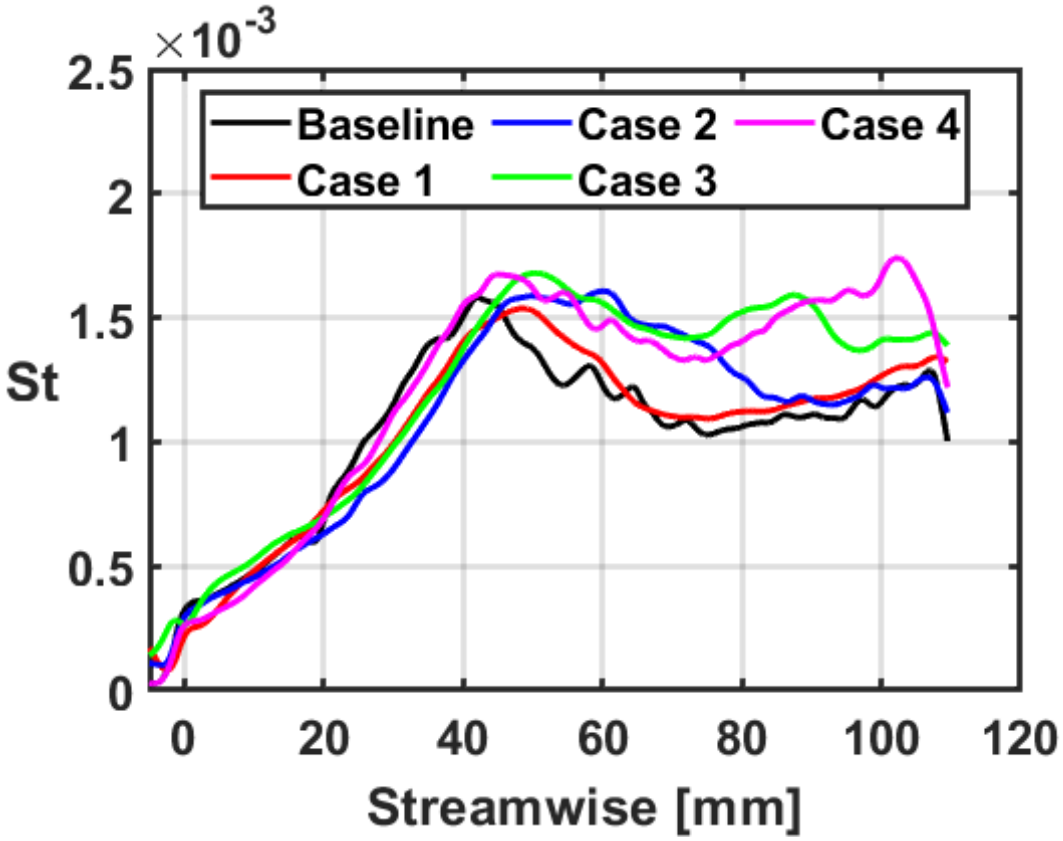


Figure 3.40: Direct comparisons of the C_h profiles for each deformation case

Chapter 4

Diagnostic Development

During the course of research, the limitations of current diagnostics for large scale and impulse facilities were apparent. These difficulties are defined by Eq. 4.1, where I is signal intensity and r is the distance the signal travels. This relationship shows that as distance is increased, the signal intensity drops significantly. This problem magnifies the effect of large facilities as the signal must travel over long distances to reach a sensor or camera, requiring stronger signal to noise ratios and precise alignment.

$$I \propto \frac{1}{r^2} \tag{4.1}$$

While proven measurements like schlieren and diagnostic paint were effective, the implementation of FLDI proved challenging due to the scale of the Mach 4 facility. Outside of the academic setting, these problems are magnified with more large-scale facilities at more extreme conditions. To address the needs of industrial facilities and researchers, new diagnostics need to be tailored to these types of facilities along with developing existing diagnostics and procedures to be more effective in these large-scale facilities. To address this, several offshoot research efforts were conducted to assist AFRL in the development and implementation of these techniques. This section covers the efforts undertaken at UTSI and the Mach 6 High Reynolds Facility to improve laser diagnostics and collaboration between UTSI and AFRL.

4.1 AFRL Mach 6 HRF LISA

The results of this section are pulled directly from the author's journal and conference papers in references [84, 85]. This section outlines the effort to introduce Laser Induced Schliere Anemometry (LISA) into the Mach 6 High Reynolds Number Facility (M6HRF) to characterize the flow quality of this large scale, hypersonic facility, reporting flow velocity, Mach number, and static temperature in a minimally intrusive manner with a high degree of accuracy.

4.1.1 Experimental Setup

Mach 6 High Reynolds Facility

The M6HRF is equipped with various sensors for live measurements of tunnel stagnation and static conditions. The total temperature and pressure is measured in the stilling chamber using a Type J thermocouple and a 20.7 MPa (3000 Psia) Omega transducer. The flow parameters for the two conditions used in this work are provided in Table 4.1.

Laser System

A Spectral Energies QuasiModo pulse burst laser system [86] operating at 10 kHz was utilized to create the laser-induced plasmas in the tunnel. The laser output wavelength was 1064 nm with a nominal pulse width of 10 ns and $1/e^2$ beam diameter of approximately 8 mm. The burst duration was set to 10.5 ms, which gave 105 pulses with an average energy of 1.1 J per pulse. The beam was guided using mirrors to a lens system consisting of a -100 mm (25.4 mm diameter, BK7) and a 150 mm (50.8 mm diameter, BK7) separated by 87 mm. This resulted in the laser beam focusing at approximately 76 cm from the lens, directly at the center of the tunnel.

Schlieren Imaging System

A typical Z-type schlieren system was utilized in the setup to image the convecting localized schliere created by each laser pulse, as shown in Fig. 4.1. The schlieren system used a custom

pulsed LED source [87, 88] that emitted green light, two 40.6 cm parabolic mirrors with focal lengths of $f = 243.8$ cm, and a high-speed camera (Photron FastCam SA-Z) provided 20 kHz images. A bandpass filter centered around 532 nm was put in front of the high-speed camera to eliminate any potential damage from excess laser light and plasma emission.

4.1.2 Results and Discussion

Evaluation of the Optical Setup

In this work, the limited optical access of the facility meant that the laser and schlieren light needed to enter the test-section through the same window. This placed restrictions on the schlieren field-of-view, as the focusing optics for the laser eclipsed the collimated schlieren light. Of more consequence, is the loss of spatial resolution in regard to where the plasma is being generated. Considering Fig. 4.2, if the laser light is perpendicular to the collimated schlieren imaging light, then any displacement in the location of the plasma would be evident in the schlieren images. However, since the collimated schlieren light and laser light enter with parallel optical axes, the motion of the plasma around the focal point is hidden within the path-integration associated with schlieren imaging. Therefore, it is preferable to have the laser be perpendicular to the collimated schlieren light, but this was not possible due to the restricted optical access of this facility.

A major challenge for this application of LISA is the generation of the laser-induced breakdown within the relatively low static pressures during tunnel operation. This is exacerbated by the large stand-off distance from the final lens and the tunnel centerline, which was approximately 76 cm due to the free-jet configuration of the facility. Furthermore, since plasma generation is stochastic in nature, it can happen in proximity to the focus if the Rayleigh range is large, and the path-integration of the schlieren in this setup would not show to what degree this would occur. Therefore, an analysis was done to estimate how likely it was for laser-induced breakdown to occur away from the focal region.

Table 4.1: A summary of test conditions in the Mach 6 High Reynolds Facility. The list includes the freestream Mach number (M_∞), the total pressure (p_0), the total temperature (T_0), the freestream static pressure (p), the freestream static temperature (T), the freestream velocity (U_∞), and the freestream per length Reynolds number (Re/x).

Parameter	Condition 1	Condition 2
M_∞	5.85	5.85
p_0 [MPa]	8.27	12.41
T_0 [K]	565	566
p [kPa]	6.12	9.18
T [K]	71	71
U_∞	996	996
Re/x [$\times 10^6$ m^{-1}]	60.1	90.2

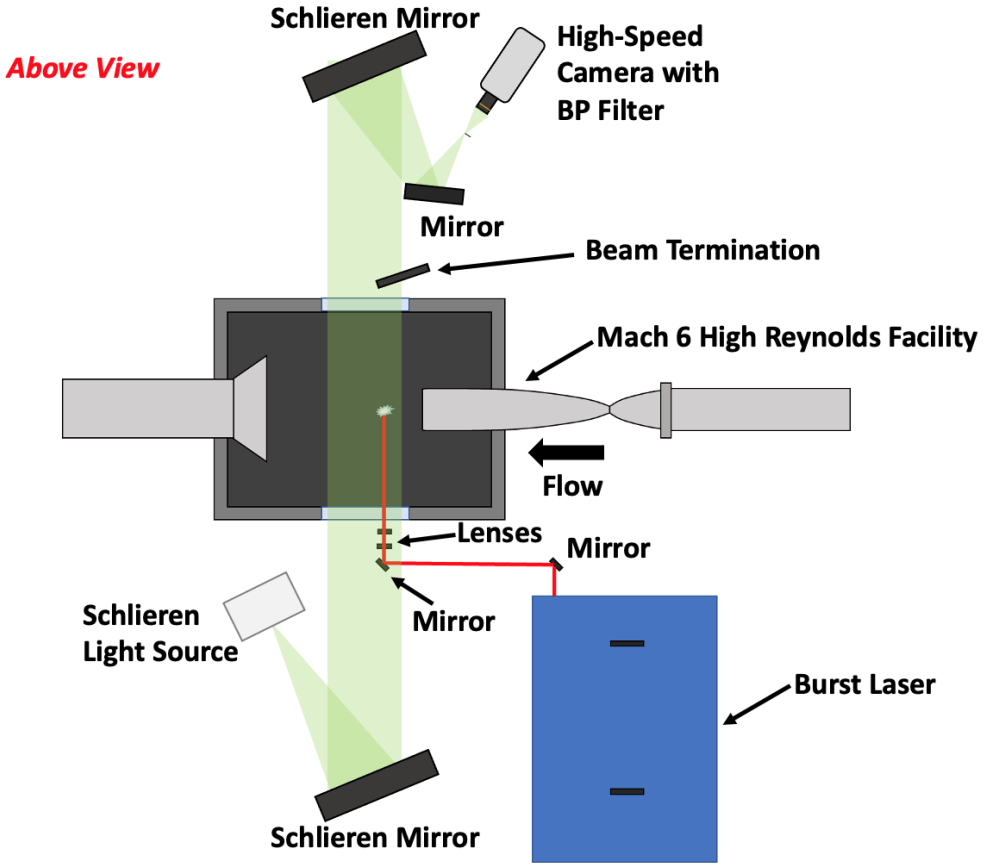


Figure 4.1: A depiction of the experiment setup for LISA in the Mach 6 High Reynolds Facility at Wright-Patterson Air Force Base. The laser operating wavelength was 1064 nm and the schlieren LED source was nominally around 530 nm. A panel placed on the outside of the tunnel was used to terminate the 1064 nm beam after passing through the tunnel.

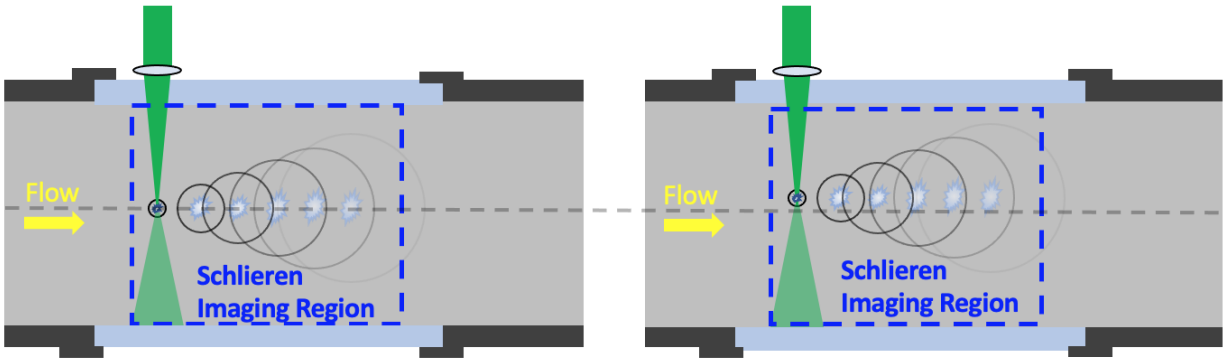


Figure 4.2: An illustration showing how plasma movement is masked in the path-integration of the schlieren. Sensitivity to the motion is lost in the schlieren path-integration for this setup with parallel schlieren light and laser optical axes upon entry into the tunnel.

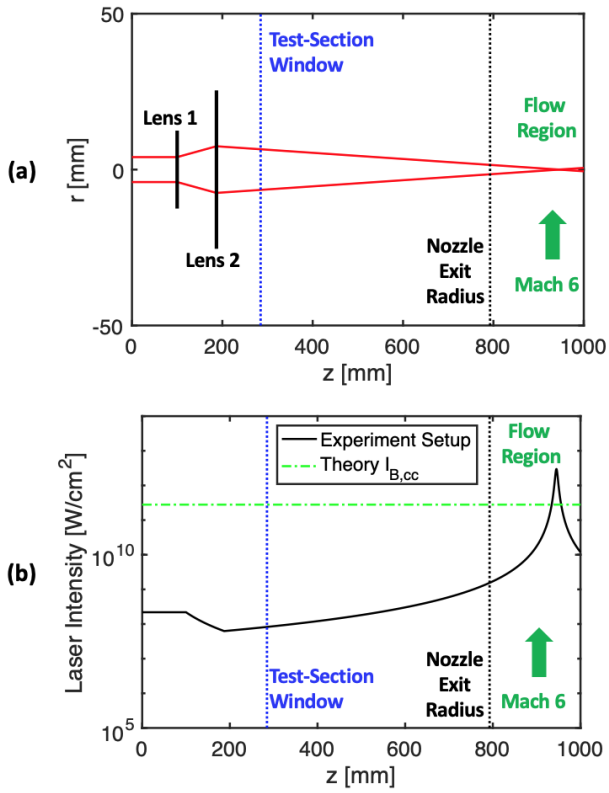


Figure 4.3: (a) Gaussian beam calculation of the laser propagation through the $f = -100$ mm and $f = 150$ mm lenses system. The laser beam was focused to the nozzle centerline. (b) An intensity distribution along the beam path calculated from the Gaussian beam calculations.

For this analysis, the laser beam was assumed to be perfectly Gaussian ($M^2 = 1$) and the propagation of the Gaussian beam through the expansion and focusing lenses was calculated up to just beyond focus. Using the average per pulse energy and the beam waist, an intensity profile along the beam path was calculated. The results are shown in Fig. 4.3. The intensity distribution along the beam path can be compared to the approximate intensity needed to commence laser-induced plasma generation. This intensity was estimated using Eq. 4.2 from the theory of collisional cascade plasma creation in air [89, 90].

$$I_{B,cc} = 1.44 \times 10^6 (p^2 + 2.2 \times 10^5 \lambda^{-2}) [W/cm^2] \tag{4.2}$$

For Eq. 4.2, p is the pressure in atmospheres and λ is the laser wavelength in micrometers. The intensity calculated from this relation is shown in Fig. 4.3(b) as a green line. Based on this analysis, plasma generation is most likely to occur within approximately 1 cm of the focal point for nominal pulse energy. Therefore, the likelihood of creating plasma prior to the focus was considered minimal. Another potential item for consideration is when the plasma reaches a critical density. While the laser pulse is still providing energy, plasma generation can move in the direction of the laser source light [91]. Hence, plasma may still be generated away from the focus in some parts, resulting in an elongated plasma or a string of breakdown plasmas [92], especially with consideration of laser energy fluctuations. Figure 4.4 shows an example of this occurrence, with multiple plasmas appearing as concentric circles in the path-integrated schlieren image.

4.1.3 Velocity Measurements

Examples of the laser-induced schliere written by the 10 kHz pulse train are shown in Fig. 4.5. Each schliere is accompanied by an outward propagating shockwave that also convects with turbulent packet of gas. However, in the reference frame of the schliere, the blast wave is only moving outwards, which causes it to weaken. The motion of each schliere is linear in Fig. 4.5, which supports the assumption that the residual packet of hot, turbulent gas from the laser-induced plasma creation is moving at a constant velocity. This fact is also supported by the measured displacements of schliere shown in Fig. 4.7.

The methodology used to track the schliere is described in Fig. 4.6. The analysis makes use of the dark and bright regions of the schliere associated with the horizontal knife edge for schlieren. The analysis is only sensitive to streamwise motion. The linear curve fits applied to the displacement versus time data in Fig. 4.7 allows the velocity to be extracted from the slope. Tables 4.2 and 4.3 show the obtained values for Condition 1 and Condition 2 respectively. The mean value for Condition 1 was found to be 985.2 ± 12 m/s, which differs from the value of 996 m/s determined by the isentropic relations (see Table 4.1) by about 1%. For condition 2, the mean velocity was determined to be 985.7 ± 14 m/s, which also compares favorably to the value determined from the isentropic relations. Since the two tunnel conditions only differ by total pressure, it is expected that the velocity be identical since only Mach number and total temperature determine the velocity of the freestream.

Mach Number and Static Temperature Measurements

While laser-induced schliere could in principle be written by a means other than laser-induced breakdown plasma creation, this approach does allow for estimation of the mean Mach number in the high-speed flow. As discussed earlier, in the reference frame of the laser-induced schliere, the shockwave from the expansion of the initial plasma propagates outward and decreases in strength. However, in the lab reference frame this wave is also convecting with the flow. Therefore, in the farfield limit the weakened shockwave should act like an acoustic wave and is subject to the Mach cone effect [93, 87]. This effect is observed in Fig. 4.8, which shows the temporal standard deviation of the high-speed schlieren images for each of the conditions. The angle of the Mach cone, μ, is related to the Mach number, M, of the flow by Eq. 4.3.

$$sin(\mu) = 1/M \tag{4.3}$$

The Mach cone angles were determined manually using ImageJ [94] with a line drawn such that it was tangent to two full spherical structures representing the expanding wave. Note that the first wave was not used due to the requirement that the moving blast wave weaken to an acoustic wave in the far field [87]. For Condition 1, the measured angle gave a

Mach number of 5.82 ± 0.17 while a Mach number of 5.76 ± 0.16 was found for Condition 2. Both values agree favorably (within 1.6%) with the value of 5.85 reported in literature for this facility [95, 96, 97].

The total temperature in this facility allows the ideal gas assumptions to hold, and from the definition of the Mach number as the ratio of the local air speed to the local speed of sound, the mean static temperature, T, of the flow can be found from the LISA measurements using Eq. 4.4.

$$T = \frac{U^2}{\gamma R M^2} \tag{4.4}$$

The ideal gas constant, R, for air is 287 J/[kg·K] and the specific heat ratio, γ, is 1.4. Using the previously determined mean values for flow Mach number and velocity, static temperatures for Conditions 1 and 2 were found to be 71.3 ± 3.2 K and 72.9 ± 3.2 K respectively. The mean value for Condition 1 is within 0.5% of the value in Table 4.1, while the mean value determined for Condition 2 is within 2.6% of the value.

4.1.4 Uncertainty Methods

The methods here follow J. R. Taylor's text [98] on error analysis. For the velocity measurements, the primary contributors to error and uncertainty were determined to be the linear regression error, the resolution error, and the statistical error from mean calculation, which are denoted as σ_{Reg}, σ_{Res}, and σ_{Stat} respectively. Hence, using quadrature methods, the error associated with the velocity is given by:

$$\sigma_{Vel} = \sqrt{\sigma_{Reg}^2 + \sigma_{Res}^2 + \sigma_{Stat}^2} \tag{4.5}$$

In each condition, the resolution of the schlieren imaging was 0.239 mm/pixel. Based on the 20 kHz imaging, one pixel uncertainty corresponds to an uncertainty contribution of 4.79 m/s; however, this must be multiplied by $\sqrt{2}$ due to the uncertainty for both positions used in determining the displacement in the velocity calculation. Thus, $\sigma_{Res} = 6.77$ m/s. For σ_{Reg}, the largest value of the error in the slope of the displacement verse time was used when applying Eq. 4.5.

For the Mach number determination, the points corresponding to the intersection of the tangent line with the spherical wave are used. Since the triangle formed by these points gives $\tan(\mu) = \Delta y/\Delta x$, and the small angle approximation for tangent gives $\mu \approx \Delta y/\Delta x$. Thus, the uncertainty relation for the angle is formulated using quadrature methods as:

$$\sigma_\mu = \mu\sqrt{\left(\frac{\sigma_{Res}}{\Delta x}\right)^2 + \left(\frac{\sigma_{Res}}{\Delta y}\right)^2} \tag{4.6}$$

For Eq. 4.6, the σ_{Res} value corresponds to one pixel distance uncertainty with a factor $\sqrt{2}$ being used to account for the displacement calculation. Uncertainty propagation for the static temperature calculation is also treated using quadrature methods. The formulation based on Eq. 4.4 is:

$$\sigma_{Temp} = T\sqrt{2\left(\frac{\sigma_{Vel}}{U}\right)^2 + 2\left(\frac{\sigma_{Mach}}{M}\right)^2} \tag{4.7}$$

4.1.5 Summary and Conclusions

In summary, laser-induced schliere anemometry (LISA) was demonstrated in an axisymmetric free-jet Mach 6 facility. This marked the first application of LISA in a hypersonic facility and the size of the test-section required the laser-induced plasma be created roughly 76 cm from the final focusing lens, which greatly exceeds the distance using in prior work [87]. It is also the first demonstration of the technique in a setup the had the beam enter the test-section with an optical axis parallel to the collimated schlieren light, which could be useful for facilities with limited optical access. As discussed in the text, an issue with such an arrangement is the uncertainty of the written schliere location along the beam axis. An analysis using Gaussian optics was presented here, justifying the choice of focusing optics to minimize the potential of creating plasma away from the focus. The velocity and static temperature measurements in the free stream agreed well with expectations from isentropic compressible flow theory, and the Mach number measured from the Mach cone effect imposed on the convecting blast wave agree with facility expectations. Thus, LISA shows immense potential for characterizing core flow in high-speed facilities.

DISTRIBUTION STATEMENT C. Distribution authorized to U.S. Government agencies and contractors. Other requests refer to AFRL/RQHA, 676 Second St, Arnold AFB, TN.

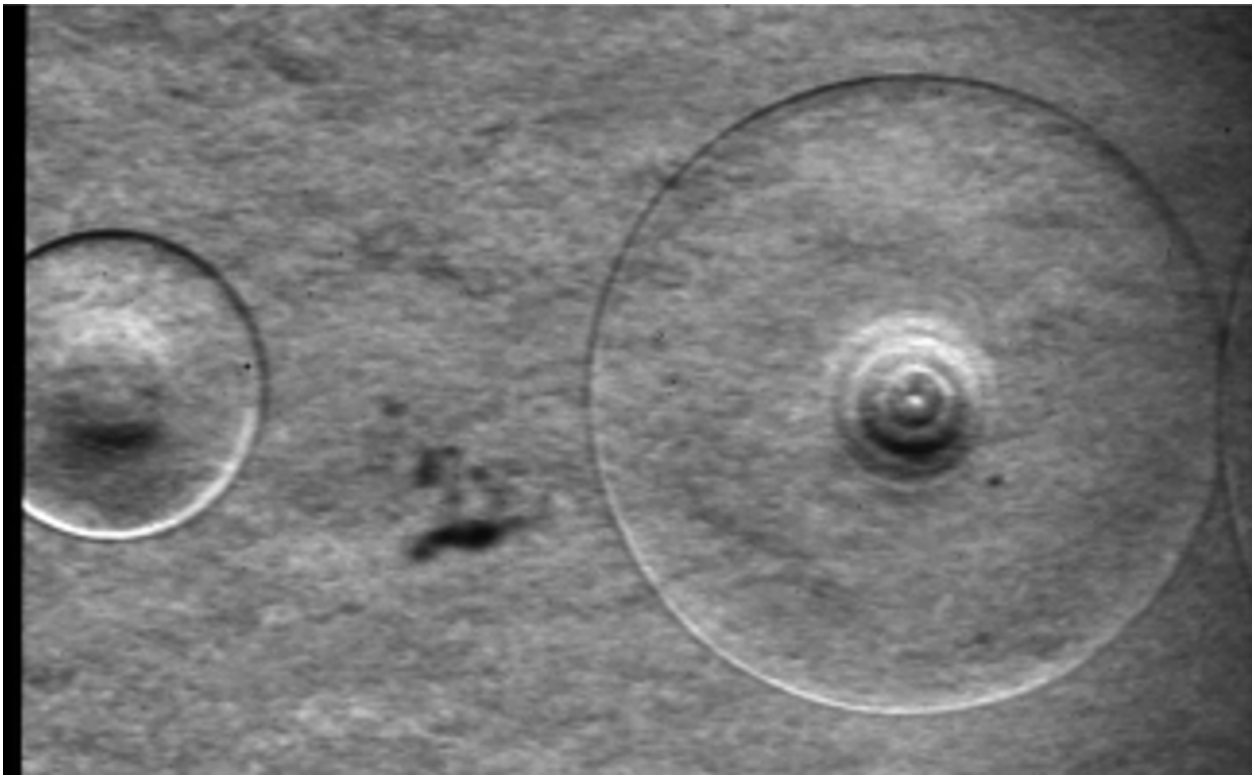


Figure 4.4: A schlieren image showing the effect of multiple laser-induced plasma occurring around the focus. The effect is most noticeable as a series of concentric rings in the schliere. Flow is from left to right.

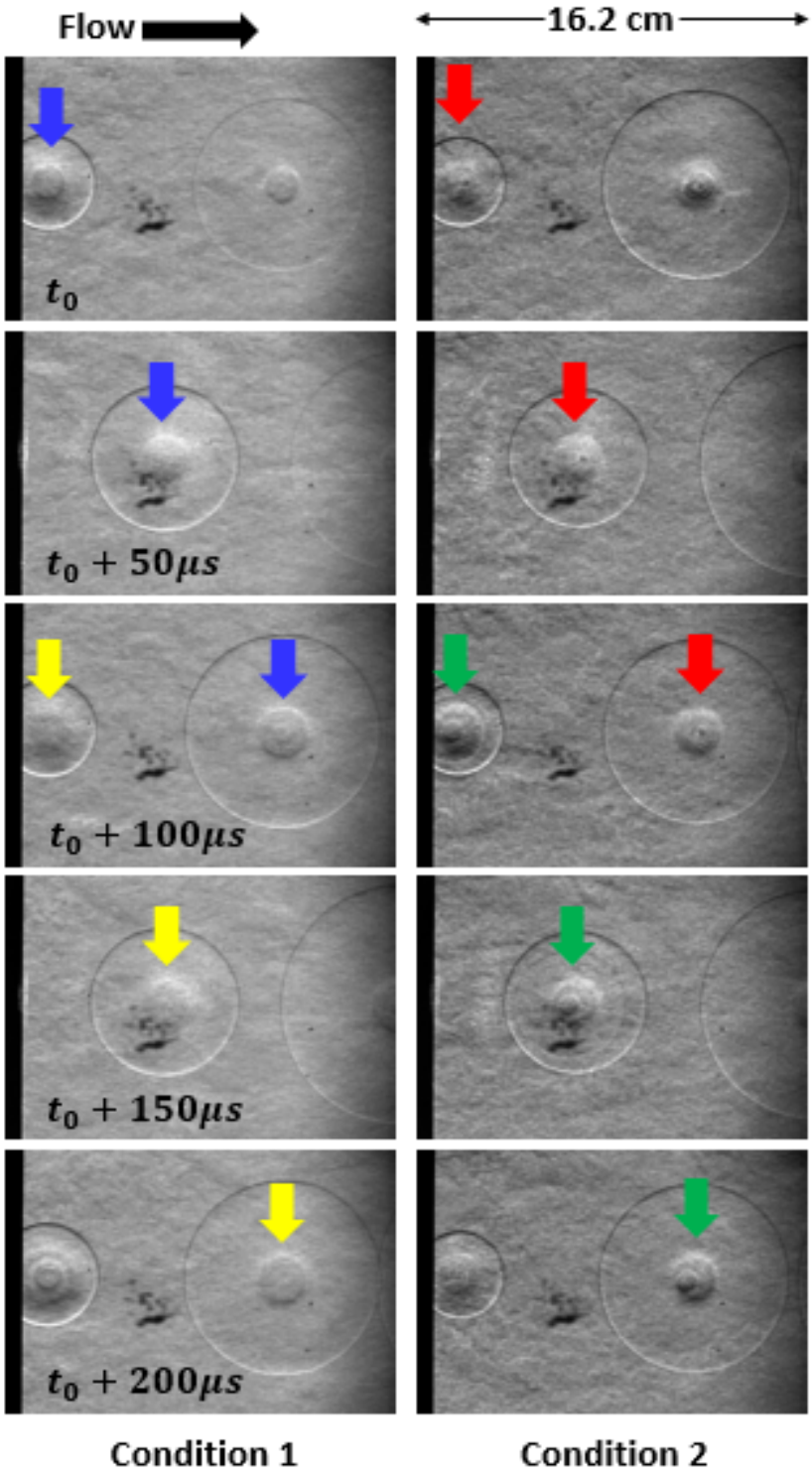


Figure 4.5: 20 kHz schlieren image sequences showing the several schliere written by the 10 kHz burst laser convecting in the Mach 6 flow. The arrows indicate the movement of a schliere and are color-coded uniquely.

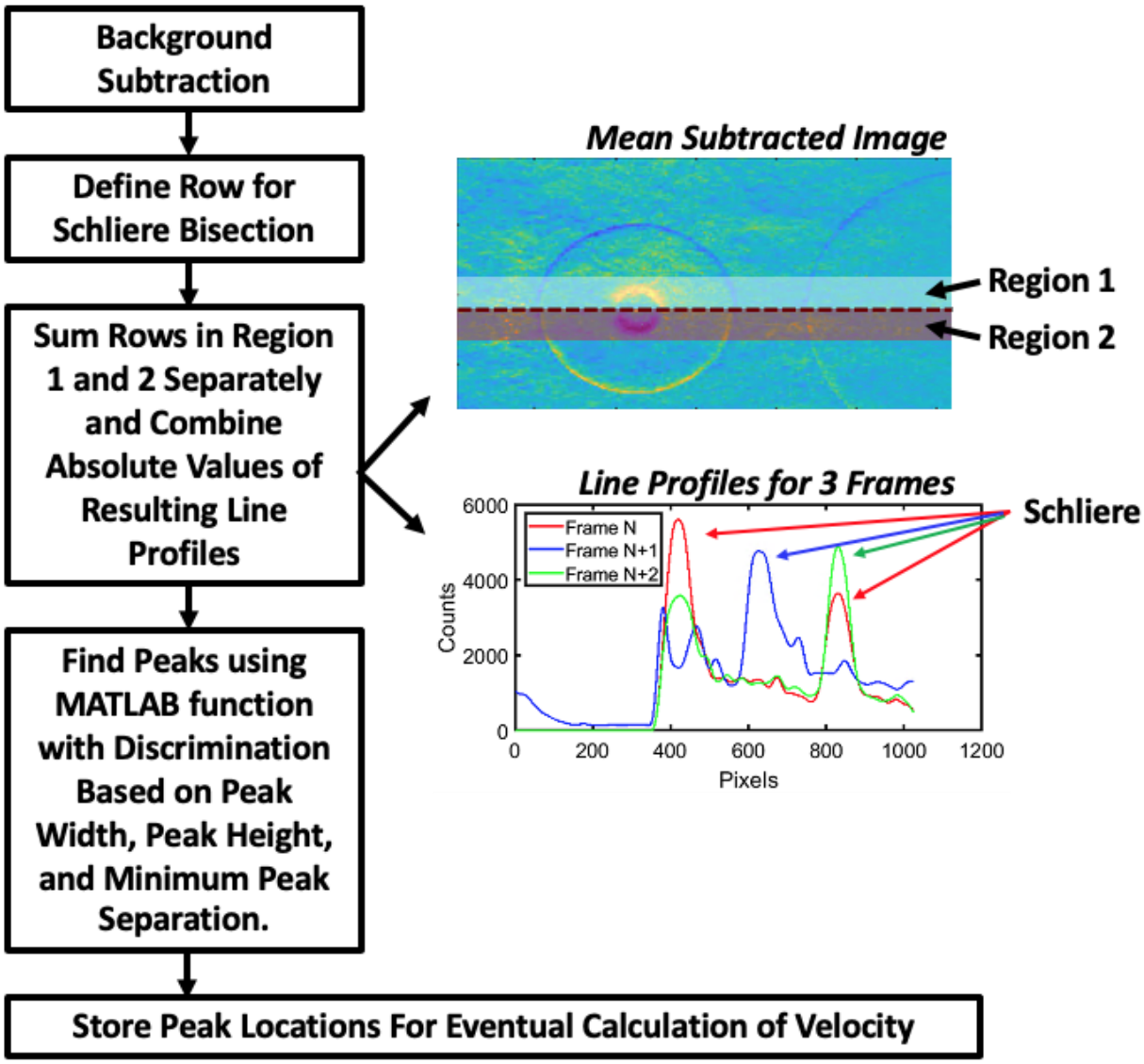


Figure 4.6: A graphical outline of the methodology used to track the schliere.

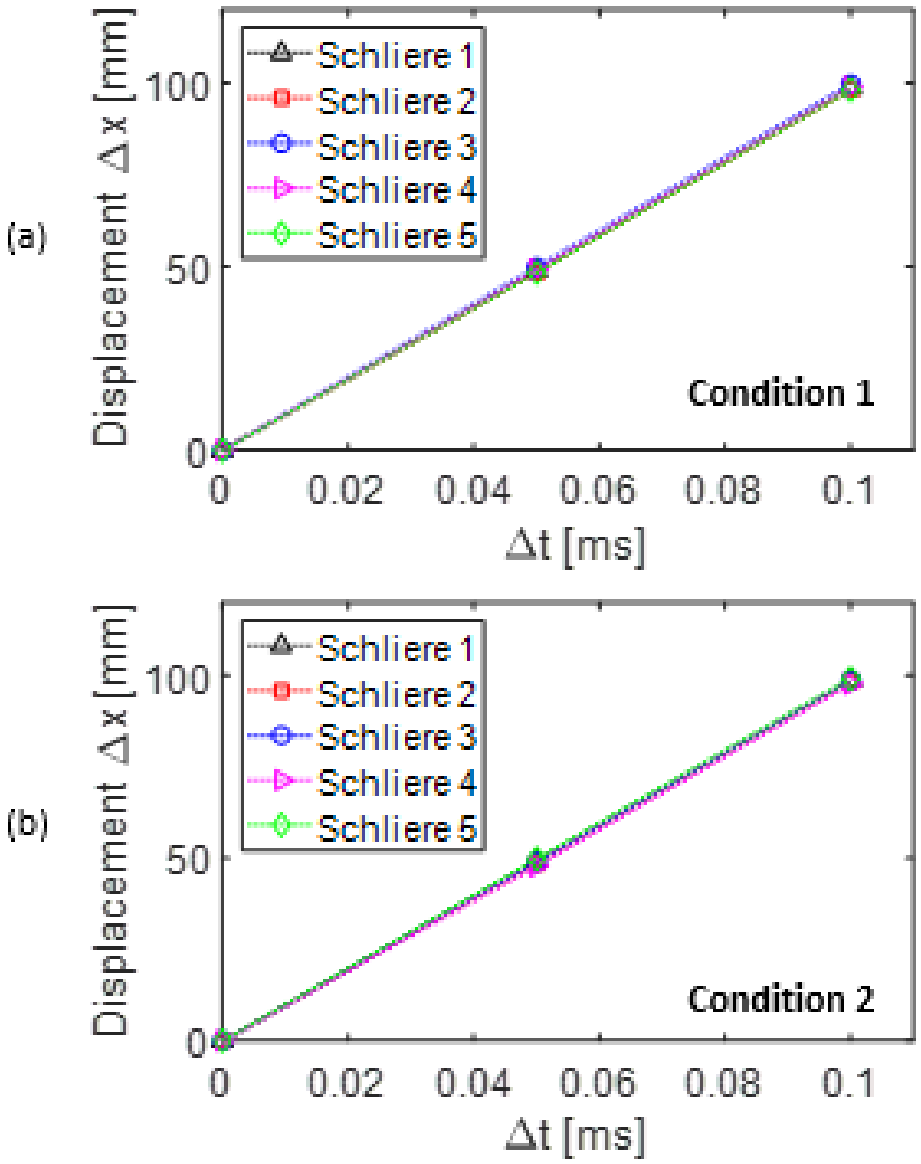


Figure 4.7: Displacement versus time data for (a) Condition 1 and (b) Condition 2. Five schliere were tracked for each and given the limited field-of-view and camera frame rate, only three frames each were appropriate for the analysis.

Table 4.2: Velocities determined from linear fits of data in Fig. 4.7(a).

Tracked Schliere Velocity: Condition 1					
Schliere #	1	2	3	4	5
Velocity $[m/s]$	987.2	984.8	987.2	984.2	982.4
Fit R^2 Value	1.0	1.0	1.0	1.0	1.0
Slope Error [m/s]	5.5	9.7	5.5	1.4	8.3
Mean Velocity $[m/s]$	985.2				
Std. Deviation $[m/s]$	2.0				
Total Uncertainty $[m/s]$	12				

Table 4.3: Velocities determined from linear fits of data in Fig. 4.7(b).

Tracked Schliere Velocity: Condition 2					
Schliere #	1	2	3	4	5
Velocity $[m/s]$	987.2	984.8	987.2	977.2	991.9
Fit R^2 Value	1.0	1.0	1.0	1.0	1.0
Slope Error [m/s]	0.0	9.7	5.5	11.1	2.8
Mean Velocity $[m/s]$	985.7				
Std. Deviation $[m/s]$	5.2				
Total Uncertainty $[m/s]$	14				

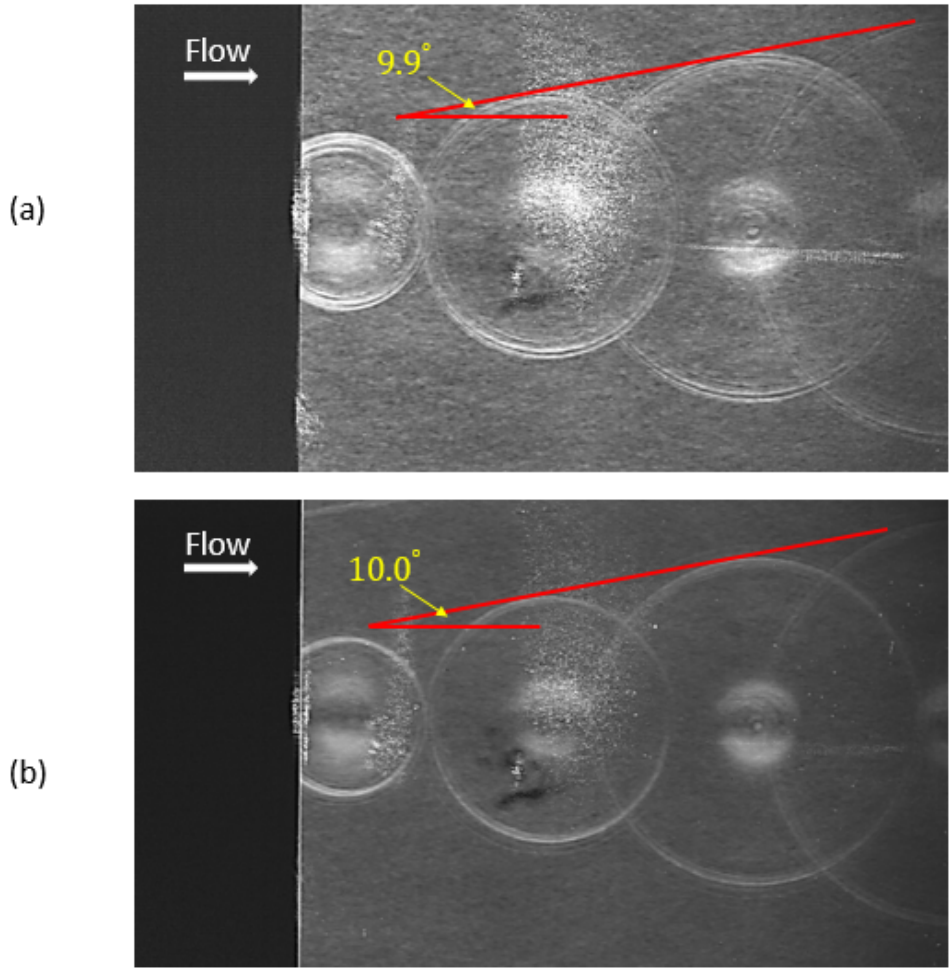


Figure 4.8: The standard deviation of the LISA high-speed schlieren images allow for measurement of the Mach number via the Mach cone effect. Measurements at (a) Condition 1 provide an angle of 9.9° ± 0.29° and for (b) Condition 2 yield an angle of 10.0° ± 0.28°. These correspond to a Mach number of 5.82 ± 0.17 and 5.76 ± 0.16 respectively.

4.2 AFRL Mach 6 HRF Cylindrical Lens FLDI

The results of this section are pulled directly from the author's conference paper in reference [99]. This work is an addendum to the prior section, demonstrating the capability of FLDI to the AFRL group at Wright Patterson in their efforts to study fluid structure interactions. This work also investigated the quality of cylindrical lens FLDI across a flat plate in measuring closer to the wall.

4.2.1 Experiment Setup

Facility Description and Conditions

The Mach 6 High-Reynolds Facility at Wright-Patterson Air Force Base was utilized for these experiments. This facility has already been previously described, so the only data points presented here are the run conditions for these experiments.

4.2.2 Model

A flat plate model is used for these experiments. A rendering of the model along with details of the location of the LA-FLDI beams is shown in Fig. 4.9. The model was injected into the flow for each run to reduce mechanical stresses and provide better wall temperature control. Unfortunately, the injection introduces a source of uncertainty with regards to beam position relative to the surface. The beams were aligned with the model in the fully injected state, but this height could slightly change during the running of the facility.

Linear Array-Focused Laser Differential Interferometry

The LA-FLDI setup used here begins with a 10 mW HeNe laser (Edmund Optics, Lumentum 1135P) operating at 632.8 nm, and identical lens focal lengths were used for the spherical and cylindrical lens configurations. The laser beam first passes through a polarizer (Thorlabs LPVISE100-A), which outputs 45° linearly polarized light. It is then expanded by a $f = -9$ mm plano-concave lens before passing through the diffractive optical element (HOLO/OR #MS-474-P-Y-A). The DOE used in this work was designed to create a 1 by 6 array. After the

DOE, the 6 beams propagate through a Wollaston prism (1.5 arc-minute, United Crystal) followed by a $f = 200$ mm plano-convex lens, which yields 6 FLDI beam pairs at the system focus. The catch-side of the system is somewhat symmetric, using a $f = 200$ mm plano-convex lens to collect the light, which then passes through an identical Wollaston prism. Beyond the prism, the beams propagate through a polarizer (Thorlabs LPVISE200-A) and are collimated by a plano-convex lens before entering the fiber optic collection unit. Each of the six beams is collected by its own fiber optic cable (Thorlabs M35L01) with a collimator (Thorlabs F240SMA-B), and the fibers are coupled to a individual photodetectors (Thorlabs). The data acquisition system (NI PXI system with components NI PXIe-8381, NI BNC-2110, and NI PXIe-6368) was set to 2 MHz, with all channels being read simultaneously. A ray trace of the system is shown in Fig. 4.10.

Fig. 4.11 show the beam profiles for both configurations. The cylindrical beams had a height of 2.96 mm, a beam spacing of 103 μm, and a pair spacing of 1.76 mm. The spherical case had a beam diameter of approximately 80 μm and a pair spacing of 1.87 mm. Due to the spacing between pairs, the profiles only show four of the six beams. To ensure that the beams passed through the boundary layer, the cylindrical beams were aligned to touch the surface while the spherical beams were aligned to within a millimeter of the surface. This highlights the potential of using cylindrical lenses across flat plate geometries, as the signal can reach the surface along the center line. This is due to the uni-axial focusing of the cylindrical lenses, which prevents clipping when the beam passes over the plate.

4.2.3 Results and Discussion

Spectral Results

To compare the spherical and cylindrical lens configurations, measurements were taken with both at the same streamwise location in the boundary layer. To ensure an accurate comparison, the focal point of each setup was placed at the centerline in the spanwise direction of the plate. To give multiple points for comparison, each FLDI setup was run at three different Reynolds numbers by varying the stagnation pressure. Figure 4.12 a and b show the spectra for each configuration for the lowest Reynolds number, showing a peak

frequency around 250 kHz. As the Reynolds number is increased, the plots begin to diverge in similarity. Figure 4.12 c through f show the spectra for increasing Reynolds numbers. While the spherical lens configuration still shows the expected turbulent peak, the cylindrical lens setup shows a larger influence from low frequency noise. Prior work has shown cylindrical lens FLDI to be sensitive to low frequency noise due to the singular focusing direction [50] so an increase in low frequency spectral noise is not unexpected, but the severity of the noise increase warranted an investigation. Figure 4.13 shows a comparison of freestream spectra between each FLDI configuration at different Reynolds numbers. The low frequency noise content is of the same order of magnitude for varying Reynolds numbers, eliminating facility noise increase as the culprit. The most likely conclusion left is an increase in edge effects due to the finite spanwise length of the flat plate. This point is further reinforced by Fig. 4.14, which shows the spectral content for both lens configurations at each Reynolds number condition. Since the freestream measurements are functionally the same regardless of Reynolds number, the highest Reynolds number freestream case is plotted for comparison. The spherical lens configuration shows a slight increase in mid-frequency noise (approx. 10 kHz) but shows the low frequency spikes that are seen in the freestream measurements. The cylindrical configuration shows how the low frequency spikes in the freestream case are drowned out by noise as the Reynolds number is increased. The spectra still have a roll off near the characteristic frequency, but that point is obscured by the increased noise level.

Velocity Estimation

Due to the streamwise orientation of the pairs, convective velocities of can be calculated by cross correlating the signals of two FLDI probe locations. Examples of the correlation coefficients for each FLDI configuration are shown in Fi. 4.15. Both configurations have a dominate peak occurring at a delayed time. Knowing the spacing between the two correlated points and dividing by the correlation time gives the convective velocity. Table 2 gives the convective velocities for each configuration at the various run conditions and unlike the spectral content, the convective velocities do not change with Reynolds number. These velocities also do not change when high pass filtering is applied to the data, indicating further

that the low frequency noise content does not lower the measured convective velocities. The uncertainties were calculated using Eq. (4.9) [70].

$$\Delta v = v\sqrt{(D/S)^2 + (1/f_s t_{corr})^2} \tag{4.8}$$

The spatial uncertainty is represented by the first term and is a function of the beam diameter, D, and the spacing between beam pairs, S. The velocity is directly computed using the beam pair spacing but that spacing is based on measurements from the centroid of beam points, which neglects the size of the beam. The second term is the temporal uncertainty, which is a function of the sample rate, fs, and the correlation time, tcorr. The simplest way to decrease the uncertainty is to increase the acquisition rate of the diagnostic, unlike increasing the beam pair spacing. While outside the scope of this paper, the spacing between pairs will have a limit based on the flow being measured.

Summary

Cylindrical and spherical lens FLDI are compared on a flat plate in Mach 6 flow. The spectra between the two configurations are similar in the lowest Reynolds number case but show significant deviation as Reynolds number increases. Given the lack of variation with Reynolds number in the freestream measurements, the initial conclusion is the cylindrical lens configuration is heavily affected by the edge effects of the plate, especially at lower frequencies. Given that cylindrical lens FLDI is designed to measure close to the surface of planar models, the detrimental impact of edge effects limits the run conditions that it will be effective. However, the edge effects do not appear to impact the velocity measurements, as both configurations report velocities within the uncertainty of the measurement.

Table 4.4: A summary of the tunnel operating conditions used in this work.

Test	**Setup**	T_0 $[K]$	p_0 $[MPa]$	Re/x $[\times 10^6\ m^{-1}]$
Run 1	Cyl. LA-FLDI	555	4.82	34.2
Run 2	Sph. LA-FLDI	555	4.82	34.2
Run 3	Cyl. LA-FLDI	555	8.27	58.5
Run 4	Sph. LA-FLDI	555	8.27	58.5
Run 5	Cyl. LA-FLDI	555	12.41	87.8
Run 6	Sph. LA-FLDI	555	12.41	87.8

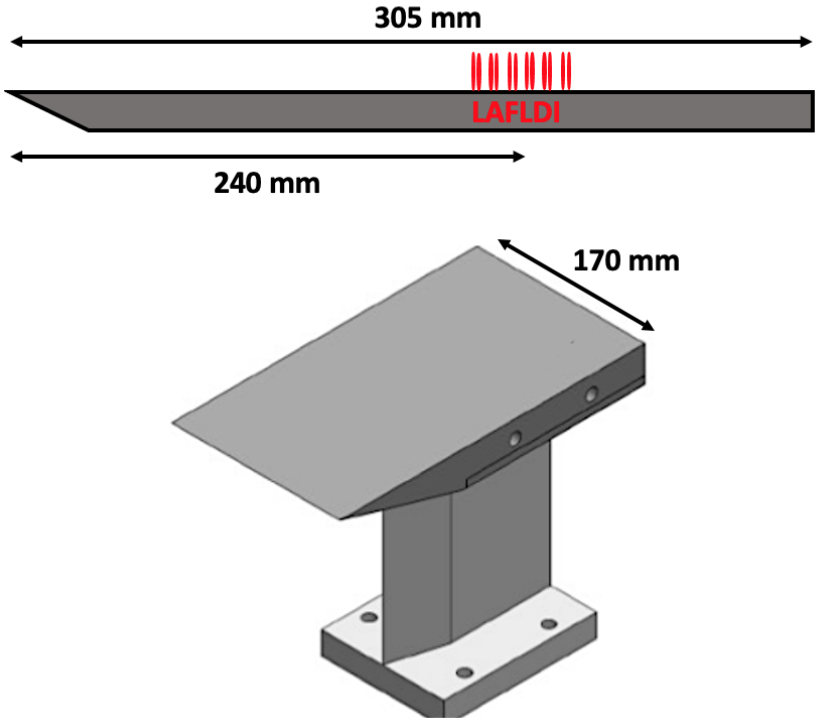


Figure 4.9: The flat plate model used in this work.

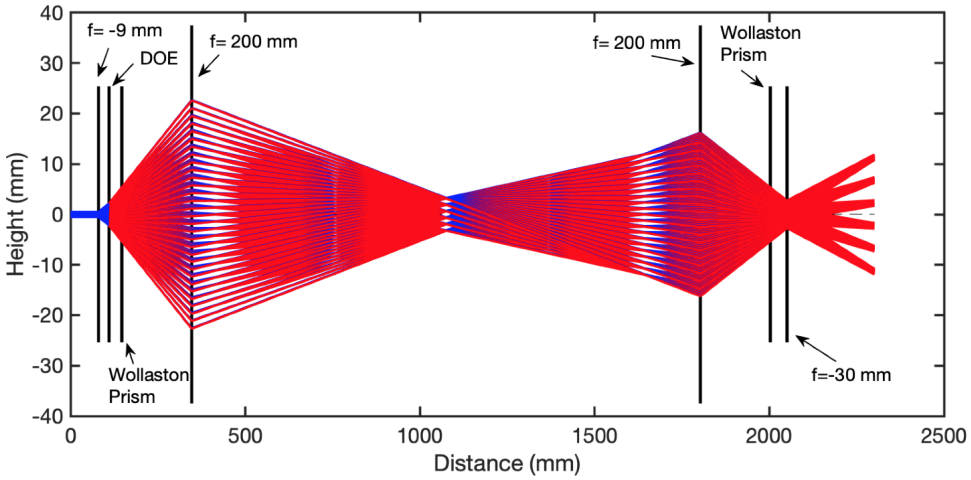


Figure 4.10: A calculated ray trace showing the LA-FLDI setup with six focused beam pairs. Note that the polarizers are not shown since they don't affect beam geometry.

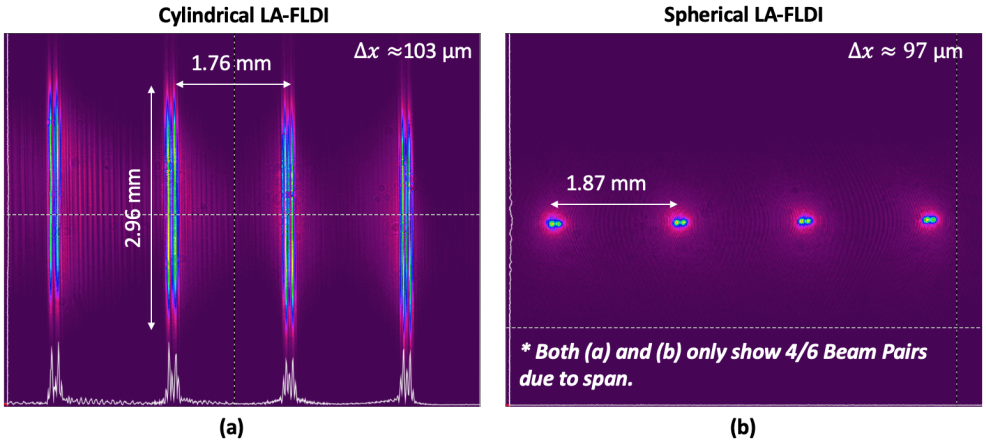


Figure 4.11: Images of the LA-FLDI beams at the focus.

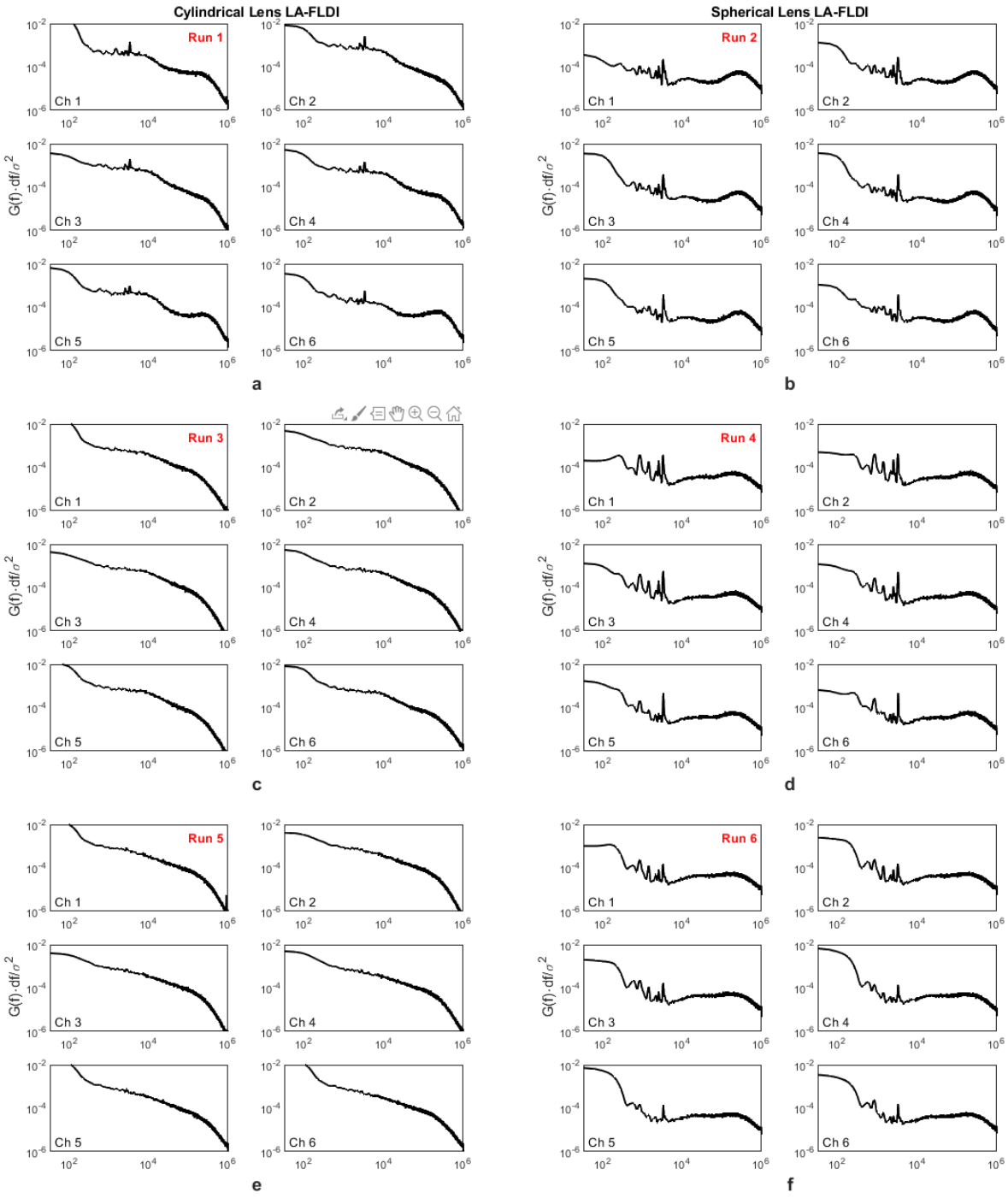


Figure 4.12: Spectra for the intermediate and highest Reynolds number conditions.

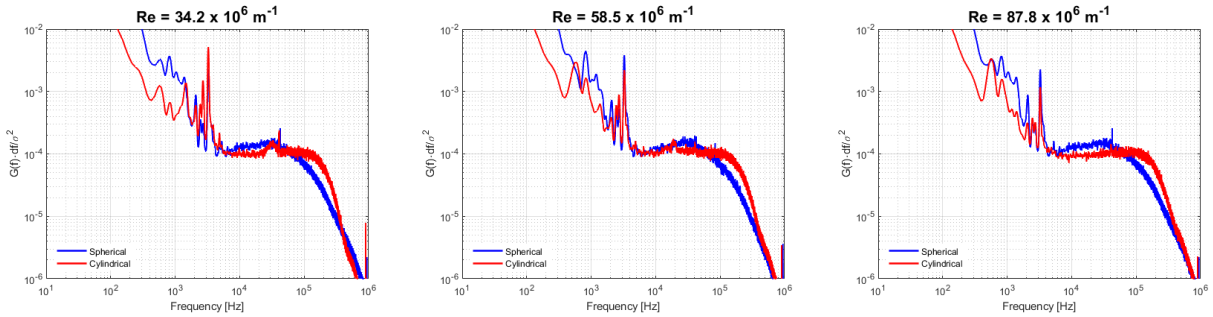


Figure 4.13: Comparison of freestream spectra between the spherical and cylindrical configurations for each Reynolds number.

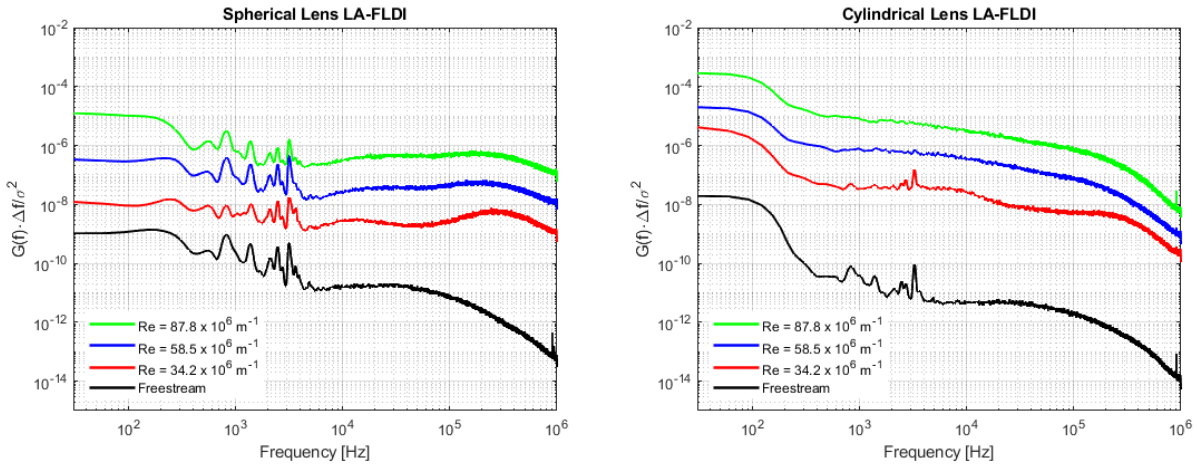


Figure 4.14: Images of the LA-FLDI beams at the focus.

Table 4.5: A summary of initial velocity calculation with the two LA-FLDI configurations.

Test	**Setup**	u_{FLDI} $[m/s]$	U_∞ $[m/s]$	u_{FLDI}/U_∞	$Uncertainty[m/s]$
Run 1	Cyl. LA-FLDI	975	997	0.978	55
Run 2	Sph. LA-FLDI	981	1002	0.979	52
Run 3	Cyl. LA-FLDI	975	1000	0.975	55
Run 4	Sph. LA-FLDI	981	1003	0.978	52
Run 5	Cyl. LA-FLDI	975	1002	0.973	55
Run 6	Sph. LA-FLDI	981	1007	0.974	52

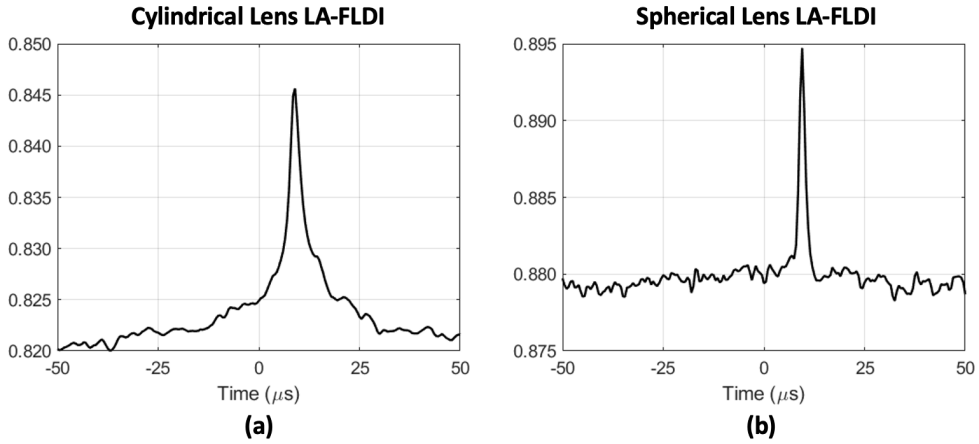


Figure 4.15: Initial analysis the correlation coefficients for determining the velocity from two channels of the LA-FLDI.

4.3 AFRL Camera FLDI

The results of this section are pulled directly from the author's conference paper in reference [100]. This experimental effort investigated the efficacy of using a high-speed camera as an FLDI detector, comparing it with a traditional photodiode setup, and assessing the viability of it to improve the versatility of FLDI.

4.3.1 Experimental Setup

Facility Description and Conditions

The Mach 2.3 and Mach 2 tunnels at UTSI were used for these experiments. Both facilities operate at the same stagnation pressure and temperature, details of which are shown in Table 2.1. The Mach 2.3 facility was used as for the initial exploration of the camera as a detector due to the convenient setup available at the time and the experiments were moved to the Mach 2 for a more detailed investigation into the topic. To better investigate the cylindrical lens FLDI across a boundary layer, a flat plate at an angle of attack of 6° was installed in the Mach 2 to provide initial data across a thin boundary layer.

Linear Array-Focused Laser Differential Interferometry

The LA-FLDI setup used here begins with a 10 mW HeNe laser (Edmund Optics, Lumentum 1135P) operating at 632.8 nm, and identical lens focal lengths were used for the spherical and cylindrical lens configurations. The laser beam first passes through a polarizer (Thorlabs LPVISE100-A), which outputs 45° linearly polarized light. It is then expanded by an $f = -9$ mm plano-concave lens before passing through the diffractive optical element (HOLO/OR #MS-474-P-Y-A). The DOE used in this work was designed to create a 1 by 6 array. After the DOE, the 6 beams propagate through a Wollaston prism (1.5 arc-minute, United Crystal) followed by an $f = 200$ mm plano-convex lens, which yields 6 FLDI beam pairs at the system focus. The catch-side of the system is somewhat symmetric, using an $f = 200$ mm plano-convex lens to collect the light, which then passes through an identical Wollaston prism. Beyond the prism, the beams propagate through a polarizer (Thorlabs LPVISE200-A) and are collimated by a plano-convex lens before entering the fiber optic collection unit. Here

we monitor 2 of the 6 beams with photodetectors and a 50/50 beam splitter sent all six beams to a Photron SA-Z operated at 1.008 MHz while the data acquisition system for the photodetectors was set to 5 MHz. Maximize the camera's field of view, the $f = -9$ and $f = 200$ spherical lenses were swapped for identical focal length cylindrical lenses. This focuses the beam in one direction, resulting in a line that can be viewed entirely by the camera sensor. To increase the height of the beams, an $f = -50$ mm and an $f = 100$ mm lens were placed on the throw side of the system. Figure 4.32 lays out a schematic of the FLDI systems used. The schematic outlines the cylindrical lens setup but is identical to the spherical lens system except for the optics highlighted in red.

Fig. 4.17 shows an image of the beam at each lens configuration focus. The cylindrical lens setup utilized the secondary Wollaston prism and polarizer in place of the DOE. This resulted in only two beam pairs but increased the distance between the pairs to keep the velocity measurements similar to those of the spherical orientation. To estimate the thickness of the floor boundary layer, the cylindrical lens signal was expanded to 3 mm for the signal to straddle the edge of the boundary layer. The boundary layer edge was measured at 11 mm from the floor based on PIV results by Kocher *et al.* [101]. With the camera sampling at 1.008 MHz, the pixel resolution available was 384 by 16 pixels. This gave a pixel to millimeter resolution of $128 px/mm$, allowing for a high accuracy in the spatial measurement across the signal line. The spherical lens system was used to measure the convective velocities and compare their similarities to the theoretical and measured velocity profiles of this boundary layer. To accomplish this, the spherical system was translated from the floor to the freestream on posts, with each measurement point recorded. To ensure the accuracy of each measurement, the signal was measured at a determined point away from the surface and then lowered while using the beam profile camera. This camera has a resolution sensitive to the 10's of μm's, allowing for precise location each time the measurement location was translated. The author will note that the system could only reach 1 mm from the surface before clipping obscured a majority of the signal.

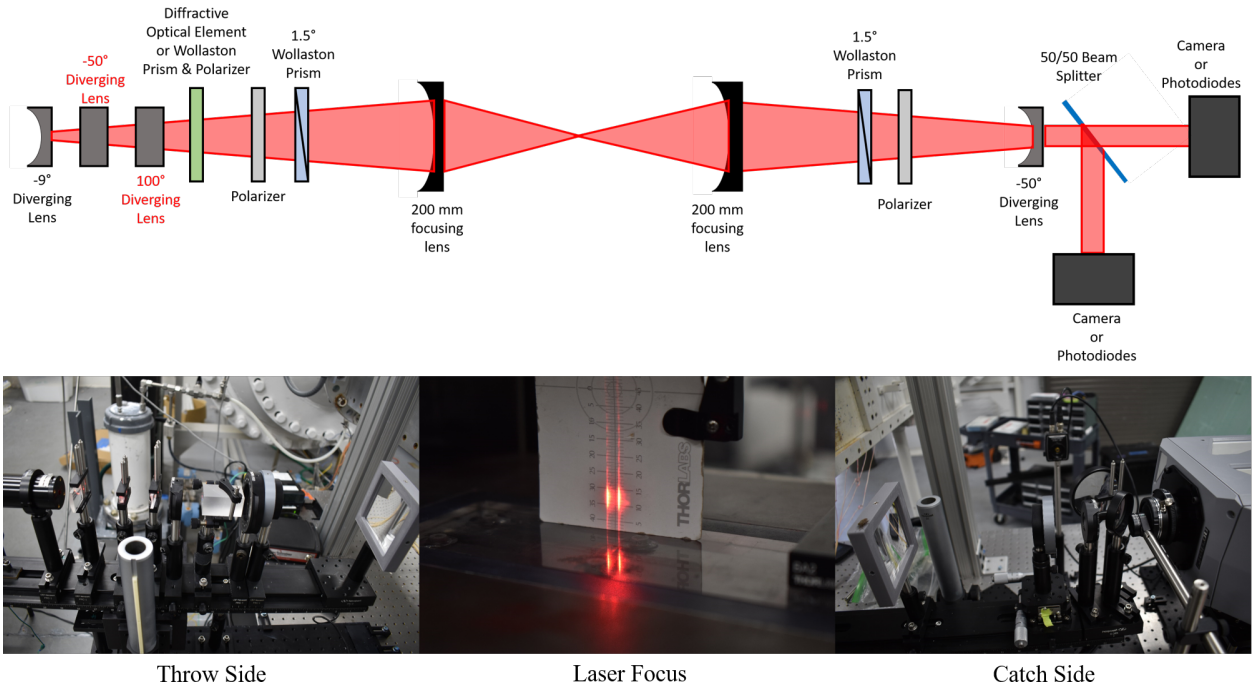


Figure 4.16: Schematic and setup of the FLDI system used in these experiments. The red text highlights the beam expansion optics only used in the cylindrical lens configuration.

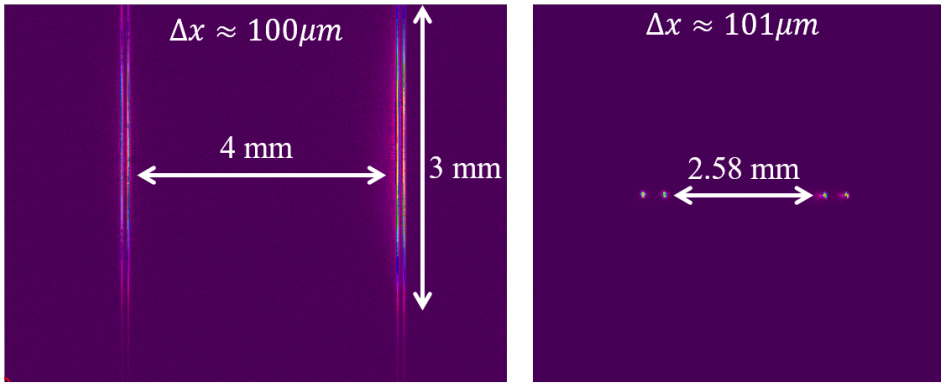


Figure 4.17: Images of the LA-FLDI beam profiles at the focus. Only two are shown since the majority of measurements only utilize two points.

4.3.2 Results and Discussion

Mach 2.3 Wind Tunnel

The initial investigation using a camera as an FLDI detector focused primarily on the comparison of turbulent boundary layer spectra between the camera and the traditional photodetectors. The focal point of the FLDI beams was placed close to the floor of the tunnel. While not precisely measured for this initial investigation, the beam location was close enough to be submerged in the boundary layer but not so close that the beam would be clipped by the wall itself. Figure 4.18 shows the variable signal sizes from spherical lens FLDI on the camera sensor and the corresponding power spectra with each signal. The red lines in each spectra represent the entire signal while the blue lines represent the spectra collected using a quarter of the signal on the camera.

While the entire signal produces the expected spectra, the partial signal results in an increase of low frequency noise and a deviation in the higher frequency regime. While this is of little consequence to the point measurement with spherical lenses, it will play a role when using cylindrical lenses. Figure 4.19 shows good agreement between the camera and photodiode spectra in the frequency regime available to the camera. The dotted line is a reference for the expected negative five thirds slope found in turbulent boundary layer spectra. Both signals peak round 50 kHz which is the characteristic frequency for the floor boundary layer in the Mach 2.3 facility. The power spectra due begin to diverge around the upper end of the camera's frequency resolution but the spectra still show the expected trends in the frequency content. When the DOE is inserted, convective velocities of the boundary layer can be measured. Table 4.6 gives the velocity results for both the camera and diodes. Both acquisition types provided velocities around 1% of each other. Given the good agreement between the camera and photodiodes, this investigation was expanded upon in the UTSI MAch 2 facility.

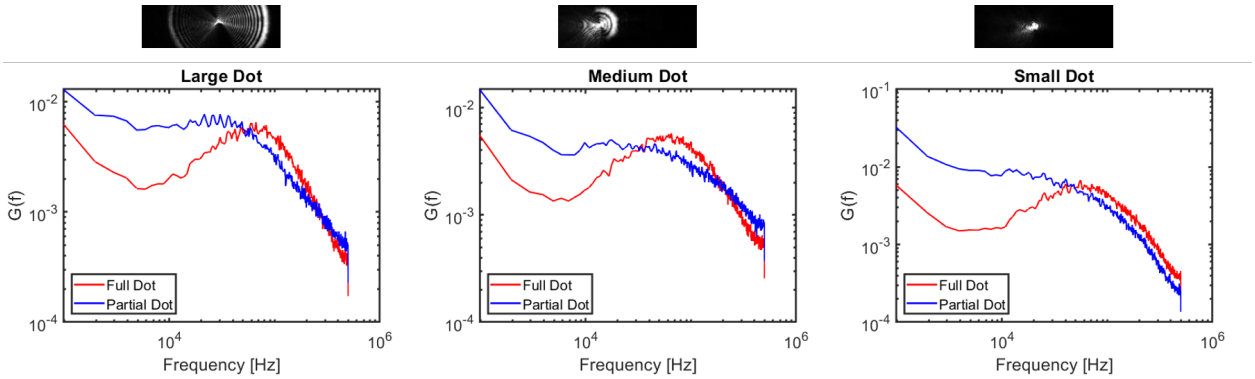


Figure 4.18: A comparison of signal size on the camera sensor and the effect of selecting only a region of interest versus the whole laser.

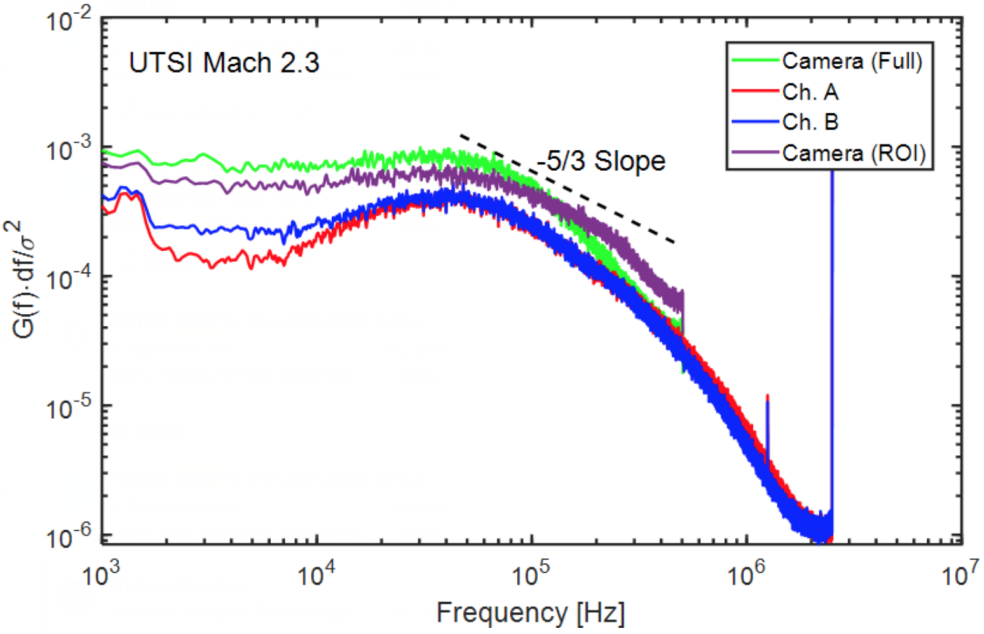


Figure 4.19: Comparison of power spectra from using the camera as the collection system to data collected with a photodetector.

Table 4.6: Convective velocity comparison between the camera and diode.

Detector	Velocity [m/s]	Uncertainty [m/s]
Camera	486	97
Diode	480	19

Mach 2 Wind Tunnel

To build on the initial investigation, the camera FLDI detection was deployed in the UTSI Mach 2 wind tunnel. Using the spherical lens FLDI configuration, the spectra and velocities of the photodetectors and camera were compared. Figure 4.20 shows a comparison of the freestream and boundary layer spectra of each detection method, with the boundary layer spectra being taken at 5 mm or 0.45δ from the floor. Both methods show strong agreement between the two detectors with a slight deviation at the higher frequencies of the camera. A major point of emphasis that came about during these experiments was the issue of signal vibration on the camera sensor. Figure 4.21 shows the camera spectra from two different boundary layer locations. Figure 4.21 a. shows a significant increase in noise between 1 and 10 kHz compared to that of Fig. 4.21 b. Initially it was thought that the noise came from tunnel vibration as the signal had a greater chance of clipping; however, there was no change in the photodetector spectra at each of those locations. From this, it was determined that a portion of the signal on the camera was moving disappearing from the images. Considering the consistency of the photodetectors, it was concluded that the vibration was coming from the camera, where each pixel is 10 μm by 10 μm. Given the restricted sensor resolution of 384 pixels wide by 16 pixels tall, the camera system is extremely sensitive to vibrations. These vibrations did not appear to impact the velocity measurements and only contaminated the low frequency portion of the signal.

To characterize the camera's accuracy in measuring convective velocity, the spherical lens system was translated through the boundary layer from near the wall to the top of the boundary layer that was reported in previous work. This resulted in eleven measurement points with the goal of replicating the velocity profile of a turbulent boundary layer. Figure 4.22 a. shows the normalized turbulent boundary layer profile derived by Sun and Childs [75] overlaid with the convective velocities measured with a photodiode at each boundary layer location. Figure 4.22 b. shows those same values overlaid on the Y^+ U^+ scaling using the Clauser-Chart method with the compressible correction. This is the same method used by Kocher et al. [101] and more detail on it can be found in their references. Figure 4.22 shows good agreement for the photodiode velocities with respect to the theoretical velocities.

Figure 4.23 shows the normalized velocities calculated using the camera as a detector. Only eight of the measurement locations were taken with the camera due to increasing difficulty in alignment. The plot shows the larger uncertainty in the camera measurement along with less accuracy compared to the photodiode. This is a result of the substantially lower sampling rate achieved by the camera. This phenomenon will be explored further in the uncertainty discussion later in the paper.

To better utilize the camera's larger pixel region, the spherical lenses were swapped for cylindrical lenses of the same focal lengths and measurements were taken near the edge of the floor boundary layer. Figure 4.24 shows power spectra near the edge of the floor boundary layer. All the signals display the characteristic roll off expected in a turbulent boundary layer spectra while the uppermost signal shows a slight flattening in the higher frequency ranges. Multiple runs were made, adjusting the signal around the known edge of the boundary layer but no conclusive distinction could be made between the intermittent region and the freestream. The authors were left to conclude that the thick floor boundary layer had an intermittent region that was too thick relative to the height of the signal for a clear measurement to be made. Due to facility time running out, the decision was made to switch the experiment to a smaller boundary layer on a flat plate. With this slight deviation being the only noticeable deviation, the decision was made to use this setup on a flat plate in the same tunnel.

The flat plate model was angled at 5°, yielding a an edge Mach number of 1.8. The primary purpose of using this model was to quickly produce a thin, turbulent boundary layer that the entire signal could be used across. Figure 4.25 shows the spectra across the thin plate boundary layer. The lowest spectrum on the graph corresponds to the signal closest to the plate surface and shows a distinct turbulent profile. As the points are moved away from the wall, the turbulent spectra dissipate until the freestream is reached in the upper range of the signal. The two interior points show a blend of turbulent and freestream content consistent with the intermittent region of the upper boundary layer. Based on the location of the freestream spectra on the signal, the boundary layer thickness for this plate was estimated to be 1.9 mm. While the spatial resolution of the measurement is

high, the preliminary nature of this measurement is not fully conclusive and requires more experimentation across different configurations.

Velocity and Uncertainty Calculation

A substantial benefit of multi-point FLDI is the estimation of convective velocities. This is achieved by cross-correlating the two of the beam signals as shown in Fig. 4.26. The convective velocity is then calculated from the known spacing between the two beams. While simple in its approach, the main area of concern comes from the uncertainty of the measurement, described by Eq. 4.9.

$$\Delta v = v\sqrt{(D/S)^2 + (1/f_s t_{corr})^2} \tag{4.9}$$

The spatial uncertainty is represented by the first term and is a function of the beam diameter, D, and the spacing between beam pairs, S. The velocity is directly computed using the beam pair spacing but that spacing is based on measurements from the centroid of beam points, which neglects the size of the beam. The second term is the temporal uncertainty, which is a function of the sample rate, fs, and the correlation time, tcorr. This term provides the majority of uncertainty, with the main driver of the uncertainty being the sample rate of the acquisition technique. With constant beam spacing, the camera velocities have an uncertainty of approximately 20% of the calculated velocity while the photodiodes have an uncertainty of 4%. This uncertainty manifests itself in the velocity resolution available to the detector with a set beam spacing. Figure 4.23 illustrates this concept by showing the constant velocity measured by the camera as it traverses the boundary layer. Since the beam spacing never changes, only the time delay between the signals would change with changes in velocity, yielding a minimum velocity the camera can resolve for that configuration.

This minimum velocity change can be defined by Eq. 4.10, where Δu is the change in velocity that can be resolved by the system, U_i is the measured velocity starting with the freestream velocity of the facility, Δx is the spacing between beam pairs from Fig. 4.33, and f is the sampling rate of the system.

$$\Delta u = U_i - \frac{\Delta x}{\frac{\Delta x}{U_i} + \frac{1}{f}} \tag{4.10}$$

Using the isentropic freestream velocity of the Mach 2 facility as the initial velocity for Eq. 4.10, the Δx from Fig. 4.33, and the sampling frequencies for each detection method, the minimum velocity changes that each system can resolve based on the velocity at the measurement point are shown in Fig. 4.27. At the higher velocities, the camera has a much higher minimum velocity that it can resolve than the photodiode due to the lower sampling rate for the camera, only coming together below 100 m/s. For a given flow field, such as turbulent boundary layer, Eq. 4.10 can be utilized in predicting how well a given FLDI system can resolve the convective velocity profile and what sampling rate and spacing are needed to achieve the desired velocity resolution.

Conclusions

A high-speed camera is compared to photodiodes as a detection method for FLDI. The spectral content is similar in the regions of sampling overlap, with the camera appearing to be more sensitive to low frequency noise than the photodiodes. The lower maximum sampling rate for the camera limits the use of the camera in convective velocity measurements as the uncertainty is too high and the velocity resolution is not sufficient to resolve fine scale velocity changes. The large sensor size does provide a significant advantage when using cylindrical lens configuration and shows great promise in measuring thing boundary layers, especially in impulse and large-scale facilities where traditional velocimetry techniques are unavailable. While the large boundary layer on the wind tunnel floor yielded indeterminate results, the thin boundary layer formed on the flat plate showed distinct regions between the boundary layer, intermittent region, and freestream.

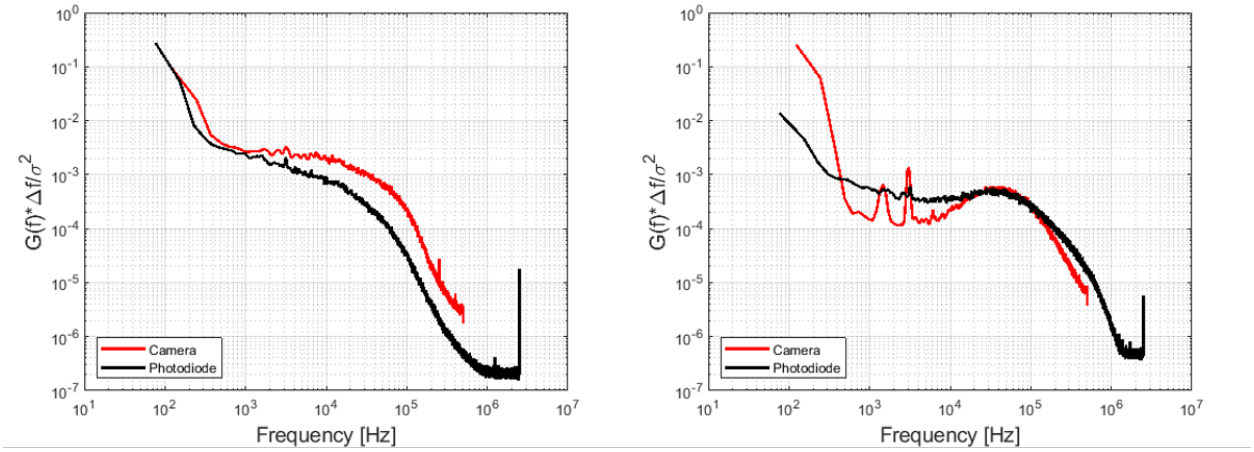


Figure 4.20: Freestream and boundary layer power spectra for the photodetector and camera. (a) was measured at 15 mm or 1.36δ from the floor and (b) was measured at 5 mm or 0.45δ from the floor

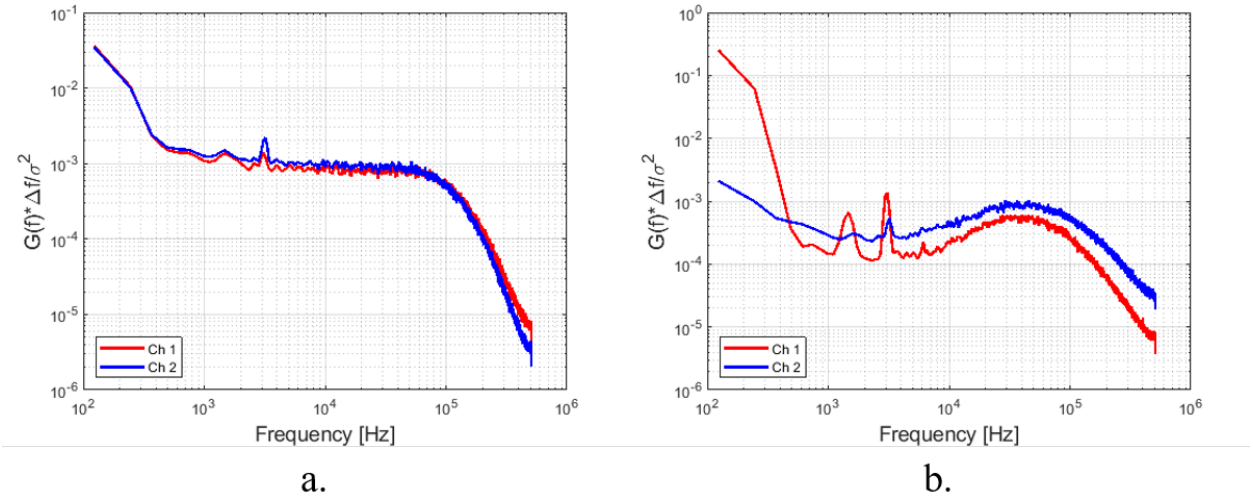


Figure 4.21: Freestream and boundary layer power spectra for each signal on the camera. (a) was measured at 1 mm or 0.27δ from the floor and (b) was measured at 5 mm or 0.45δ from the floor

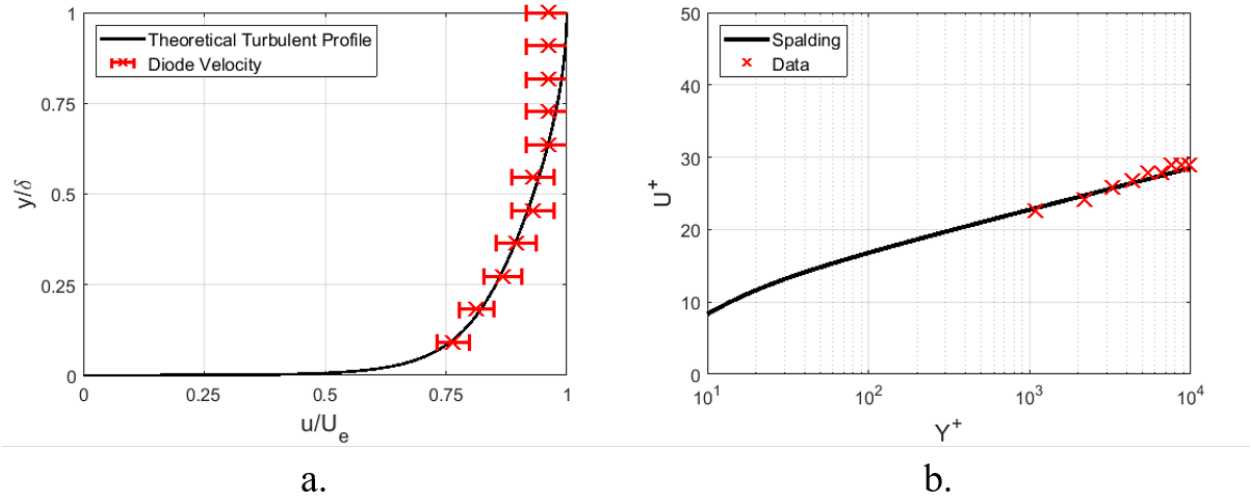


Figure 4.22: (a) Photodiode velocity profile normalized by the boundary layer thickness and freestream velocity. (b) Inner variable scale velocity profiles of photodiode measured velocities

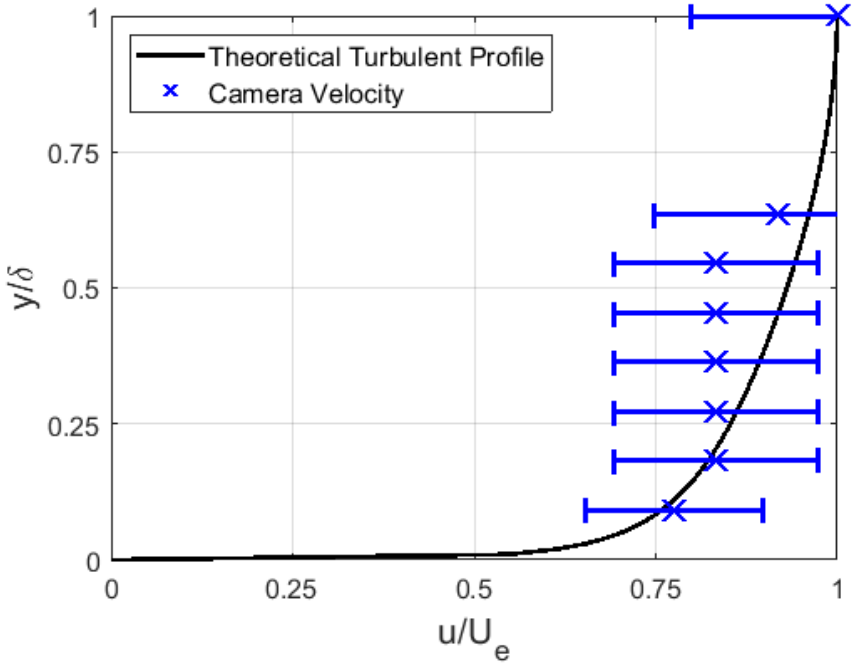


Figure 4.23: Camera velocity profile normalized by the boundary layer thickness and freestream velocity.

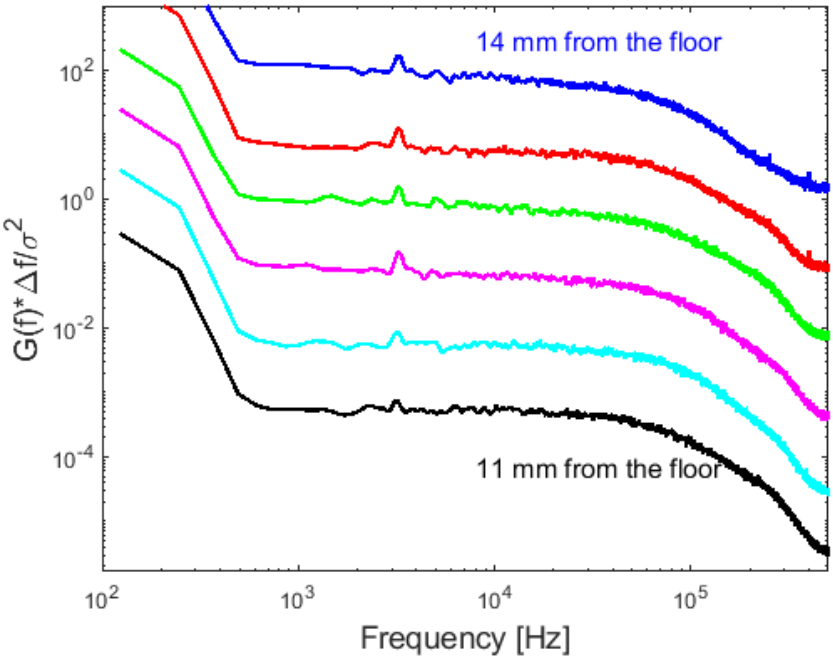


Figure 4.24: Power spectra across the upper edge of the floor boundary layer. Each spectra represents a distinct point along the signal.

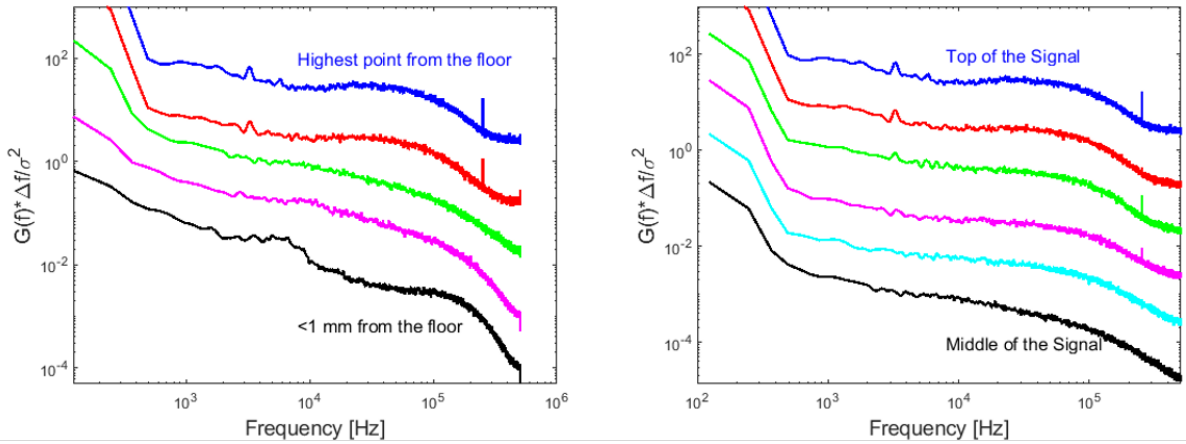


Figure 4.25: (a) Power spectra across the plate boundary layer. Each spectra represents a distinct point along the signal. (b) Power spectra across the upper half of the plate boundary layer signal

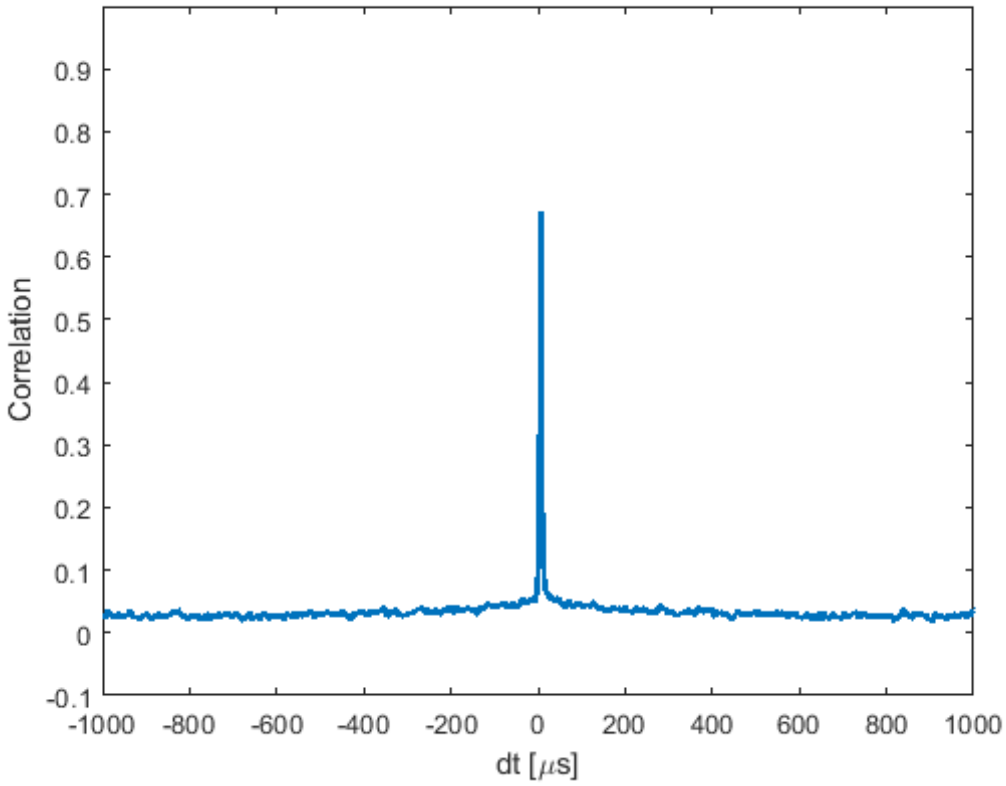


Figure 4.26: Correlation plot for convective velocity calculation.

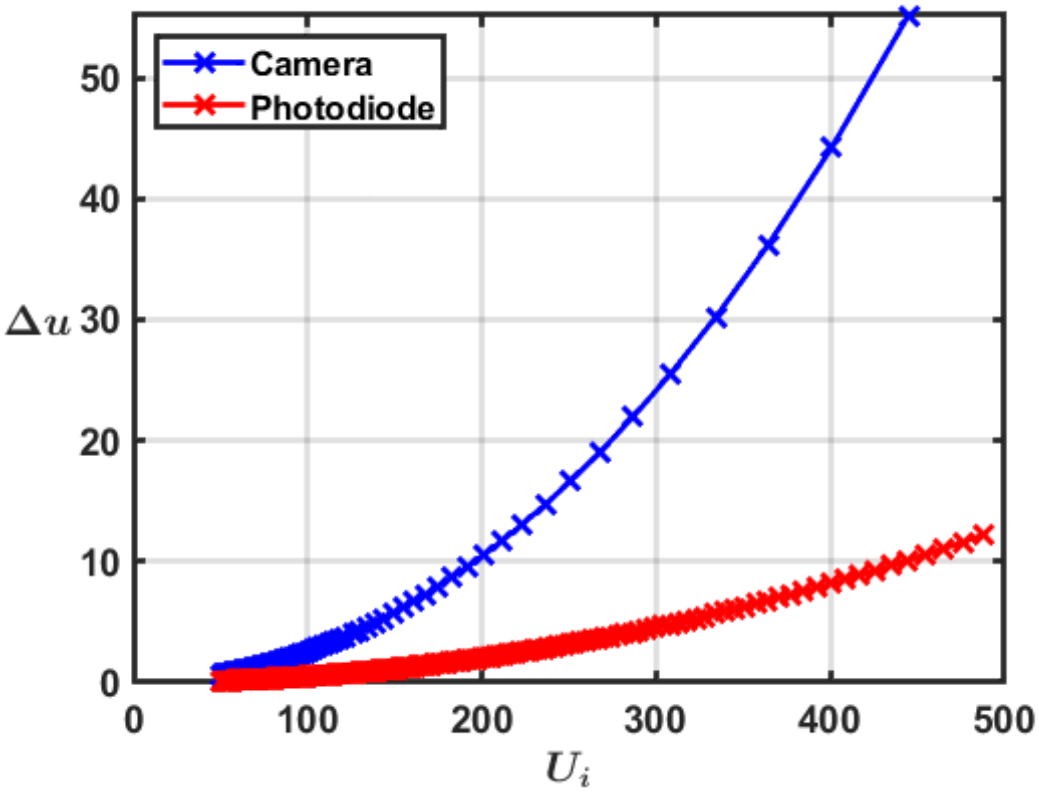


Figure 4.27: Comparison of the minimum resolvable velocity changes for a given velocity between the photodiode and camera. Note the diode sampling rate is 5 MHz while the camera is 1.008 MHz.

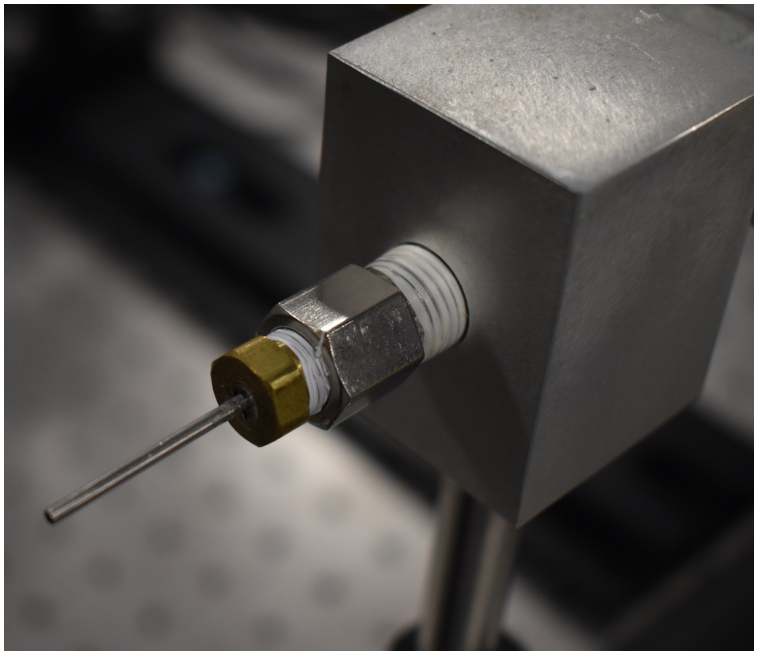
4.4 Camera Based Cylindrical Lens FLDI

The results of this section are pulled directly from the author's pending journal paper that is in review. This experimental effort characterizes the combined cylindrical lens FLDI system and the high-speed camera detector. The setup is characterized over a benchtop tube jet before being used to measure a thin, turbulent boundary layer on a flat plate at Mach 2.

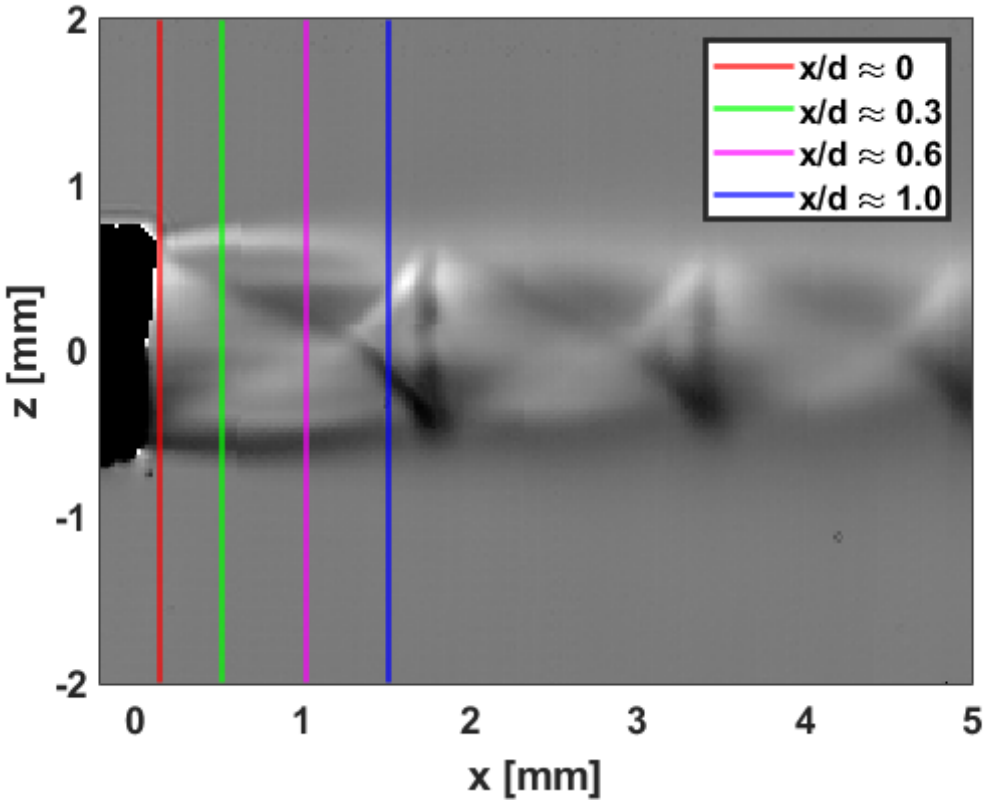
4.4.1 Experiment Setup

Tube Jet

To characterize the response of the cylindrical lens FLDI when using the camera, a 1.5 mm diameter tube jet was set up on the bench top, shown in Fig. 4.28a. The jet used pure nitrogen and flow was controlled from the pressurized container by manually opening a valve. A nominal supply pressure of 344.7 kPa gauge (50 psig) was used, which was monitored by an omega pressure transducer placed where the nitrogen connected to the jet inlet. To visualize the tube jet, a lens based schlieren system was set up on the bench top. Figure 4.30 shows a schematic of this schlieren setup in relation to the jet. An in-house LED produced light, pulsed at 200 kHz, which was focused by a 150 mm lens onto an iris to create a point light source. The light then expands onto a 400 mm lens which collimates the beam as it travels over the jet. After the jet, the light then reaches another 400 mm lens that focuses it onto a knife edge and into a Photron SA-Z equipped with a 300 mm Sigma camera lens. The camera frame rate is synchronized with the LED at 200 kHz, with the system triggered and synchronized with a delay generator. Using the adjustments on the camera lens, the image is focused on the jet nozzle and the resulting image has a spatial resolution of 44 px/mm. Figure 4.28b shows a mean schlieren image of the jet at the nominal operating pressure, with the four FLDI measurements taken along the jet highlighted by the individual colored lines. The cylindrical signal was oriented to bisect the jet, as shown by the lines in Fig. 4.28b, to demonstrate that the cylindrical signal was discretely sensitive at different spatial points along the signal.



(a) Tube jet used



(b) Average tube jet schlieren.

Figure 4.28: Tube jet used for cylindrical lens FLDI characterization with the camera.

Mach 2 Facility and Flat Plate

To compare the camera and a photodiode and illustrate the utility of the cylindrical lens combined with a camera detector, the Mach 2 tunnel at UTSI, described in earlier sections, was used. For this set of experiments, three different Reynolds numbers were used, and their corresponding tunnel conditions are compiled in Table 4.7.

Comparisons between the two detectors using the spherical lens LA-FLDI were done using the turbulent floor boundary layer, measured at 11 mm by Kocher *et al.* [101]. The well characterized velocity of the floor boundary layer made it ideal for comparisons of convective velocities between the two detectors. The substantial thickness also allowed for multiple measurement points within the boundary layer to properly resolve the velocity profile without requiring sub-millimeter precision when translating the system. Since the cylindrical lens signal has a larger spatial range of measurement, a flat plate is used to generate a thin boundary layer, shown in Fig. 4.29, with zero angle of attack and a full tunnel span to reduce the impact of edge effects. The plate produces a thin, turbulent boundary layer near the leading edge that can be fully enveloped by the cylindrical FLDI signal, allowing for measurements of the entire boundary layer in a single run. The two measurement locations relative to the leading edge are shown by the two wall-normal lines and illustrate how the FLDI signal was with respect to the boundary layer. To ensure the signal was reaching the surface of the model, the signal was placed low enough for it to be partially cut off by the plate during the run.

Schlieren

To visualize the tube jet, a lens based schlieren system was set up on the bench top. Figure 4.30 shows a schematic of this schlieren setup in relation to the jet. An in-house LED produced light, pulsed at 200 kHz, which was focused by a 150 mm lens onto an iris to create a point light source. The light then expands onto a 400 mm lens which collimates the beam as it travels over the jet. After the jet, the light then reaches another 400 mm lens that focuses it onto a knife edge and into a Photron SA-Z equipped with a 300 mm Sigma camera lens. The camera frame rate is synchronized with the LED at 200 kHz, with the

system triggered and synchronized with a delay generator. Using the adjustments on the camera lens, the image is focused on the jet nozzle and the resulting image has a spatial resolution of 44 px/mm.

In the Mach 2 facility, a modified Z-type schlieren system was used. The light source, lens, and iris were the same as the linear system used with the tube jet. Instead of lenses, the light was collimated using a parabolic mirror with a 2.5 m focal length. A schematic of the system is diagrammed in Fig. 4.31, showing the use of an additional flat mirror to turn the light after the test section due to space limitations. A Photron SA-Z was used, acquiring images at 20 kHz.

Focused Laser Differential Interferometry Setup and Characterization

There are two FLDI systems used in this work, one utilizing spherical lenses, the other cylindrical lenses. Both systems have a camera as the detector; however, the cylindrical lens system utilizes additional lenses to expand the measurement signal. These changes are highlighted in Fig. 4.32, where the additional optics for the camera are labeled in green, the additional expansion lenses for the cylindrical system are labeled in blue, and the diffractive optical element (DOE) for the spherical system in red. For the two FLDI systems used in this work, both begin with a 10 mW HeNe laser (Edmund Optics, Lumentum 1135P) operating at 632.8 nm with an approximate 1.0 mm diameter. The laser beam passes through an $f = -9$ mm lens. The beam then propagates through a polarizer (Thorlabs LPVISE100-A), which outputs 45° linearly polarized light before passing through a Wollaston prism (1.5 arc-minute, United Crystal) followed by an $f = 200$ mm convex lens. The catch-side of the system is somewhat symmetric in setup, using an $f = 200$ mm convex lens to collect the light, which then passes through an identical Wollaston prism. Beyond the prism, the beams propagate through a polarizer (Thorlabs LPVISE200-A) and are collimated by a concave lens before passing through a 50/50 beam splitter. Here, the beam is monitored with a photodiode sampling at 5 MHz in one direction, while the other direction has the beam sent to a Photron SA-Z operated at 1.008 MHz, with two neutral density filters (Thorlabs NE10A-A and NE13A) in front to reduce the intensity of the incoming light.

Table 4.7: A summary of the conditions used at during these tests. The list includes the measured stagnation pressure (P_0) and stagnation temperature (T_0) along with the isentropically calculated static pressure (P_∞), static density (ρ_∞), and unit Reynolds number (Re_x)

Parameter	Condition 1	Condition 2	Condition 3
$P_0[kPa]$	206.8	241.3	275.8
$T_0[K]$	295	295	295
$P_\infty[kPa]$	26.4	30.8	35.2
$\rho_\infty[kg/m^3]$	0.561	0.654	0.748
$Re/x[\times 10^6 m^{-1}]$	25.8	30.1	34.4

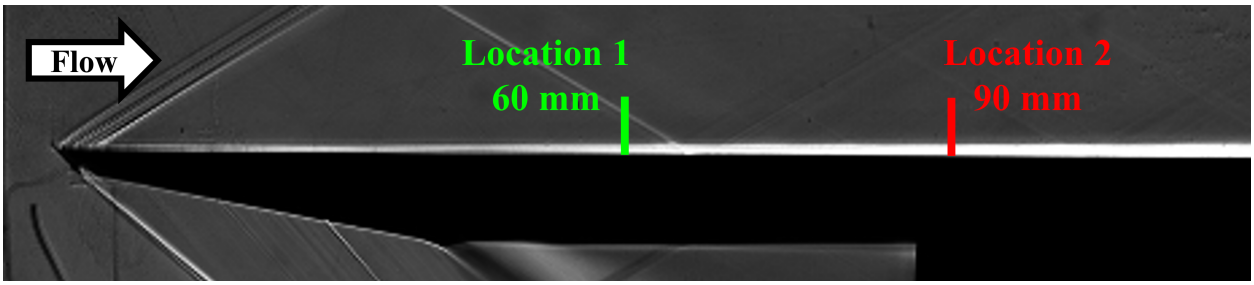


Figure 4.29: Average schlieren image of the flat plate model with FLDI measurement locations highlighted.

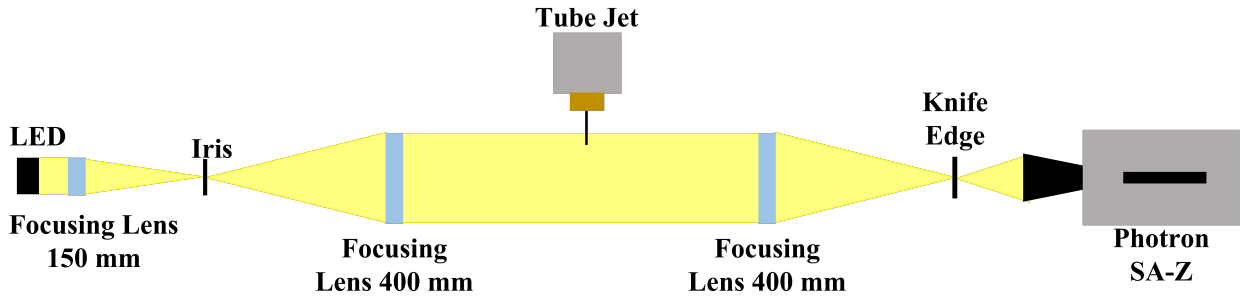


Figure 4.30: Schematic of the bench top schlieren setup used to image the tube jet.

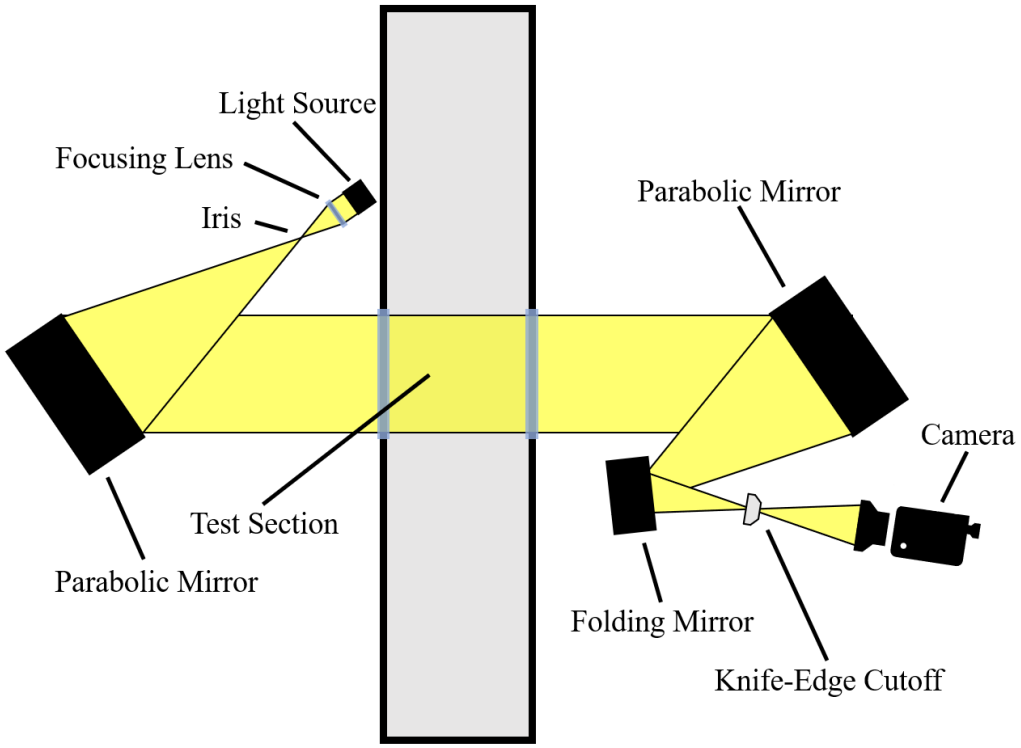
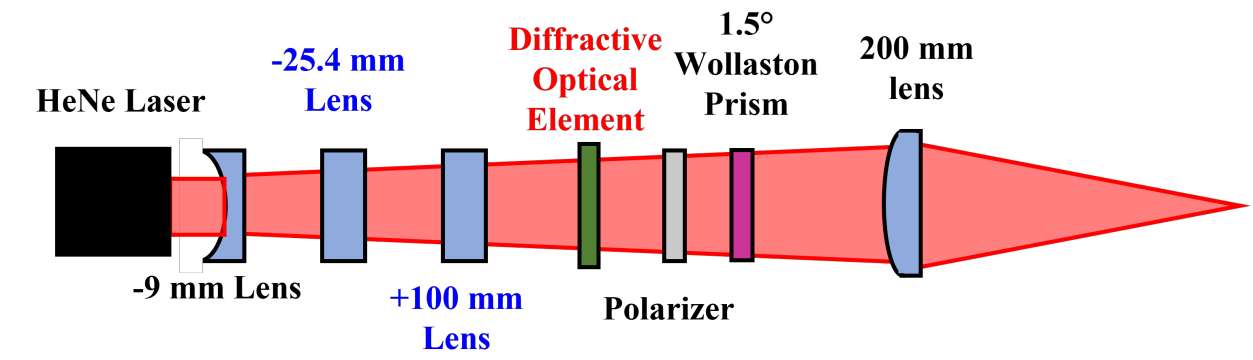
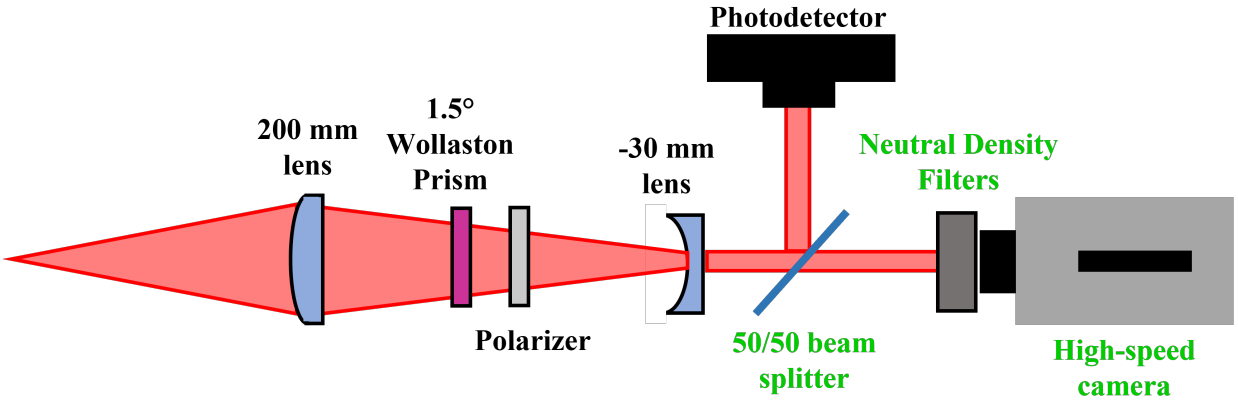


Figure 4.31: Schematic of the modified Z-type schlieren setup used in the Mach 2 facility [102].



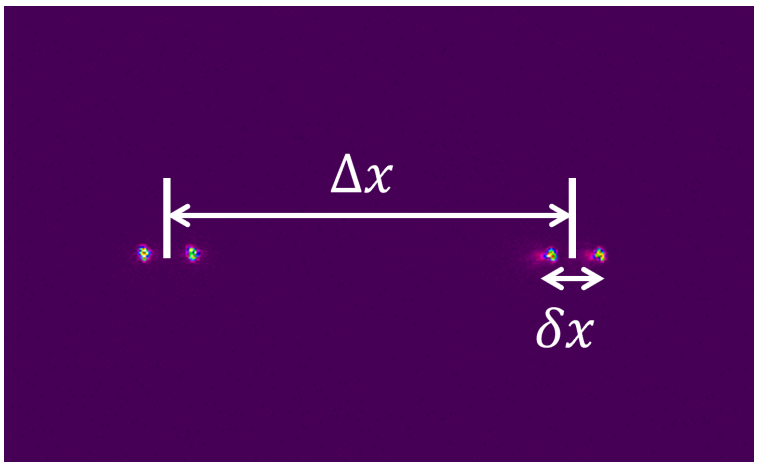
(a) FLDI system throw side



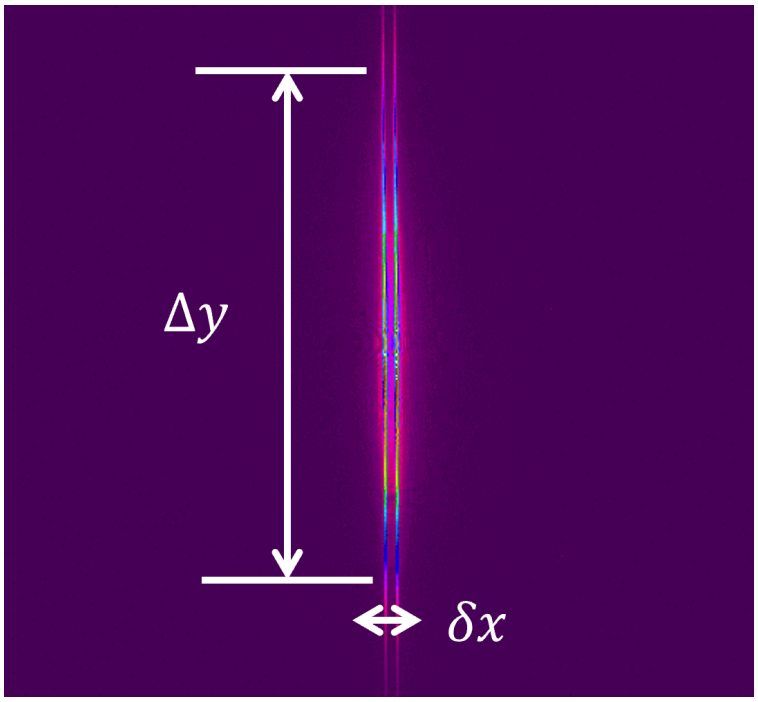
(b) FLDI system catch side

Figure 4.32: Schematic of the cylindrical lens FLDI system used to measure the flat plate boundary layer. The green labels are for the elements present in both lens configurations for the camera, while the blue labels highlight optic(s) that are either unique to the cylindrical lens system used in these experiments and the red label highlights the optic(s) used only in the spherical lens configuration.

In the cylindrical lens setup, the spherical lenses were swapped for identical focal length cylindrical lenses that were oriented in the streamwise direction to expand and focus the beam in a single direction while maintaining a constant wall normal height. Additionally, the DOE is removed and an $f = -25.4$ mm cylindrical lens and $f = 100$ mm cylindrical lens are placed between the first expansion lens and polarizer. The first of these lenses spreads the beam in the wall normal direction while the second collimates it in that direction. The two lenses are spaced 74.6 mm apart, yielding a collimated beam size approximately three times the laser output. Figure 4.33a shows an image of the spherical beams at the system focus, with the pair spacing (Δx) and beam spacing (δx) highlighted. Figure 4.34b shows the cylindrical system profile with the beam spacing and beam height (Δy) highlighted. A complete list of the relevant length values for each system are compiled in Table 4.5. The beam profile images were taken using a beam camera (Newport LBP2-VIS2) placed at the focus of the FLDI system. For the spherical system, the beam height and width are taken as the beam diameter and in the cylindrical case, the pair spacing is absent since only one measurement signal was taken for that case. The cylindrical lens configuration only had one measurement pair since the camera sensor was only large enough to encapsulate one signal while maintaining a sufficiently high frame rate. The height for the cylindrical lens signal is set to ensure a tall enough measurement area to capture the boundary layer and freestream while keeping the signal small enough to fit on the camera sensor. Additionally, the camera was operated at two frame rates. In both lens configurations, the camera frame rate was 1.008 MHz with resolutions of $512x8$ pixels for the spherical lens LA-FLDI and $384x16$ pixels for the cylindrical lens FLDI. The 1.008 MHz acquisition rate was the highest preset option for the camera that still allowed a reasonable sensor size. The narrow band of pixels allowed made the system susceptible to vibrations, with runs being re-done due to the signal moving off the sensor. This, combined with the flow fields studied, led to a reduction in the frame rate of the cylindrical lens system to 210 kHz. Screech tones in the jet would be low frequency enough to resolve and were not the focus of the study and the turbulent frequencies of the flat plate boundary layer was too high for the cylindrical lens megahertz acquisition to confidently resolve.



(a) Spherical lens



(b) Cylindrical lens

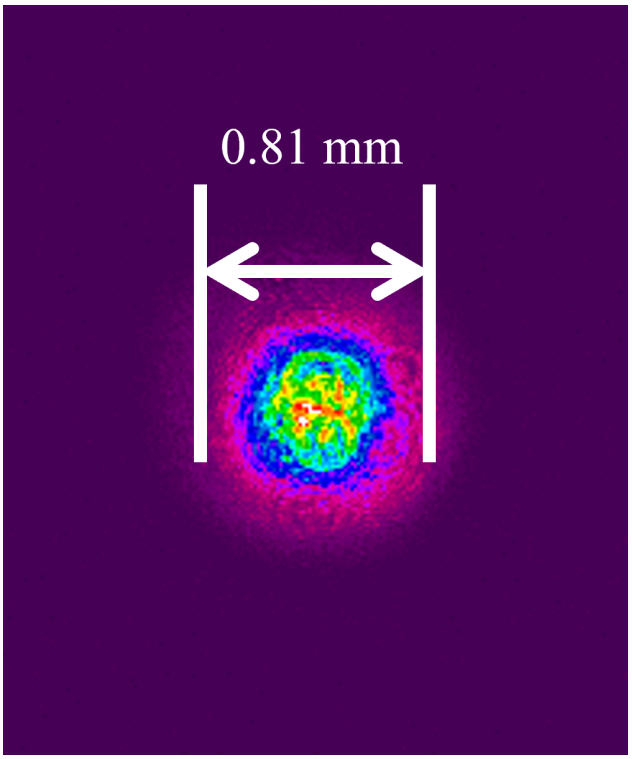
Figure 4.33: Beam profiles at the system focus for both lens configurations with relevant lengths labeled.

Table 4.8: Measurements of the beam profiles for both configurations

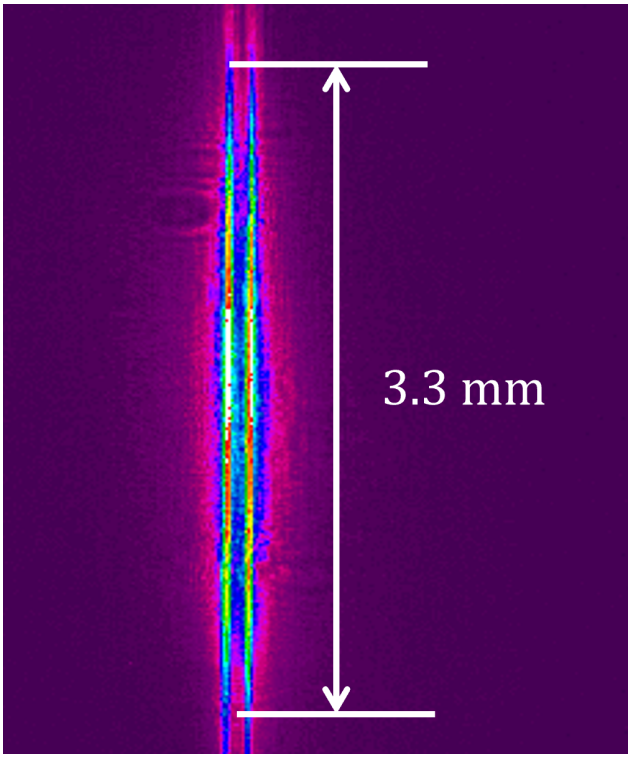
Length	Spherical	Cylindrical
Δx	4.0	N/A
δx	0.1	0.1
Δy	0.08	2.8
δy	0.08	0.08

To achieve a precise spatial measurement, the beam height must be accurately measured to ensure both collimation and accurate mapping on the camera. To do this, the output directly from the laser must be measured and the $1/e^2$ signal drop off for Gaussian beams must be considered. This same concept must be employed for the measurement at the focus and for the direct mapping onto the camera. Figure 4.34a shows the beam profile of the laser output having a $1/e^2$ diameter of 0.81 mm and Fig. 4.34b having a $1/e^2$ diameter of 3.30 mm, showing a magnification of 4.00 generated by the lens expansion optics compared to the theoretical magnification of 3.9. To ensure an accurate measurement, the profiles in Fig. 4.34 were taken with a shortened exposure time on the beam camera to ensure the signal was not over exposed. Using this measured height, the physical scaling of the camera signal can be determined from the size of the signal on the camera sensor. Since there is no expansion lens in front of the camera, the camera's pixel size ($20\mu m \times 20\mu m$) can be used to validate the signal size and collimation. The length of the signal on the camera is 167 px, highlighted by the red lines overlaid on the signal as it appears on the camera in Fig. 4.35a. Based on the physical pixel size, the resolution of the camera is 50 px/mm and dividing the signal length by this resolution yields a physical size of 3.34 mm, matching the beam measurement at the focus. This matching shows that the signal is not expanding through the test section and that the camera's designed resolution is appropriate to use as a conversion to physical units.

To ensure the camera had sufficient dynamic range, the second Wollaston prism was translated across the signal to change the signal phase from maximum to minimum. Figure 4.35b shows the camera response as the prism is shifted, with the mean camera intensities marked by black x's and those values fit with a sine wave. The camera had a 0.35 μs shutter and showed a sufficient dynamic response; however, it was important to optimize the neutral density filters, the 50/50 beam splitter, and the camera shutter to achieve an appropriate response. The use of too many ND filters or a short shutter time reduced the camera's minimum below that of the system, causing the signal to blend in with the background noise or disappear entirely before the system's minimum signal. Conversely, the extension of the shutter speed or reduction in the number of filters caused the camera to quickly overexpose, well before the maximum signal generated by the system.

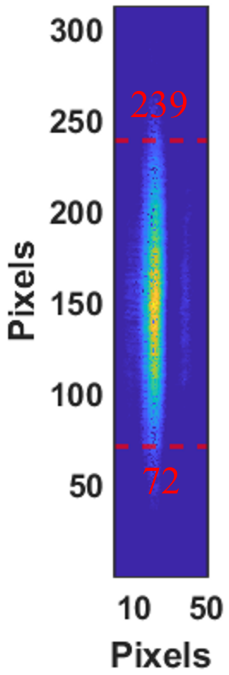


(a) Beam profile taken at the laser output

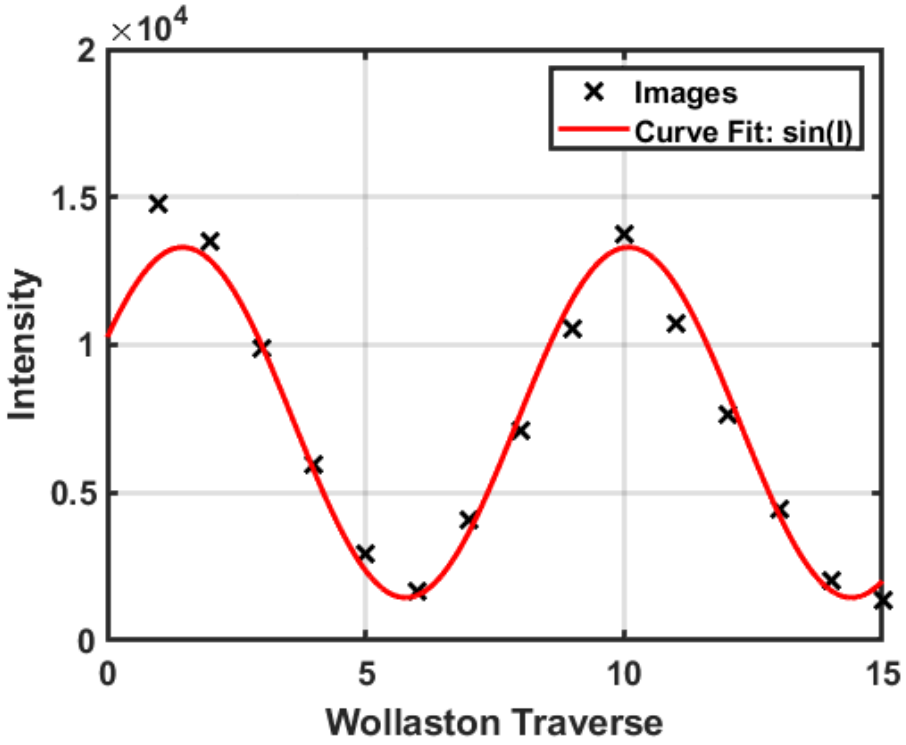


(b) Cylindrical lens profile at the focus

Figure 4.34: Beam profiles with accurate measurements using the $1/e^2$ beam diameter for Gaussian beams.



(a)



(b)

Figure 4.35: (a) cylindrical FLDI signal imaged by the camera. The $1/e^2$ extent of the beam was calculated in MATLAB and is highlighted in red. (b) mean intensity of the camera signal as the second Wollaston prism is translated across the beam path.

4.4.2 Results and Discussion

Tube Jet

To characterize the response of the cylindrical lens FLDI signal at discrete points along the length of the signal, a small tube jet was bisected by the FLDI signal at four locations downstream of the nozzle exit. For this setup, the camera was operated at 210 kHz to improve the sensor size of the camera, making alignment easier and eliminating signal dropout. To generate a uniform signal at each spanwise location, each row of pixels was summed together, creating a single column vector for each image, with each value representing an independent spatial measurement. Figures 4.36 through 4.39 show the normalized standard deviation of the FLDI signal at each location against the normalized standard deviation profiles from schlieren. The schlieren profiles are spanwise slices at the same axial locations as the FLDI measurements. The x/d location in Fig. 4.36 was the closest the signal could be placed to the nozzle without cutting off any of the FLDI signal. This was accomplished by cutting off the signal with the nozzle, then using a precision translation stage, moving the nozzle back until the entire signal was visible on the camera. There is good agreement between the profiles at all four locations, with the FLDI signal showing a slightly wider jet in Fig. 4.37 and Fig. 4.38. This discrepancy is due to FLDI having a higher sensitivity than schlieren. In Fig. 4.39 there is still good agreement between the two diagnostics, although there are not observable shear layer peaks. This lack of shear layer peaks is explained in Fig. 4.28b, showing the 1.0 x/d measurement location lies over the first shock cell in the jet, obscuring the shear layer seen prior to that interaction. The y-axis normalization of the standard deviation by its maximum compensates for the difference in pixel intensity between the two different diagnostic techniques, allowing for them to be compared directly with each other.

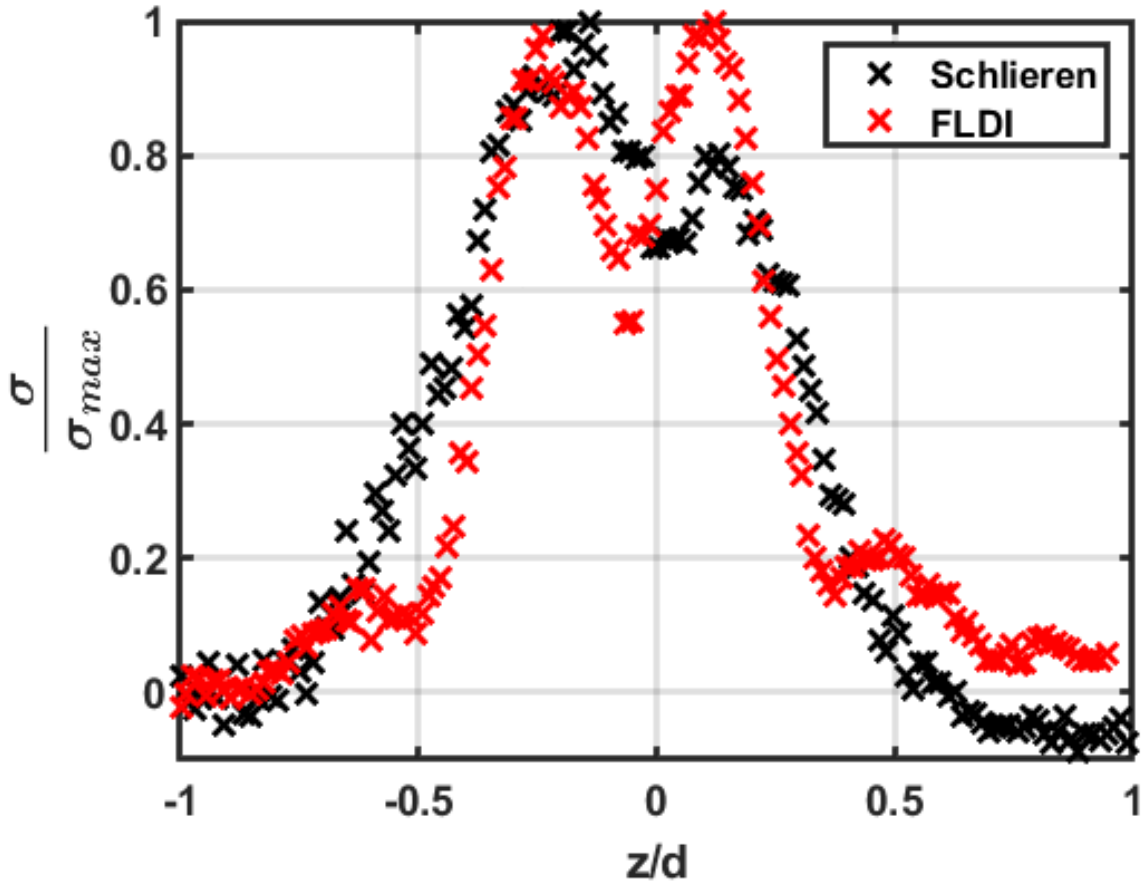


Figure 4.36: 0.0 x/d

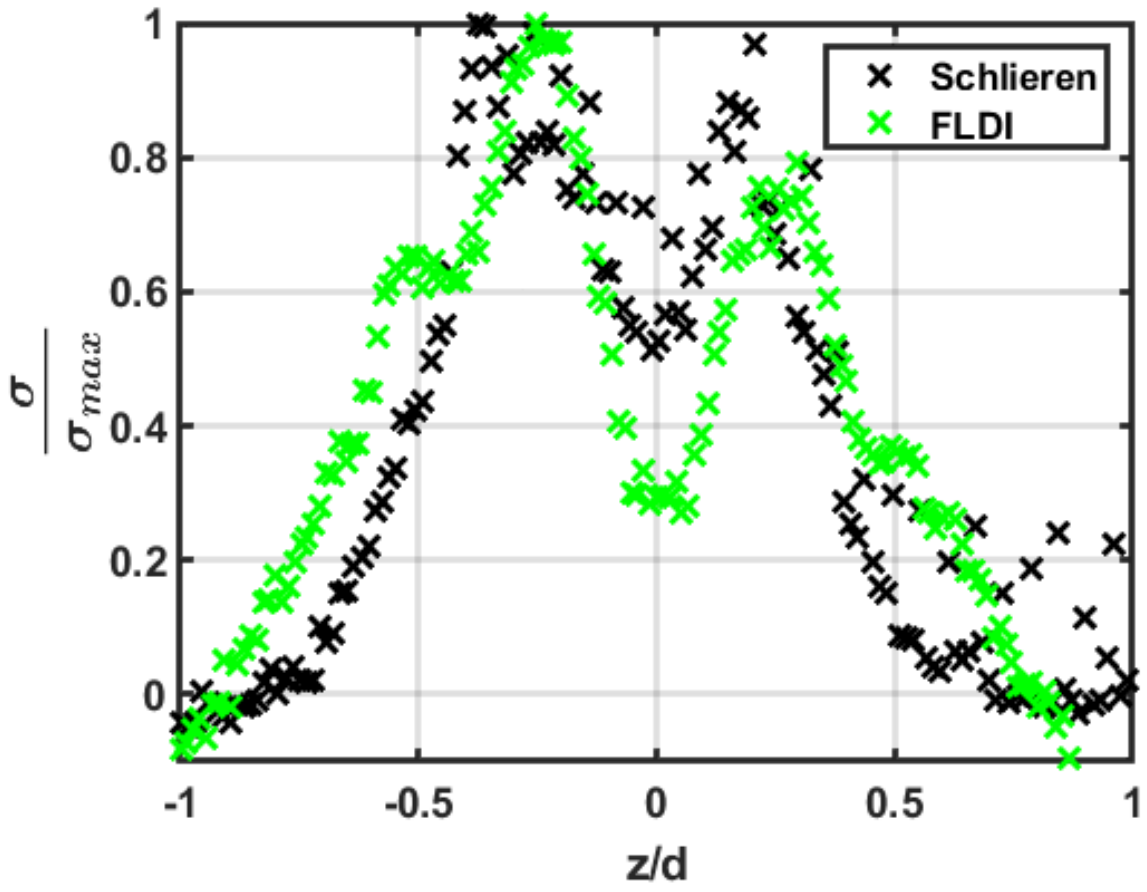


Figure 4.37: 0.3 x/d

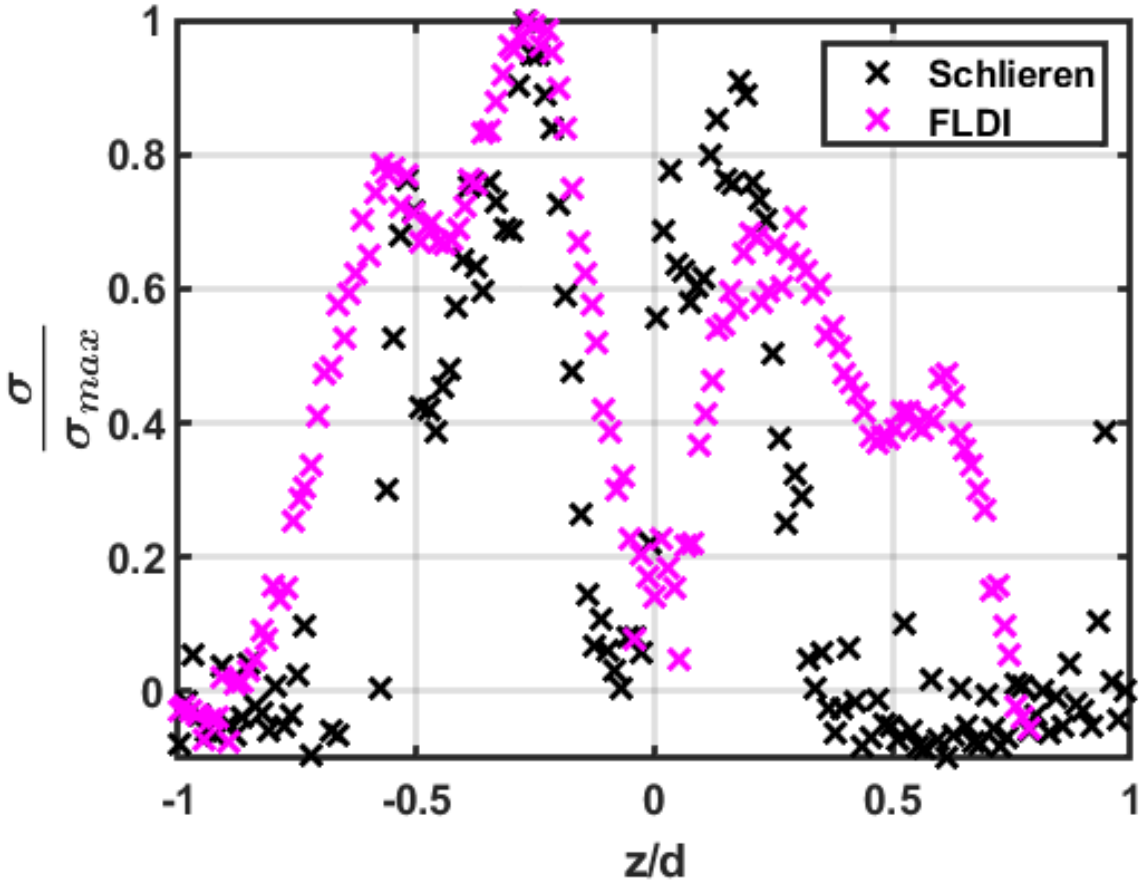


Figure 4.38: 0.6 x/d

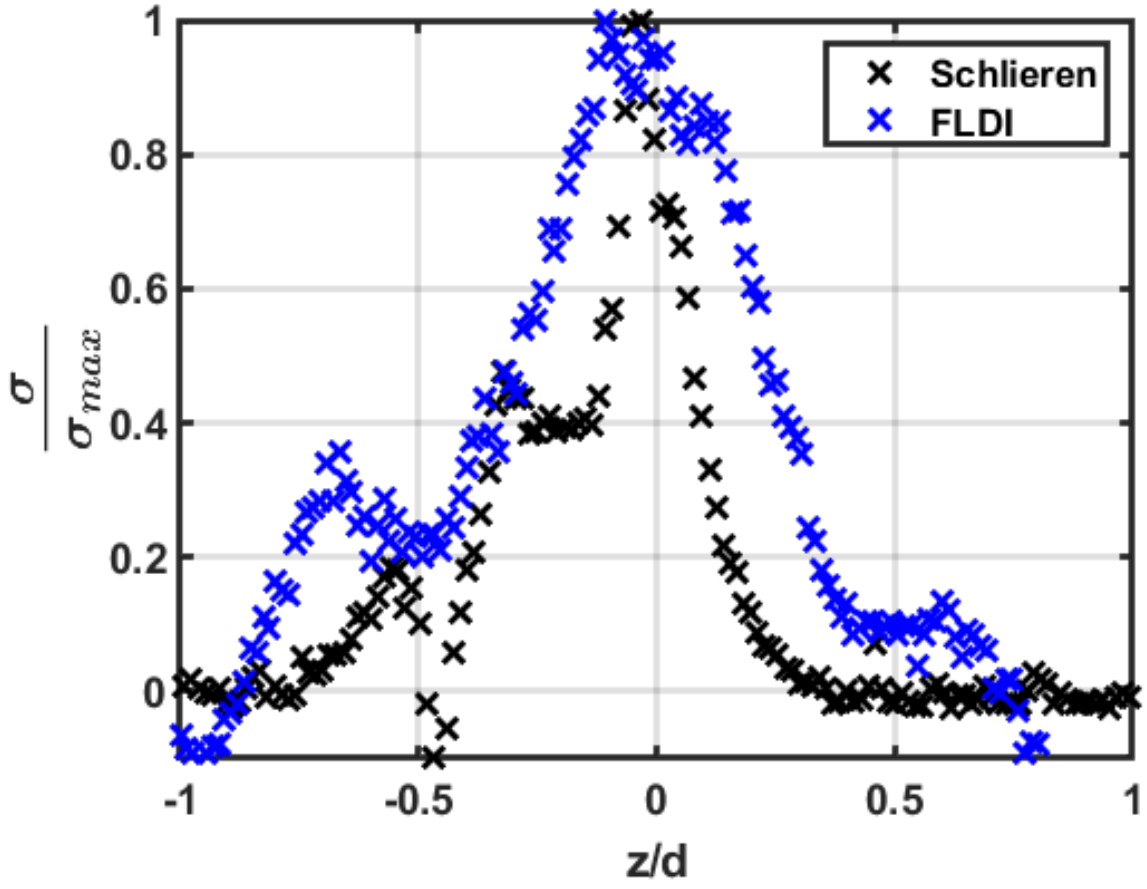


Figure 4.39: 1.0 x/d

Mach 2 Flat Plate

Given the success of resolving the small-scale jet flow, the system was moved to the UTSI Mach 2 wind tunnel to study its efficacy on a thin, turbulent boundary layer along a flat plate. Measurements were taken at 60 and 90 mm from the leading edge of the plate at three different Reynolds numbers tabulated in Section 2.2. Due to the low density environment of the wind tunnel, the response of the FLDI system was decreased as shown in the average intensity profiles for each condition in Fig. 4.40. The background signal was taken at atmospheric conditions with the tunnel not in operation and has the highest signal compared to the run conditions. Each run condition shows a subsequent decrease in signal with a decrease in static density, with condition 1 having the lowest signal of all. While the trend of decreasing intensity values is based on a decrease in the magnitude of density fluctuations, the actual intensity values are a function of the system setup and any correlation of those values to actual density is a subject for further exploration. Of particular interest to this study is the spatial variation in the signal, even in the background. This is a result of spreading the Gaussian distribution of the laser and the use of a cylindrical lens in spreading that signal in the wall normal direction. The standard deviation and RMS plots of these signals also show a similar spatial distribution except for the standard deviation of the background signal which is essentially zero across the entire signal as is expected. Due to the high-density nature of the tube jet, this issue was masked as the high density of the flow increased the signal intensity to a point where this distribution was negligible in comparison. This increase in signal for the jet did require the use of more neutral density filters to avoid overexposure of the camera sensor, generating far different intensity magnitudes between the jet and wind tunnel setup.

In the wind tunnel, a flat plate boundary layer was measured with the cylindrical signal oriented wall normal as shown in Fig. 4.29. The standard deviation profiles taken at these two locations is shown in Figures 4.43 through 4.45 for all three conditions. To account for the spatial distribution of the FLDI signal the standard deviation of each pixel was normalized by the mean of that pixel. This not only accounts for the spatial distribution of the signal but also the change in signal intensity brought about by the different static

densities at each condition. In both streamwise locations, the camera detection resolves the increased density fluctuations with increasing Reynolds number from Condition 1 to Condition 3, with Condition 3 having the highest values of the three, particularly in the freestream region toward the top of the signal. All the runs also show a peak in fluctuations in the lower portion of the signal before the fluctuations fall back towards the freestream values.

This reduction in fluctuations near the wall is consistent with known boundary layer theory, as the lowest portions of the turbulent boundary layer are known as the laminar sub-layer. FLDI measurements, particularly by Ceruzzi [103] and Weisberger [72], show that FLDI measurements in laminar boundary layers are similar to measurements made in freestream conditions. These profiles also correspond well with RMS profiles measured by Ceruzzi [103] and Davenport [104], who translated each of their systems through a turbulent wall boundary layer, measuring the signals at different wall normal locations. Davenport in particular, used the floor boundary layer of the same facility as this study; however, both researchers used spherical lens systems with photodiode detectors. Even with differing detectors, the RMS profiles they measured have a similar shape to those shown in Figures 4.43 through 4.45.

One point of interest between the different conditions is the increased wall normal position in the peak fluctuations in the boundary layer. The increasing wall normal heights of these peaks with Re/x runs counter intuitive to the shrinking of the known decrease in boundary layer thickness with an increase in Re/x. This trend is consistent between both positions and between different runs of the same conditions and is a current source of future investigation. Given the scale of this flow field, no PIV measurements have been done to directly measure the boundary layer thickness on this model to determine the actual boundary layer thickness at these locations and conditions. Even with this Reynolds number discrepancy, the change in boundary layer thickness is expected to be larger with the change in position compared to that of Re/x. Figures 4.43 through 4.45 compare the fluctuation profiles between the two streamwise locations at each condition. For each condition, the profile is shifted slightly higher for the 90 mm position relative to 60 mm, showing that the system resolved the boundary layer growth between the two positions. This shift is evident not only in the

increased wall normal height of the peak fluctuations, but also in the freestream asymptote occurring prior to a wall normal height of 2 mm at the upstream location and after 2 mm at the downstream location. There is also an increase in the magnitude of fluctuations in the downstream position, indicating an increase in turbulent energy as the flow develops.

Summary and Conclusions

Camera-based detection was used with both spherical and cylindrical lens FLDI systems. The camera-based detection was compared against the traditional photodiode detection of a spherical lens system, with reasonable agreement in spectral content and convective velocities. The differences between the two were most evident in the convective velocity measurements on the floor of the Mach 2 wind tunnel, where the limited sampling rate of the camera was unable to resolve the fine scale velocity changes in the upper regions of the boundary layer. When deployed with a cylindrical lens system, the camera's large sensor allowed for a discrete spatial sampling of the signal. Comparisons with high speed schlieren show the camera detection could accurately resolve the density changes of the small-scale jet and compared well with similar schlieren measurements. This system was then deployed to the UTSI Mach 2 wind tunnel where it made highly resolved measurements of the thin, turbulent boundary layer along a flat plate. With a high pixel to millimeter resolution, the system was able to resolve fluctuations from the freestream to the near wall, laminar sub-layer. The high resolution of camera-based detection combined with the benefits of cylindrical lens FLDI has immense potential for allowing near wall, non-intrusive boundary layer measurements.

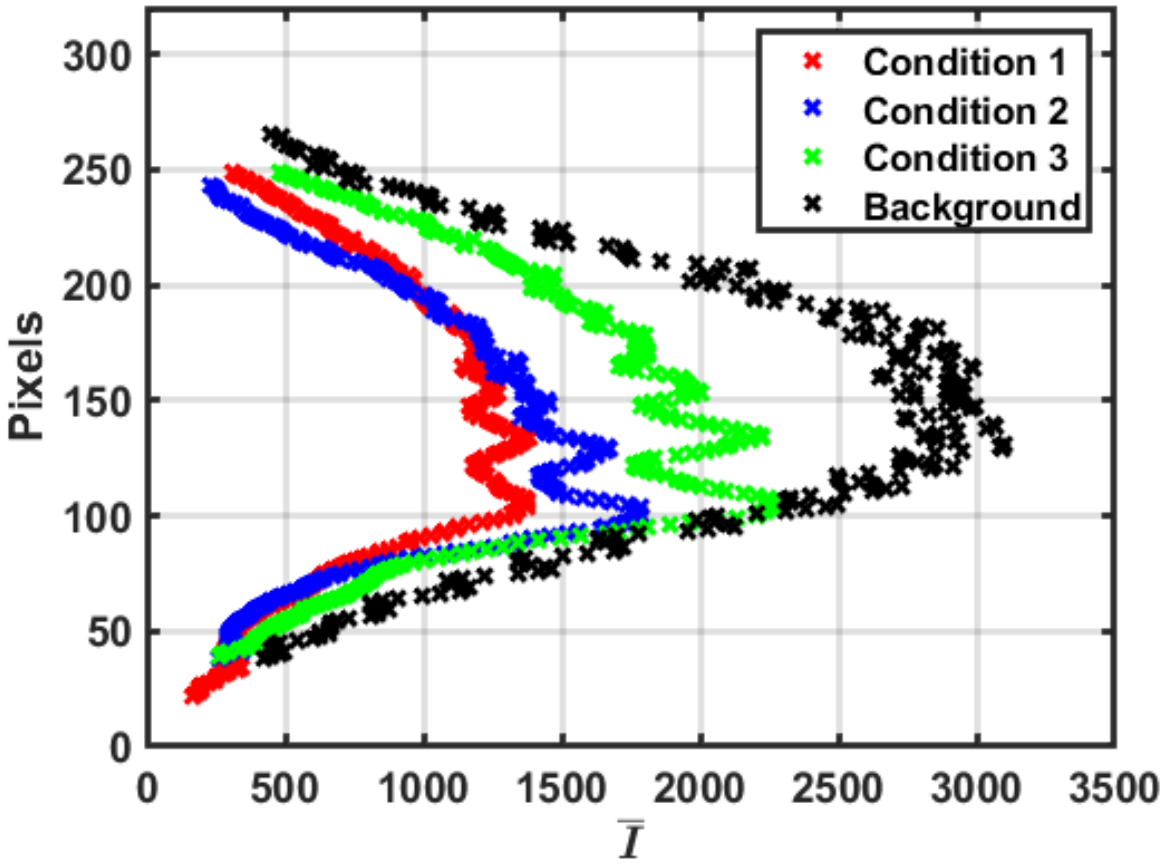


Figure 4.40: Average intensity of each row of pixels

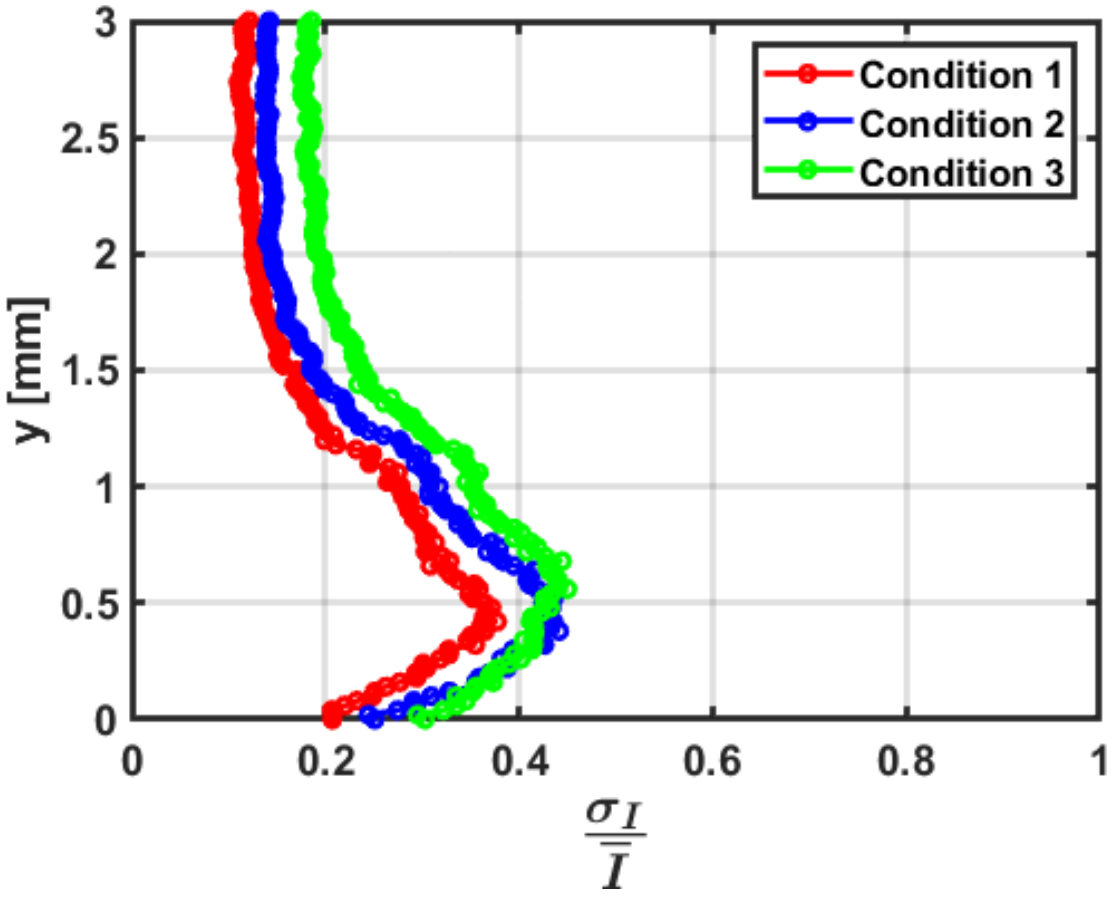


Figure 4.41: Normalized FLDI signal at x = 60 mm.

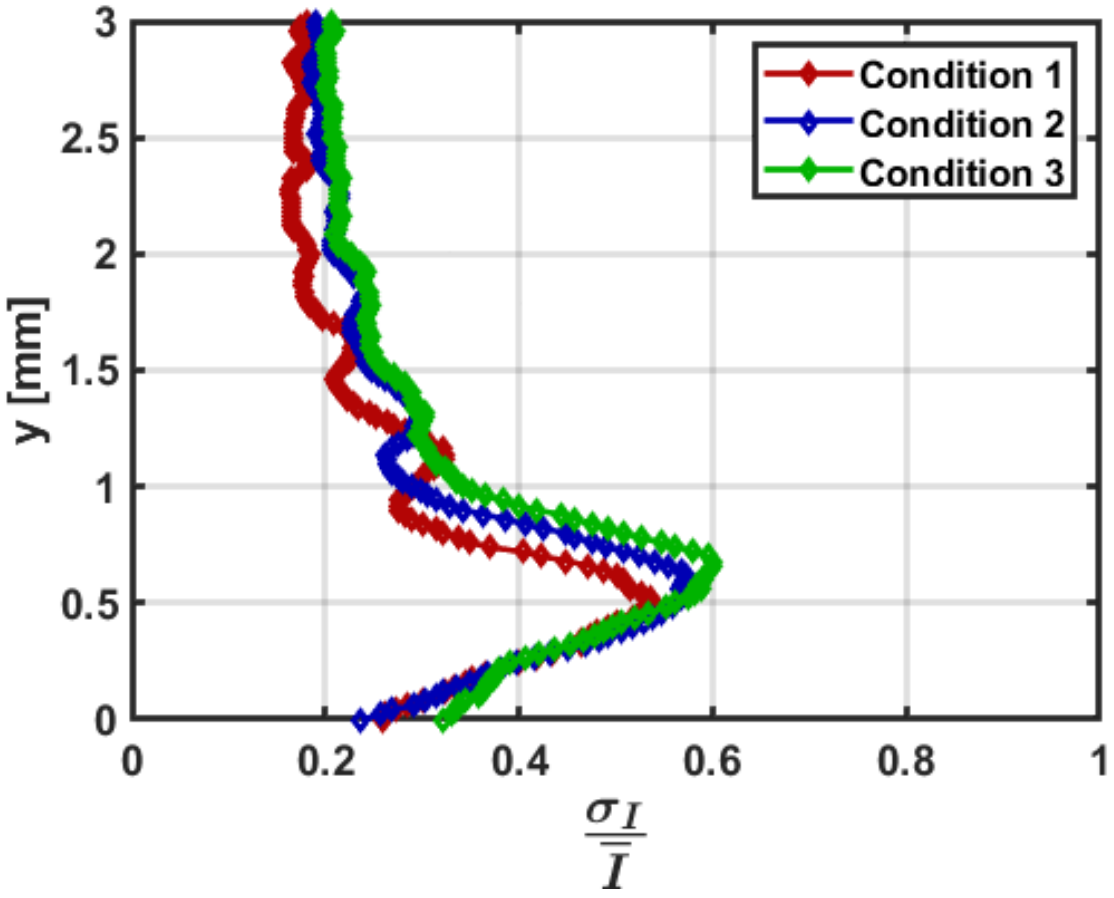


Figure 4.42: Normalized FLDI signal at x = 90 mm.

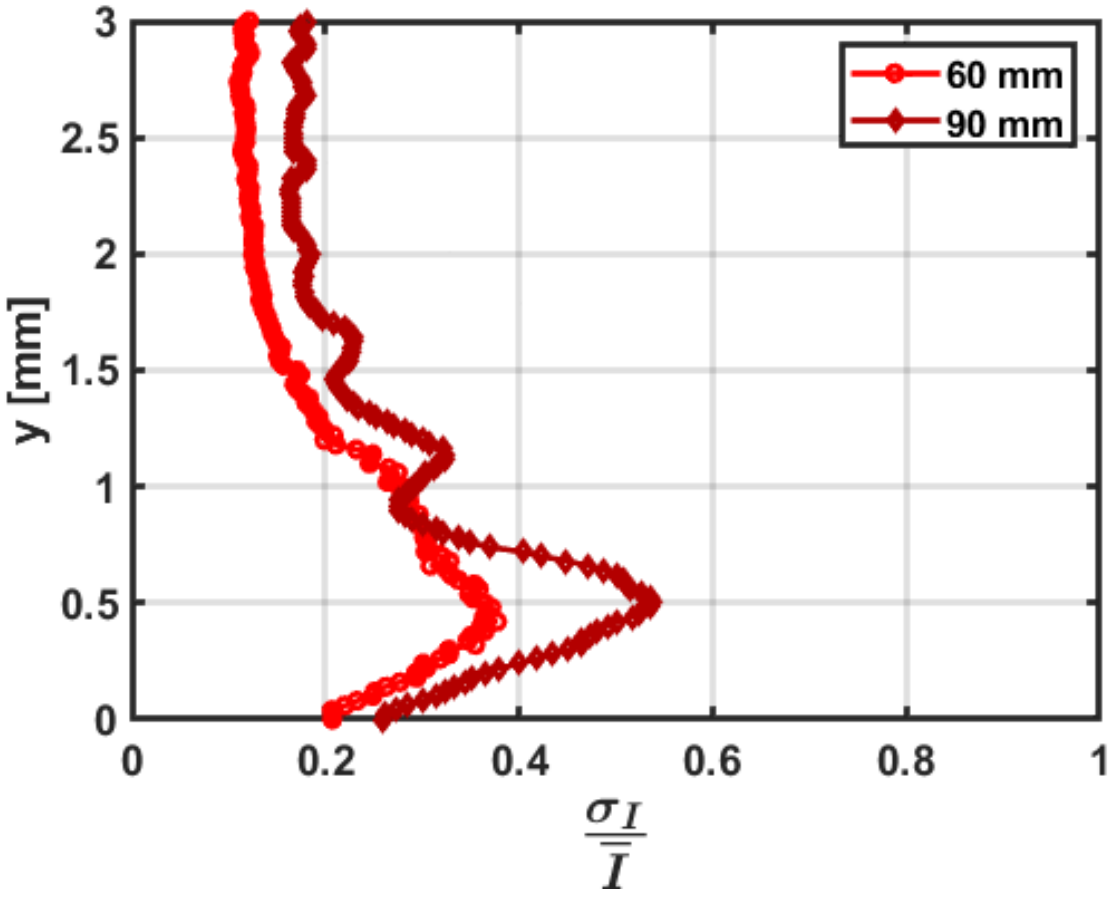


Figure 4.43: Normalized fluctuation profiles at both x locations for Condition 1

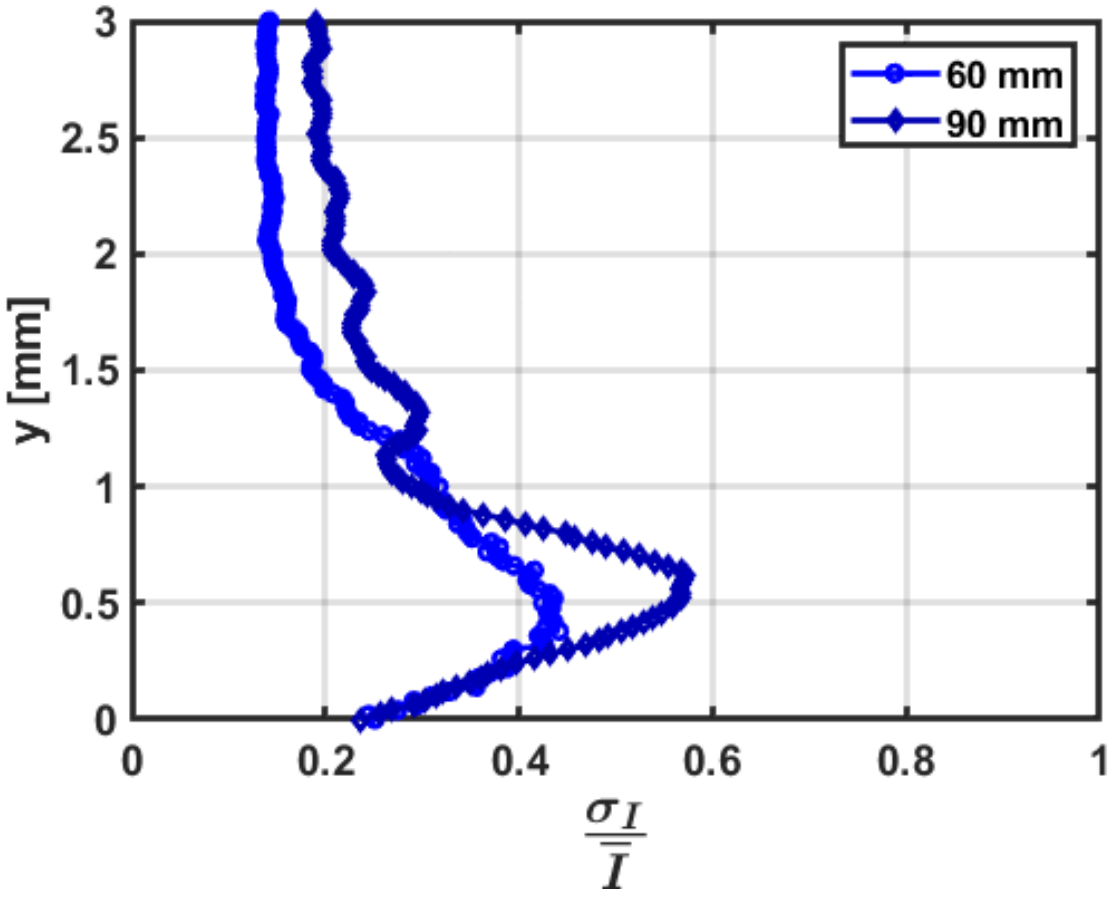


Figure 4.44: Normalized fluctuation profiles at both x locations for Condition 2

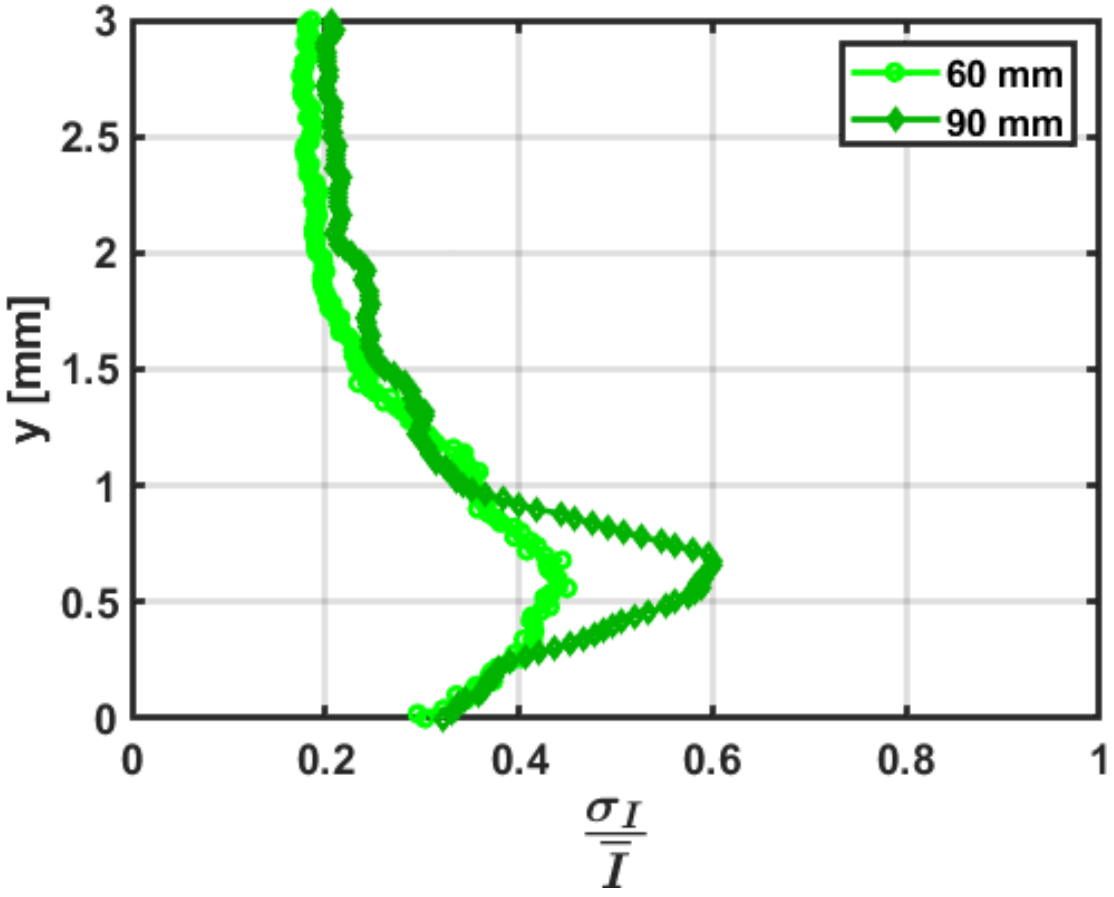


Figure 4.45: Normalized fluctuation profiles at both x locations for Condition 3

Chapter 5

Future Research

Future research efforts on the aerodynamic impact of fluid structure interactions should initially focus on completing the experimental suite on the Mach 7 flare. Pressure sensitive paint would be used to corroborate the flow structures and interaction changes identified in the temperature and schlieren measurements. A direct shear stress sensor and appropriate velocimetry technique would measure the changes in skin friction along the flare while also identifying where the Reynolds analogy holds and if the interaction deviates from that relationship. Further work should focus on changes to the canonical control surface by changing it to a fin and looking at the impact of incoming boundary layer state. Future diagnostic work would push forward the measurement capability of FLDI while facilitating its deployment to a broader array of wind tunnels. Current efforts from other researchers look to use FLDI as a continuous measurement for characterizing freestream turbulent noise content along with being a constant transition detector along complex model surfaces. Improvements in camera and detector technology would allow for a combination of boundary layer RMS measurements and convective velocity profiles, giving researchers a highly resolved measurement tool for future boundary layer studies.

Bibliography

[1] Bertin, J. J., *Hypersonic aerothermodynamics*, AIAA, 1994. 1, 11

[2] Howarth, L., "High Speed Aerodynamics and Jet Propulsion. Volume VI. General Theory of High Speed Aerodynamics. Edited by WR Sears. Oxford University Press, 1955. 758 pp. Diagrams. 100s." *The Aeronautical Journal*, Vol. 59, No. 536, 1955, pp. 576–577. 2

[3] Roshko, A., and Liepmann, H., *Elements of Gas-dynamics*, Wiley, 1957. 2, 50

[4] Roger, M., "Aerothermalelasticity," *Aero/Space Engineering*, Vol. 17, 1958, pp. 34–43. 3, 33

[5] Roger, K., "Boundary-Layer Theory for Pressure and Drag of a Wavy Surface," *Journal Aircraft*, Vol. 11, 1974, pp. 382–389. https://doi.org/10.2514/3.60353. 3, 4

[6] Anderson, W. J., "Supersonic Wind-Tunnel Tests of Wavy-Walled Cylinders," *AIAA Journal*, Vol. 5, 1967. 4, 5, 9, 33, 39

[7] Dixon, S., Griffith, G., and Shore, C., "Experimetnal Pressures and Turbulent Heat-Transfer Coefficients Associated with Sinusoidal Protuberances on a Flat Plate at a Mach Number of 3," Tech. rep., 1963. 4

[8] Lynch, K. P., Jones, E. M., and Wagner, J. L., "Simulatneous PSP and DIC measurements for fluid-structure interactions in a shock tube," *AIAA Aviation 2018 Forum*, 2018. https://doi.org/10.2514/6.2018-3870. 6

[9] Lynch, K. P., Jones, E. M., Brink, A. R., Rohe, D. P., Kuether, R. J., Wagner, J. L., Mathis, A., and Quinn, D. D., "Response of Jointed-Structures in a Shock Tube: Simultaneous PSP an dDIC with Comparison to Modeling," *AIAA Aviation 2019 Forum*, 2019. https://doi.org/10.2514/6.2019-3654. 6

[10] Tan, S. S., Gramola, M., and Bruce, P. J., "Fluid-Structure Interactions on a Slender Cone under Quiet Flow Conditions at Mach 6," *AIAA Scitech 2017 Forum*, 2017. https://doi.org/10.2514/6.2017-0402. 6, 7

[11] Gramola, M., Bruce, P., and Santer, M., "Experimental FSI study of adaptive shock control bumps," *Journal of Fluids and Structures*, Vol. 81, 2018, pp. 361–377. 6, 7

[12] Tan, S. S., Gramola, M., and Bruce, P. J., "Oblique Shockwave Boundary Layer Interaction on a Flexible Surface," *AIAA Scitech 2019 Forum*, 2019. https://doi.org/10.2514/6.2019-0097. 6

[13] Neet, M. C., and Austin, J. M., "Effects of Surface Compliance on Shock Boundary Layer Interactions in the Caltech Mach 4 Ludwieg Tube," *AIAA Scitech 2020 Forum*, 2020. https://doi.org/10.2514/6.2020-0816. 6, 7

[14] Spottswood, S. M., Beberniss, T. J., and Eason, T. G., "Full-field, dynamic pressure and displacement measurements of a panel excited by shock-boundary layer interaction," *AIAA/CEAS Aeroacoustics 2013*, 2013. https://doi.org/10.2514/6.2013-2016. 7

[15] Beberniss, T. J., Spottswood, S. M., Ehrhardt, D. A., and Perez, R., "Dynamic Response of a Thin Panel Subjected to a Shock Wave Impingement and Thermal Buckling," *AIAA 2017 Aviation Forum*, 2017. https://doi.org/10.2514/6.2017-3555. 7

[16] Spottswood, S., Eason, T., and Beberniss, T., "Influence of shock-boundary layer interactions on the dynamic response of a flexible panel," *Proceedings of the ISMA-2012*, 2012, pp. 17–19. 7

[17] Beberniss, T. J., and Eason, T. I., "Structural Scale Modeling and Experiments for Hypersonic Vehicles," Tech. rep., Hypersonic Sciences Branch (AFRL/RQHF) Wright-Patterson Air Force Base . . . , 2017. 7

[18] Peltier, S. J., Rice, B. E., Szmodis, J. M., Ogg, D. R., Hofferth, J. W., Sellers, M. E., and Harris, A., "Aerodynamic Response to a Compliant Panel in Mach 4 Flow," *AIAA Aviation 2019 Forum*, 2019. https://doi.org/10.2514/6.2019-3541. 7, 8, 9

[19] Visbal, M., "Viscous and Inviscid interactions of an oblique shock with a flexible panel," *Journal of Fluids and Structures*, Vol. 48, 2014, pp. 27–45. 7

[20] Boyer, N. R., McNamara, J. J., and Visbal, M. R., "Study on Shock-Induced Panel Flutter in 2-D Laminar Flow," *AIAA Aviation 2016 Forum*, 2016. https://doi.org/10.2514/6.2016-1091. 7, 8, 9

[21] Brouwer, K. R., Gogulapati, A., and McNamara, J. J., "Interplay of Surface Deformation and Shock-Induced Separation in Shock/Boundary Layer Interactions," *AIAA Scitech 2017 Forum*, 2017. https://doi.org/10.2514/6.2017-0177. 8

[22] Shinde, V., McNamara, J., Gaitonde, D., Barnes, C., and Visbal, M., "Transitional shock wave boundary layer interaction over a flexible panel," *Journal of Fluids and Structures*, Vol. 90, 2019, pp. 263–285. 8

[23] Anderson, W. J., "Oscillatory Pressures in an Idealized Boundary Layer with an Application to the Panel Flutter of Cylindrical Shells," *AIAA Journal*, 1965. https://doi.org/10.2514/6.1965-1105. 8, 39

[24] Shinde, V., Becks, A., Deshmukh, R., McNamara, J., Gaitonde, D., Neet, M., and Austin, J., "Spatially developing supersonic turbulent boundary layer subjected to static surface deformations," *European Journal of Mechanics*, Vol. 89, 2021, pp. 485–500. 8, 9, 39

[25] Edney, B., "Anomalous heat transfer and pressure distributions on blunt bodies at hypersonic speeds in the presence of an impinging shock." Tech. rep., Flygtekniska Forsoksanstalten, Stockholm (Sweden), 1968. 9

[26] Edney, B. E., "Effects of shock impingement on the heat transfer around blunt bodies." *AIAA Journal*, Vol. 6, No. 1, 1968, pp. 15–21. 9

[27] Holden, M., Moselle, J., Wieting, A., and Glass, C., "Studies of aerothermal loads generated in regions of shock/shock interaction in hypersonic flow," *26th Aerospace Sciences Meeting*, 1988, p. 477. 9, 10

[28] Bertin, J. J., Graumann, B. W., and Goodrich, W. D., "Aerothermodynamic Aspects of Shock-Interference Patterns for Shuttle Configurations During Entry," *Journal of Spacecraft and Rockets*, Vol. 10, No. 9, 1973, pp. 545–546. 11

[29] Holden, M., and Kolly, J., "Measurements of heating in regions of shock/shock interaction in hypersonic flow," *33rd Aerospace Sciences Meeting and Exhibit*, 1995, p. 640. 11

[30] Keyes, J. W., and Hains, F. D., "Analytical and experimental studies of shock interference heating in hypersonic flows," Tech. rep., 1973. 11

[31] Berry, S. A., and Nowak, R. J., "Fin leading-edge sweep effect on shock-shock interaction at Mach 6," *Journal of spacecraft and rockets*, Vol. 34, No. 4, 1997, pp. 416–425. 11

[32] Klopfer, G., and Yee, H., "Viscous hypersonic shock-on-shock interaction on blunt cowl lips," *26th Aerospace Sciences Meeting*, 1988, p. 233. 11

[33] COMEAUX, K., CHAPMAN, D., and MACCORMACK, R., "Viscous hypersonic shock-shock interaction on a blunt body at high altitude," *28th Thermophysics Conference*, 1993, p. 2722. 11

[34] Hackett, C., and Calleja, J., "Exploratory study of heating due to a hypersonic, high-enthalpy shock/shock interaction," *Fluid Dynamics Conference*, 1995, p. 2216. 11

[35] Smeets, G., "Flow Diagnostics by Laser Interferometry," *IEEE Transactions on Aerospace and Electronic Systems*, Vol. AES-13, No. 2, 1977, pp. 82–90. https://doi.org/10.1109/TAES.1977.308441. 12, 27

[36] Lester, L., and Gragston, M., "10 kHz Laser-Induced Schliere Anemometry for Velocity, Mach Number, and Static Temperature Measurements in Supersonic Flows," *Applied Optics*, Vol. 60, No. 5, 2021. https://doi.org/0.1364/AO.433085. 12, 23

[37] Schmisseur, J. D., Collicott, S. H., and Schneider, S. P., "Laser-Generated Localized Freestream Perturbations in Supersonic and Hypersonic Flows," *AIAA Journal*, Vol. 38, No. 4, 2000, pp. 666–671. https://doi.org/10.2514/2.1008. 12, 24

[38] Smeets, G., and George, A., "Laser-Differential Interferometer Applications in Gas Dynamics," Tech. rep., Institut Franco-Allemand De Recherches Saint-Louis(France), 1996. 12, 27

[39] White, F. M., and Majdalani, J., *Viscous fluid flow*, Vol. 3, McGraw-Hill New York, 2006. 12

[40] Price, T. J., Gragston, M., Schmisseur, J. D., and Kreth, P. A., "Measurement of supersonic jet screech with focused laser differential interferometry," *Applied Optics*, Vol. 59, No. 28, 2020, pp. 8902–8908. 12

[41] Gragston, M., Siddiqui, F., and Schmisseur, J. D., "Detection of second-mode instabilities on a flared cone in Mach 6 quiet flow with linear array focused laser differential interferometry," *Experiments in Fluids*, Vol. 62, No. 4, 2021, 81. https://doi.org/10.1007/s00348-021-03188-6. 12, 13, 28

[42] Ceruzzi, A., McManamen, B., and Cadou, C. P., "Demonstration of two-point focused laser differential interferometry (2pFLDI) in a Mach 18 flow," *AIAA Scitech 2021 Forum*, 2021, p. 0983. 12, 13

[43] Fulghum, M. R., "Turbulence Measurements in High-Speed Wind Tunnels Using Focusing Laser Differential Interferometry," , 2014. 12

[44] Ceruzzi, A., and Cadou, C. P., "Simultaneous Velocity and Density Gradient Measurements using Two-Point Focused Laser Differential Interferometry," *AIAA Scitech 2019 Forum*, 2019. https://doi.org/10.2514/6.2019-2295. 13, 28

[45] White, F. M., and Majdalani, J., *Viscous fluid flow*, Vol. 3, McGraw-Hill New York, 2006. 13

[46] Parziale, N. J., Shepherd, J. E., and Hornung, H. G., "Observations of Hypervelocity Boundary-Layer Instability," *Journal of Fluid Mechanics*, Vol. 781, 2015, p. 87–112. https://doi.org/10.1017/jfm.2015.489. 13

[47] Bathel, B. F., Weisberger, J. M., Herring, G. C., King, R. A., Jones, S. B., Kennedy, R. E., and Laurence, S. J., "Two-Point, Parallel-Beam focused Laser Differential Interferometry with a Nomarski Prism," *Appl. Opt.*, Vol. 59, No. 2, 2020, pp. 244–252. https://doi.org/10.1364/AO.59.000244. 13

[48] Jewell, J. S., Parziale, N. J., Lam, K.-L., Hagen, B. J., and Kimmel, R. L., "Disturbance and Phase Speed Measurements for Shock Tubes and Hypersonic Boundary-Layer Instability," *32nd AIAA Aerodynamic Measurement Technology and Ground Testing Conference*, 2016. https://doi.org/10.2514/6.2016-3112. 13

[49] Gragston, M., Hsu, P., Jiang, N., Roy, S., and Zhang, Z., "Emissions in short-gated ns/ps/fs-LIBS for fuel-to-air ratio measurements in methane-air flames," *Applied Optics*, Vol. 60, No. 15, 2021, pp. C114–C120. 13

[50] Houpt, A., and Leonov, S., "Cylindrical Focused Laser Differential Interferometer," *AIAA Journal*, Vol. 59, No. 4, 2021, pp. 1142–1150. https://doi.org/10.2514/1.J059750. 13, 28, 98

[51] Kreth, P. A., Gragston, M. T., Davenport, K., and Schmisseur, J. D., "Design and intial characterization of the UTSI Mach 4 Ludwieg tube," *AIAA Scitech 2021 Forum*, 2021. 16

[52] Gragston, M., Davenport, K., Siddiqui, F., Webber, N., Smith, C. D., Kreth, P. A., and Schmisseur, J. D., "Design and Initial Characterization of the UTSI Mach 7 Ludwieg Tube," *AIAA SCITECH 2023 Forum*, 2023, p. 1457. 16, 20

[53] Settles, G. S., *Schlieren and shadowgraph techniques: visualizing phenomena in transparent media*, Springer Science & Business Media, 2001. 23

[54] Combs, C. S., Lash, E. L., Kreth, P. A., and Schmisseur, J. D., "Investigating unsteady dynamics of cylinder-induced shock-wave/transitional boundary-layer interactions," *AIAA journal*, Vol. 56, No. 4, 2018, pp. 1588–1599. 23

[55] Lash, E. L., Combs, C. S., Kreth, P. A., Beckman, E. A., and Schmisseur, J. D., "Developing an Image-Based Analysis of the Dynamics of Transitional Shock Wave-Boundary Layer Interactions," *32nd AIAA Aerodynamic Measurement Technology and Ground Testing Conference*, 2016, p. 4320. 23

[56] Lash, E. L., Combs, C. S., Kreth, P. A., and Schmisseur, J. D., "Study of the dynamics of transitional shock wave-boundary layer interactions using optical diagnostics," *47th AIAA Fluid Dynamics Conference*, 2017, p. 3123. 23

[57] Chism, J. R., Gragston, M., Hagen, B., Leicht, J., and Riley, Z. B., "Laser-induced schliere anemometry in a Mach 6 flow with collinear light entry," *Applied Optics*, Vol. 61, No. 11, 2022, pp. 3070–3076. 23

[58] McLachlan, B. G., and Bell, J. H., "Pressure-sensitive paint in aerodynamic testing," *Experimental thermal and fluid science*, Vol. 10, No. 4, 1995, pp. 470–485. 24

[59] Campbell, B., Liu, T., and Sullivan, J., "Temperature sensitive fluorescent paint systems," *25th Plasmadynamics and Lasers Conference*, 1994, p. 2483. 24

[60] ISSI, "Innovative Scientific Solutions Inc. Website: Fast Response Pressure Sensitive Paint," , 2023. URL https://innssi.com/fastpsp.html. 25

[61] Gregory, J. W., Sakaue, H., Liu, T., and Sullivan, J. P., "Fast pressure-sensitive paint for flow and acoustic diagnostics," *Annual Review of Fluid Mechanics*, Vol. 46, 2014, pp. 303–330. 25, 30

[62] Sellers, M., Nelson, M., and Crafton, J. W., "Dynamic pressure-sensitive paint demonstration in AEDC propulsion wind tunnel 16T," *54th AIAA Aerospace Sciences Meeting*, 2016, p. 1146. 25

[63] Sellers, M., "Application of pressure sensitive paint for determining aerodynamic loads on a scale model of the F-16C," *21st aerodynamic measurement technology and ground testing conference*, 2000, p. 2528. 25

[64] Schultz, D. L., and Jones, T., "Heat-transfer measurements in short-duration hypersonic facilities," Tech. rep., ADVISORY GROUP FOR AEROSPACE RESEARCH AND DEVELOPMENT NEUILLY-SUR-SEINE ..., 1973. 27

[65] Smith, C., Kreth, P. A., Schmisseur, J. D., and Strickland, G., "Characterization of Temperature Sensitive Paint for Application in Hypersonic Ludwieg Tubes at the University of Tennessee," *AIAA SCITECH 2022 Forum*, 2022, p. 1660. 27, 31

[66] Beck, W. H., Klein, C., Henne, U., Martinez Schramm, J., Wagner, A., Hannemann, K., Gawehn, T., and Guelhan, A., "Application of temperature and pressure sensitive paints to DLR hypersonic facilities:"lessons learned"," *53rd AIAA Aerospace Sciences Meeting*, 2015, p. 0023. 27

[67] Martinez Schramm, J., Hannemann, K., Ozawa, H., Beck, W., and Klein, C., "Development of Temperature Sensitive Paints in the High Enthalpy Shock Tunnel Göttingen, HEG," 2015. 27

[68] Liu, T., Ward, C. A., Rubal, J., Sullivan, J. P., and Schneider, S. P., "Heat-flux measurements with temperature-sensitive paint in a Mach-6 quiet tunnel," *Journal of spacecraft and rockets*, Vol. 50, No. 2, 2013, pp. 282–293. 27

[69] Gragston, M., Price, T., Davenport, K., Zhang, Z., and Schmisseur, J. D., "Linear Array Focused-Laser Differential Interferometry for Single-Shot Multi-Point Flow Disturbance Measurements," *Opt. Lett.*, Vol. 46, No. 1, 2021, pp. 154–157. https://doi.org/10.1364/OL.412495. 28

[70] Gragston, M., Price, T. J., Davenport, K., Schmisseur, J. D., and Zhang, Z., "An m by n FLDI Array for Single-Shot Multipoint Disturbance Measurements in High-Speed Flows," *AIAA Scitech 2021 Forum*, 2021. https://doi.org/10.2514/6.2021-0599. 28, 99

[71] Chism, J. R., Gragston, M. T., Riley, Z., Spottswood, M., Perez, R., and Hagen, B. J., "Cylindrical and Spherical Lens Linear-Array Focused Laser Differential Interferometry on a Flat Plate at Mach 6," *AIAA Scitech 2022 Forum*, 2022. https://doi.org/10.2514/6.2022-1659. 28

[72] Weisberger, J. M., Bathel, B. F., Herring, G. C., Buck, G. M., Jones, S. B., and Cavone, A. A., "Multi-point line focused laser differential interferometer for high-speed flow fluctuation measurements," *Appl. Opt.*, Vol. 59, No. 35, 2020, pp. 11180–11195. https://doi.org/10.1364/AO.411006. 28, 138

[73] Peltier, S. J., Rice, B. E., Johnson, E., Narayanaswamy, V., and Sellers, M. E., "Effects of Three-Dimensional Pressure Gradients on High-Speed Turbulent Boundary Layers," *AIAA Scitech 2021 Forum*, 2021. https://doi.org/10.2514/6.2021-0913. 33

[74] Bertram, M., Weinstein, L., Cary, A., and Arrington, J., "Heat Transfer to Wavy Wall in Hypersonic Flow," *AIAA Journal*, Vol. 5, 1967, pp. 1760–1767. https://doi.org/10.2514/3.4301. 33

[75] Sun, C., and Childs, M. E., "A Modified Wall Wake Velocity Profile for Turbulent Compressible BOundary Layers," *Aircraft*, 1973. 46, 110

[76] Semper, M. T., and Bowersox, R. D., "Tripping of a hypersonic low-Reynolds-number boundary layer," *AIAA Journal*, Vol. 55, No. 3, 2017, pp. 808–817. 54

[77] Chism, J. R., Kreth, P. A., and Schmisseur, J. D., "Characterization of Downstream Effects from a WavyWall on a Hollow Cylinder at Mach 4," *AIAA SCITECH 2023 Forum*, 2023, p. 0080. 54

[78] Smith, C. D., Kreth, P. A., Schmisseur, J. D., and Strickland, G., "Temperature-Sensitive Paint Measurements of Cylinder-Induced Shockwave-Boundary Layer Interaction on a 6-degree Cone with Laminar Mach 7 Flow," *AIAA SCITECH 2023 Forum*, 2023, p. 2445. 55, 62

[79] Butera, J. G., Smith, C. D., and Schmisseur, J. D., "Hypersonic Ground Tests of BOLT II Using Optical Diagnostics," *AIAA SCITECH 2023 Forum*, 2023, p. 1190. 55

[80] Martinez Schramm, J., Hannemann, K., Ozawa, H., Beck, W., and Klein, C., "Development of Temperature Sensitive Paints in the High Enthalpy Shock Tunnel Göttingen, HEG," 2015. 55

[81] Liu, T., Ward, C. A., Rubal, J., Sullivan, J. P., and Schneider, S. P., "Heat-flux measurements with temperature-sensitive paint in a Mach-6 quiet tunnel," *Journal of spacecraft and rockets*, Vol. 50, No. 2, 2013, pp. 282–293. 60

[82] Nakakita, K., Osafune, T., and Asai, K., "Global heat transfer measurement in a hypersonic shock tunnel using temperature-sensitive paint," *41st Aerospace Sciences Meeting and Exhibit*, 2003, p. 743. 60

[83] Ledbetter, S. Y., Lester, L. E., Garner, A. N., Goldston, H. R., Smith, C. D., Gragston, M., Kreth, P. A., and Schmisseur, J. D., "Analysis of Streamwise Vortex Streaks in Shockwave-Boundary Layer Interactions on a Hollow Cylinder-Flare at M= 4," *AIAA AVIATION 2023 Forum*, 2023, p. 3698. 62

[84] Chism, J. R., Gragston, M., Hagen, B., Leicht, J., and Riley, Z. B., "Laser-induced schliere anemometry in a Mach 6 flow with collinear light entry," *Applied Optics*, Vol. 61, No. 11, 2022, pp. 3070–3076. 82

[85] Chism, J. R., Gragston, M., Riley, Z., and Hagen, B., "Laser-Induced Schliere Anemometry in a Mach 6 Flow," *AIAA AVIATION 2022 Forum*, 2022, p. 3473. 82

[86] Felver, J., Slipchenko, M. N., Braun, E. L., Meyer, T. R., and Roy, S., "High-energy laser pulses for extended duration megahertz-rate flow diagnostics," *Opt. Lett.*, Vol. 45, No. 16, 2020, pp. 4583–4586. https://doi.org/10.1364/OL.400831. 82

[87] Lester, L., and Gragston, M., "10 kHz Laser-Induced Schliere Anemometry for Velocity, Mach Number, and Static Temperature Measurements in Supersonic Flows," *Applied Optics*, Vol. 60, No. 5, 2021. https://doi.org/0.1364/AO.433085. 83, 87, 89

[88] Willert, C. E., Mitchell, D. M., and Soria, J., "An assessment of high-power light-emitting diodes for high frame rate schlieren imaging," *Experiments in fluids*, Vol. 53, No. 2, 2012, pp. 413–421. 83

[89] Kroll, N., and Watson, K. M., "Theoretical study of ionization of air by intense laser pulses," *Physical Review A*, Vol. 5, No. 4, 1972, p. 1883. 86

[90] Thiyagarajan, M., and Thompson, S., "Optical breakdown threshold investigation of 1064 nm laser induced air plasmas," *Journal of Applied Physics*, Vol. 111, No. 7, 2012, p. 073302. 86

[91] Glumac, N., and Elliott, G., "The effect of ambient pressure on laser-induced plasmas in air," *Optics and Lasers in Engineering*, Vol. 45, No. 1, 2007, pp. 27–35. 86

[92] Gragston, M., Hsu, P., Patnaik, A., Zhang, Z., and Roy, S., "Time-Gated Single-Shot Picosecond Laser-Induced Breakdown Spectroscopy (ps-LIBS) for Equivalence-Ratio Measurements," *Applied spectroscopy*, Vol. 74, No. 3, 2020, pp. 340–346. 86

[93] Anderson, J. D., *Modern compressible flow: with historical perspective*, Vol. 12, McGraw-Hill New York, 1990. 87

[94] Schneider, C. A., Rasband, W. S., and Eliceiri, K. W., "NIH Image to ImageJ: 25 years of image analysis," *Nature methods*, Vol. 9, No. 7, 2012, pp. 671–675. 87

[95] Sagerman, D. G., Rumpfkeil, M. P., Hellman, B. M., and Dasque, N., "Comparisons of Measured and Modeled Aero-thermal Distributions for Complex Hypersonic Configurations," *55th AIAA Aerospace Sciences Meeting*, 2017. https://doi.org/10.2514/6.2017-0264. 88

[96] Riley, Z. B., Perez, R. A., and Ehrhardt, D. A., "Response of a Thin Panel to Aerothermal Loading at Mach 6," *AIAA Journal*, Vol. 59, No. 9, 2021, pp. 3787–3793. https://doi.org/10.2514/1.J060404. 88

[97] DoD, "US Government Website: Mach 6 High Reynolds number Facility," , 2023. URL https://www.afrl.af.mil/Portals/90/Documents/RQ/RQ-Mach-6-High-Reynolds-Number-Facility-180323.pdf?ver=2020-08-28-132037-177. 88

[98] Taylor, J., *Introduction to error analysis, the study of uncertainties in physical measurements*, 1997. 88

[99] Chism, J. R., Gragston, M., Riley, Z. B., Perez, R., Spottswood, M., and Hagen, B., "Cylindrical and Spherical Lens Linear Array-Focused Laser Differential Interferometry on a Flat Plate at Mach 6," *AIAA SCITECH 2022 Forum*, 2022, p. 1659. 96

[100] Chism, J. R., Gragston, M., Peltier, S. J., and McManus, T. A., "Measurements of a Mach 2.3 Turbulent Boundary Layer Using High-Speed Imaging of Linear Array-FLDI," *AIAA AVIATION 2022 Forum*, 2022, p. 3474. 105

[101] Kocher, B. D., Combs, C. S., Kreth, P. A., and Schmisseur, J. D., "Characterizing the streamwise development of surface roughness effects on a supersonic boundary layer," *2018 Fluid Dynamics Conference*, 2018, p. 4047. 106, 110, 121

[102] Shoppell, Z. M., Langley, K. R., and Schmisseur, J. D., "Experimental Investigation of the Role of Shock Strength in Transitional Shockwave-Boundary Layer Interactions," *AIAA SCITECH 2023 Forum*, 2023, p. 1990. 124

[103] Ceruzzi, A., Callis, B., Weber, D., and Cadou, C. P., "Application of focused laser differential interferometry (FLDI) in a supersonic boundary layer," *Aiaa scitech 2020 forum*, 2020, p. 1973. 138

[104] Davenport, K., and Gragston, M., "Simultaneous Turbulent Boundary Layer Velocity Profile and Scalar Turbulence Spectra with Linear Array-FLDI," *AIAA SCITECH 2022 Forum*, 2022, p. 1313. 138

Vita

James Rhett Chism was born in Memphis and raised in Hickory Withe, Tennessee. After graduating from St. Benedict at Auburndale high school in 2013, James attended Mississippi State University where he earned a B.S. in Aerospace Engineering with a minor in German in 2018. After graduation, James joined the HORIZON research group first as a summer intern and then as a Master's student in the subsequent fall semester. Near the end of his Master's program, James switched to the PhD degree track, opting to complete the Master's degree simultaneously with the PhD. James worked in the AFRL Summer Faculty Fellowship program at Arnold Air Force Base, was an invited student researcher at the AFRL Mach 6 wind tunnel at Wright Patterson Air Force Base and at VKF Tunnel C, and was a Lockheed Martin Hypersonics Intern for two semesters.